Title
Time Domain Reflectance for Thermal Conductivity of Electronic Materials

Author
Warkander, Sorren

Publication Date
2022

Peer reviewed|Thesis/dissertation

Time Domain Reflectance for Thermal Conductivity of Electronic Materials

by

Sorren Victoria Warkander

A dissertation submitted in partial satisfaction of the

requirements for the degree of

Doctor of Philosophy

in

Materials Science and Engineering

in the

Graduate Division

of the

University of California, Berkeley

Committee in charge:

Professor Junqiao Wu, Chair
Professor Christopher Dames
Professor Lane Martin

Fall 2022

Abstract

Time Domain Reflectance for Thermal Conductivity of Electronic Materials

by

Sorren Victoria Warkander

Doctor of Philosophy in Materials Science and Engineering

University of California, Berkeley

Professor Junqiao Wu, Chair

Electronic materials represent a vast category with wide-ranging properties. Though definitionally, their electronic properties are of interest, study of their thermal properties provides additional important information. Whether to find materials with desirable thermal conductivity—high to dissipate heat or low to limit heat transport—or because the mechanisms underlying heat transport provide insight into the fundamental physics of the material, thermal characterization allows better understanding of such materials.

In the study of the thermal properties of materials, optical pump-probe methods are a key tool. Laser-based measurements allow probing of small areas without requiring microfabrication, and the use of pulsed lasers and modulated beams allows measurement of high-speed effects and so small sample areas. Time domain thermoreflectivity (TDTR), which uses modulated pulsed laser beams, stands as a key tool for measurement of the thermal properties of both bulk and thin film samples. This work seeks to provide a detailed introduction to the technique and the mathematical analysis required for such measurements, apply TDTR to interesting materials systems, and push beyond the limits of traditional TDTR with the development of a transducerless time domain reflectance (tTDR) technique which uses the same equipment.

Study of thermal properties can provide new insights into the fundamental properties of materials. Metallic vanadium dioxide nanobeams have a much lower thermal conductivity than would be expected given their electrical conductivity, implying that electrons are more effective at carrying charge than heat.[1] This result is not always seen in other sample geometries,[2] and TDTR measurements allow characterization of thin film samples, allowing further study. Unfortunately, the samples measured in this work did not provide high enough electrical conductivity to draw conclusions about electronic thermal transport, but this stands as an interesting line of investigation.

One category of electronic materials of increasing interest is that of two-dimensional materials, whose ultra-thin nature offers new properties and applications. However, it also makes study of their thermal properties challenging and makes traditional TDTR infeasible. By contrast, tTDR is well suited to characterize their properties, and in this work initial measurements were made on suspended molybdenum disulfide. In addition to the fundamental properties of the materials, other effects can be engineered. For example, creating bilayers with twists between layers causes the development of moiré patterns which have novel properties. Their in-plane thermal conductivities are not well characterized, and tTDR provides an avenue for changing that. Preparation of such

samples is very challenging, thus far preventing systematic study as a function of twist angle, but initial measurements demonstrated that tTDR is an applicable tool for such systems.

Time domain reflectance measurements, both in the form of TDTR and tTDR, are powerful tools for the characterization of a wide range of materials, including many electronic materials. This work seeks to offer insight into and expand their applications.

Acknowledgements

It is with gratitude toward many people that I write up this work. Thanks are certainly due to my advisor, Prof. Junqiao Wu, for his support throughout my time in graduate school. His patience and belief in my abilities made it possible for me to navigate these projects. Thanks also to Prof. Chris Dames for clear and interesting instruction about heat transport and for warmth and guidance when I had questions, and to both Prof. Dames and Prof. Lane Martin for serving on my dissertation committee.

At the center of this work is my use of the time domain thermoreflectivity (TDTR) system at the Molecular Foundry at Lawrence Berkeley National Lab (LBNL), and I am very grateful that I have had the opportunity to work with it. Thanks to Dr. Frank Ogletree for ensuring its existence and for being invested in its operation, to Dr. Archana Raja for support in and around the laser lab and for ensuring I established connections with the other researchers in the lab, and especially to Dr. Ed Barnard for teaching me nearly everything I know about the practical side of laser optics, ScopeFoundry, and general equipment maintenance and use. Additionally, thanks to Prof. Sam Huberman and Prof. Gang Chen for providing me my first introduction to TDTR many years ago, and to Prof. Sean Lubner for introducing me to the Foundry system and getting me started both making measurements and analyzing the resulting data. This list would not be complete without mention of Prof. Aaron Schmidt, whose thesis and papers have been invaluable references for me even though we have not crossed paths in person.

Many people have made other contributions that facilitated my work. The VO_2 and WVO_2 samples I studied were grown by Prof. Kechao Tang, who also provided the electrical characterization. My initial development of transducerless time domain reflectance measurements involved measurement of a germanium sample provided by Prof. Joel Ager III and measured with traditional TDTR by Qinshu Li and Prof. Bo Sun. Other parameters for those measurements were provided by Hall effect measurements performed by Dr. Danqing Wang. My study of suspended MoS_2 was made possible by the tireless sample preparation efforts of Zhuowa Wu, supported by Prof. AKM Newaz. Numerous others, especially members of the Wu group, have provided training and assistance throughout my work.

My work has been financially supported through several sources. Work at the Molecular Foundry is supported and funding through the LBNL Electronic Materials Program was available because of the support of the Director, Office of Science, Office of Basic Energy Sciences, Materials Sciences and Engineering Division of the U.S. Department of Energy under Contract No. DE-AC02-05CH11231. I was privileged to receive support from the Department of Defense (DoD) through the National Defense Science & Engineering Graduate (NDSEG) Fellowship Program and from the University of California, Berkeley through the Jane Lewis Fellowship.

It is hard to imagine any of this as being possible without the love provided by those close to me. My parents and brother have modeled curiosity and enthusiasm throughout my life and supported me in all my endeavors. My husband, Jes, has offered me encouragement, perspective, and lots of tea, and has listened to me talk through many things, science-related and not. I am confident that my grandparents would be pleased to see me here, and I treasure how much love I got from them when I was younger. Many other relatives and effectively-relatives have helped me navigate life and reach this point. I want to offer particular gratitude to the network of friends I have built over the last decade or so—their unwavering support, even across thousands of miles, has made my life immensely better. And of course, thanks to my cat, Toast, for love, cuddles, and reminders to value all parts of life.

Contents

1 Introduction

1.1 Motivation

The thermal properties of materials govern their utility in many applications and act as probes for rich understanding of physics. From microelectronics, where nanoscale transistors require effective cooling, to the development of thermoelectric power generation, where low thermal conductivity is desirable, thermal properties have technological relevance. Additionally, they can provide a probe to understand underlying materials physics. For example, careful study of thermal conductivity across the metal-insulator transition in vanadium dioxide has been used as an indicator for Lorentz number suppression, implying non-quasiparticle behavior of electrons in the metallic state.[1]

Beyond bulk materials, the field of two-dimensional materials is growing rapidly. These materials, which function while atomically thin, offer novel possibilities, and significant effort is being applied to their integration in next-generation electronics. This makes understanding of their properties, including thermal properties, increasingly relevant. Additionally, from extremely high thermal conductivity in monolayer graphene[3] to extremely high anisotropy in twisted MoS_2 heterostructures,[4] their thermal properties are themselves of interest. As such, additional understanding of these materials and additional tools to build such understanding are valuable.

1.2 Pump-probe techniques

To characterize the thermal properties of materials, particularly at small length scales, laser-based methods provide valuable tools. The ability to focus laser spots onto small (micron to sub-micron scale) areas to provide heating and measurement allows measurement of samples without requiring microfabrication of electrodes or other similar processing steps. This allows measurements of a wide class of samples, including bulk samples and thin films.

A common category of laser-based measurement is that of pump-probe techniques, in which two laser beams are used. The first, the pump, excites a sample response, and the second, the probe, measures it. Excitation is typically caused by light absorption, and measurement can be done based on reflected or transmitted intensity, among other properties. From the seminal work of Paddock and Eesley,[5] which demonstrated the applicability of transient reflectance for studying thermal transport, much work has been done to develop new and better methods of using pump-probe laser systems to study thermal properties. This dissertation seeks to further expand that body of knowledge.

1.3 Structure of dissertation

This work focuses on building understanding of time domain reflectivity techniques and extending them to new regimes. Chapters 2 and 3 discuss the basic requirements for and theory of time domain reflectivity measurements. Chapter 4 describes methods for working with the multi-parameter nonlinear model that describes such measurements. Chapter 5 describes traditional TDTR measurements of materials near metal-insulator transitions, and Chapters 6 and 7 describe the development and application of the tranducerless time domain reflectivity technique and its applications to bulk and two-dimensional semiconductors.

2 TDTR Fundamentals

2.1 Equipment

The theory of TDTR can be understood by considering relatively few components, though in practice a setup will be significantly more complicated, as shown in Appendix 1 for the system in the Molecular Foundry. Figure 1 shows one version of a minimal TDTR setup. To allow time domain measurements, a pulsed laser and a mechanical delay stage are required; to set and measure at the measurement frequency requires an optical modulator and a lock-in amplifier; and to record signal a photodetector must be included. Additionally, there must be some way to separate the pump and probe beams after they strike the sample, for example a dichroic mirror or short- or long-pass filter for systems which use different wavelengths for the pump and the probe.

The basic principle of the measurement is as follows:

- An ultrafast pulsed laser produces picosecond-scale laser pulses, separated in time by the *laser repetition time*. Most commonly, a titanium sapphire laser is used and produces a train of pulses with a wavelength of 800 nm with a repetition time near 12 nanoseconds.
- Each pulse leaving the laser is split such that some of its intensity is directed to the pump line and some to the probe line. In the setup shown in Figure 2-1, this happens inside the optical parametric oscillator (OPO), which also upconverts the pump light from 800 nm to 565 nm. The OPO allows tuning of the pump wavelength; at the Molecular Foundry 565 nm is chosen to provide maximum signal.
- The pulses on the probe line pass through the mechanical delay stage which increases the distance they travel by a controlled amount.
- Meanwhile, the pulses on the pump line pass through the optical modulator. This modulator changes transmissivity at a controlled frequency (the *modulation frequency*), which is significantly slower than the laser repetition rate. This causes the intensity of the train of pump pulses to vary at the modulation frequency, as shown schematically in Figure 2-2a.
- The dichroic mirror reflects the pump pulses and transmits the probe pulses such that they both strike the sample at normal incidence.
- The pump and probe pulses strike the sample. The *delay time* is defined as the time between the incidence of the pump and probe pulses; for positive delay time the pump strikes first. The relative incidence of pump and probe pulses for positive delay time is shown in Figure 2-2b.
- The pump pulse is absorbed by the sample; the probe pulse is reflected off the sample. (In practical terms, part of the probe pulse is absorbed, but because the train of probe pulses is not modulated, this does

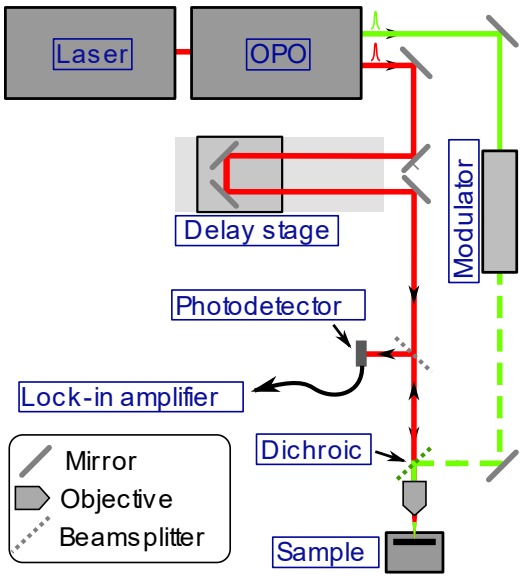

Figure 2-1: Diagram of a minimal two-color TDTR setup. The pump beam is shown at right in green and the probe at left in red.

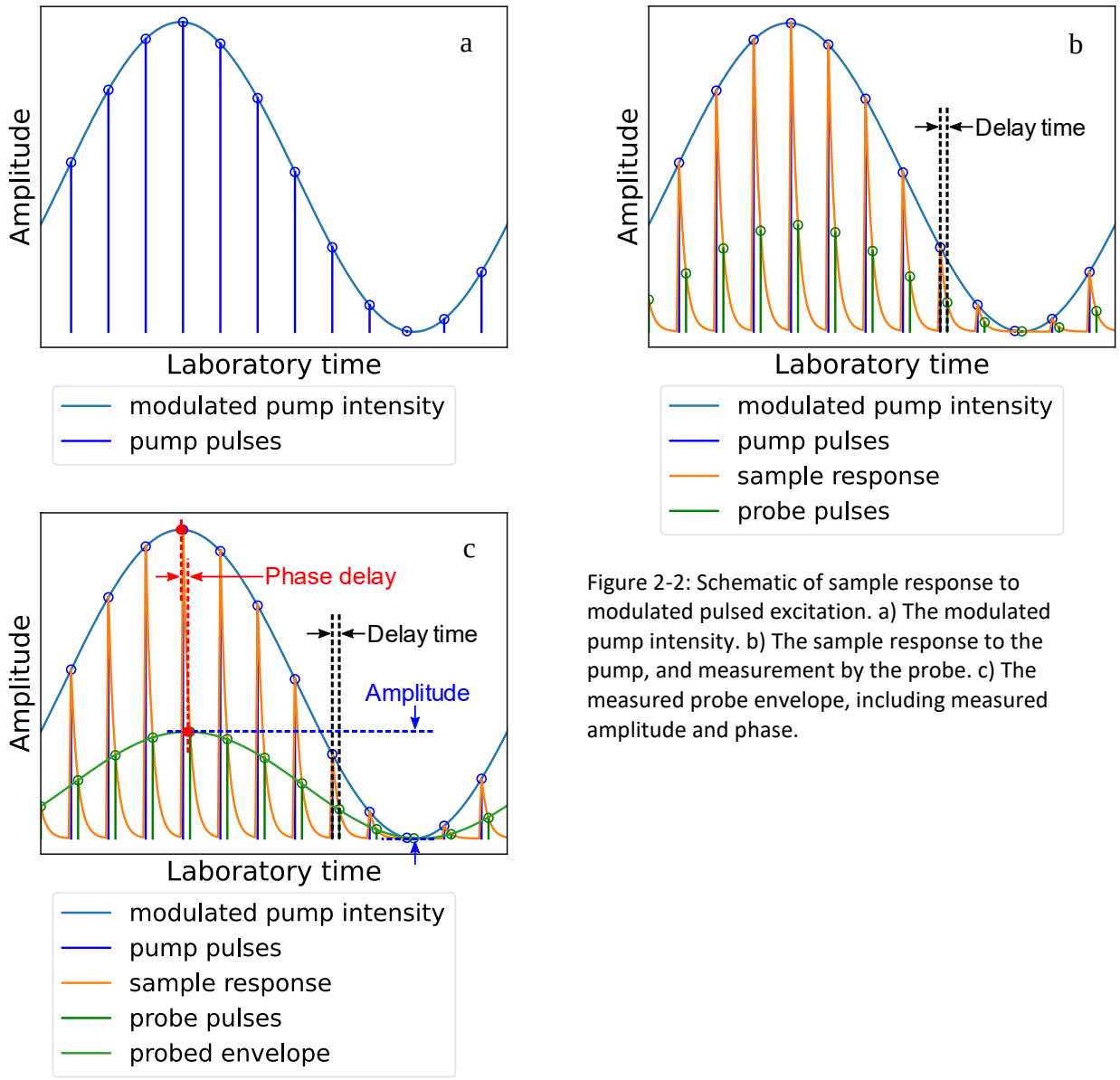

Figure 2-2: Schematic of sample response to modulated pulsed excitation. a) The modulated pump intensity. b) The sample response to the pump, and measurement by the probe. c) The measured probe envelope, including measured amplitude and phase.

not contribute to the TDTR signal. Part of the pump pulse is reflected, but this is optically filtered out and so similarly does not contribute to the final signal.)

- The reflected component of the probe pulse is directed to the photodetector. In systems such as that shown in Figure 1, this is done by a beamsplitter.
- The output from the photodetector is passed to a lock-in amplifier. Because the train of pump pulses is modulated at a set frequency, the reaction of the sample to the pump is modulated at that frequency. (Figure 2-2c) Thus, selecting the same frequency using the lock-in amplifier is equivalent to selecting the component of the sample behavior caused by the pump excitation. The lock-in amplifier measures the amplitude and phase of the probed response. The amplitude is that of the sinusoidal oscillation in probe intensity, as highlighted in Figure 2-2c; the phase is related to the time difference between the maximum intensity of the train of pump pulses striking the sample and the maximum of the probed signal.

Both the delay time and the modulation frequency can be varied in taking a measurement—the first allowing *time domain* thermoreflectivity (TDTR) measurements and the latter their close relative, *frequency domain* thermoreflectivity (FDTR) measurements—as both can have significant effects on the signal. To better understand this, we seek a mathematical description of the TDTR signal and then discuss its behavior in limiting and realistic cases.

2.2 Mathematical Description of TDTR

As described above, TDTR measurements make use of a pulsed laser and optical modulator, which leads to sample excitation from a train of pump pulses separated by some repetition time and varying in intensity with time. Each incident pulse causes some reaction in the sample, which is later measured by the probe pulse. However, for most thermal measurements, the repetition time of the laser is shorter than the time required for the sample to return to equilibrium, leading to accumulation of the effects of each pulse.[6–8] As such, consideration of the laser response to a single pulse is insufficient, and the effects of the modulated train of pulses is required. We thus seek an expression that captures the relationship between the input parameters of delay time and modulation frequency, and the output signal from the lock-in amplifier.

Following the approach of Schmidt, Chen, and Chen,[9] we treat the sinusoidal modulation of the pump intensity as the real part of the complex expression $e^{i\omega_0 t}$, with ω_0 the modulation frequency. Though the laser intensity can only take positive values, so a more accurate expression would be $1 + e^{i\omega_0 t}$, the constant offset is rejected by the lock-in amplifier and can be ignored. We ignore the amplitude of the modulation—the final amplitude of the signal depends on too many factors to be relevant in the circumstances described here and only the normalized amplitude will be considered. The signal measured by the lock-in is a wave of the same frequency as the pump modulation but has different amplitude and phase, which we write as $Ae^{i(\omega_0 t+\phi)}$ for A the amplitude and ϕ the phase. We express the relationship between the pump intensity and the measured signal as a transfer function, the complex number $Z(\omega_0, t_d)$:

$$Ae^{i(\omega_0 t+\phi)} = Z(\omega_0, t_d)e^{i\omega_0 t} \tag{2-1}$$

The amplitude of Z and the phase between its real and imaginary components correspond to the amplitude and phase measured by the lock-in amplifier during an experiment. It should be noted that the raw phase data recorded by the lock-in amplifier depends on the phase delay from many components. For consistency, a phase correction is applied to the signal to force the measured out-of-phase component to be continuous across zero delay time, with the discontinuous behavior caused by the pump showing up entirely in the in-phase signal.[10] It is this phase corrected data which is further analyzed.

2.2.1 Solution using the time domain response

The value of Z can then be approached in two ways: by considering the response of the sample in the time domain, or by considering that in the frequency domain. The first approach is taken by Capinski and Maris,[6] who describe the sample response to be the sum of the responses to all pump pulses. To follow this approach, we write the intensity of the pump as a modulated series of delta functions:

$$I_0(t) \propto \sum_{n=-\infty}^{\infty} e^{i\omega_0 t}\delta\left(t - n\,\tau_{rep}\right) \tag{2-2}$$

where $e^{i\omega_0 t}$ gives the modulated intensity of the pump and the pulsed nature of the laser is accounted for by the sum over delta functions separated in time by the repetition time of the laser, τ_{rep}. If each laser pulse induces a response $h(t)$ in the sample, the total response can be written

$$\sum_{n=-\infty}^{\infty} h\left(t - n\,\tau_{rep}\right) e^{i\omega_0 n \tau_{rep}} \tag{2-3}$$

where the real part of $e^{i\omega_0 n\tau_{rep}}$ gives the relative power of the *n*th pump pulse. The sample response is measured whenever a probe pulse strikes, which occurs a time t_d after each pump pulse, so the probe intensity can be written

$$I_1(t) \propto \sum_{m=-\infty}^{\infty} \delta\left(t - m\,\tau_{rep} - t_d\right) \tag{2-4}$$

The sample response as measured by the probe, i.e. the variation in reflected intensity, is given by the product of equations (2-3) and (2-4):

$$z(t) \propto \sum_{n=-\infty}^{\infty} \sum_{m=-\infty}^{\infty} h\left(t - n\,\tau_{rep}\right) e^{i\,\omega_0\,n\,\tau_{rep}}\,\delta\left(t - m\,\tau_{rep} - t_d\right) \tag{2-5}$$

The expected lock-in output can be found finding the component of this response which varies at the modulation frequency, given by Schmidt[9,10] as

$$Z(\omega_0, t_d) \propto \sum_{q=0}^{\infty} h(q\,\tau_{rep} + t_d)\, e^{-i\omega_0(q\,\tau_{rep}+t_d)} \tag{2-6}$$

where q is restricted to positive values because $h(t) \equiv 0$ for $t < 0$.

This equation can be interpreted as stating that the measured signal is determined by the sum of the response to a single pulse at delay time t_d, the phase-shifted response to the prior pump pulse, now at delay time $t_d + \tau_{rep}$, the phase-shifted response to the pulse which preceded that, and so on. The use of this approach to build understanding of TDTR signals is described in section 2.3.1.

2.2.2 Solution using the frequency domain response

The transfer function *Z* can also be found by considering the response of the sample in the frequency domain, by considering the response of the sample to periodic heating. This approach is taken by Cahill.[7] If the amplitude of the pump signal were purely sinusoidal, i.e. the laser were continuous-wave rather than pulsed, simply considering the intensity as $I_0(t) \propto e^{i\omega_0 t}$ would be sufficient. To find the frequency domain response, we would simply consider the Fourier transform: $\tilde{I}_0(\omega) \propto 2\pi\delta(\omega - \omega_0)$. However, we must account for the pulsed nature of the pump, as in equation (2-2). To do so, we treat each pump pulse as sampling the amplitude of the sinusoid and apply the sampling theorem, which states that a sampled signal

$$x_p(t) = \sum_{n=-\infty}^{\infty} \delta(t - n\tau - T_0)\, x(t) \tag{2-7}$$

can be written in the frequency domain as

$$\widetilde{X_p}(\omega) = \frac{1}{\tau}\sum_{l=-\infty}^{\infty} \tilde{X}\left(\omega - l\frac{2\pi}{\tau}\right) e^{-il\frac{2\pi T_0}{\tau}} \tag{2-8}$$

where $\tilde{X}(\omega)$ is the Fourier transform of $x(t)$ and T_0 is an arbitrary offset between zero time and the time of the first measurement.[11] Applying this approach (with $T_0 = 0$), we find the frequency domain expression of the pump intensity to be

$$\widetilde{I_0}(\omega) \propto \sum_{l=-\infty}^{\infty} \delta\left(\omega - \omega_0 - l\,\frac{2\,\pi}{\tau_{rep}}\right) \tag{2-9}$$

The sample response is given by the convolution of the pump intensity $I_0(t)$ and the impulse response of the sample $h(t)$, which in the frequency domain becomes the product of their Fourier transforms:

$$\sum_{l=-\infty}^{\infty} \delta\left(\omega - \omega_0 - l\,\frac{2\,\pi}{\tau_{rep}}\right)\widetilde{H}(\omega) \tag{2-10}$$

where $\widetilde{H}(\omega)$ is the Fourier transform of $h(t)$ and so represents the single-pulse frequency response of the sample.

The pulsed nature of the probe serves to measure the sample response at times $t_d + n\tau_{rep}$ for integer *n*. To account for this, we again apply the sampling theorem and find that the signal measured by the probe is

$$Z(\omega, t_d) \propto \sum_{l=-\infty}^{\infty}\sum_{m=-\infty}^{\infty}\left[\delta\left((\omega - m\frac{2\,\pi}{\tau_{rep}}) - \omega_0 - l\,\frac{2\,\pi}{\tau_{rep}}\right)\widetilde{H}\left(\omega - m\,\frac{2\,\pi}{\tau_{rep}}\right)\right] e^{-im\frac{2\pi}{\tau_{rep}}t_d} \tag{2-11}$$

The lock-in amplifier selects only the component of the signal at $\omega = \omega_0$; upon evaluating $Z(\omega_0)$, the delta function eliminates terms where $l \neq -m$, so we replace l with $-m$ and eliminate one of the sums, finding

$$Z(\omega = \omega_0, t_d) \propto \sum_{m=-\infty}^{\infty} \delta(\omega - \omega_0)\,\widetilde{H}\left(\omega + m\,\frac{2\,\pi}{\tau_{rep}}\right) e^{im\frac{2\pi}{\tau_{rep}}t_d} \tag{2-12}$$

which simplifies to

$$Z(\omega_0, t_d) \propto \sum_{m=-\infty}^{\infty} \widetilde{H}\left(\omega_0 + m\,\frac{2\,\pi}{\tau_{rep}}\right) e^{im\frac{2\pi}{\tau_{rep}}t_d} \tag{2-13}$$

This is the frequency domain equivalent of equation (2-6), and can be shown to be mathematically equivalent.[10] It can be interpreted as saying that the measured TDTR signal is the sum of the frequency response at the modulation frequency (with a phase shift due to the delay

time) and the frequency response at all multiples of $\frac{2\pi}{\tau_{rep}}$, a frequency set by the laser repetition rate. This allows another avenue for understanding TDTR signals, as discussed in section 2.3.2.

2.3 Fast and slow effects in a model system

Though the actual response of a sample to a pump pulse is more complicated than an exponential decay and will be considered in Chapter 3, considering the signal that would arise from a purely exponential single pulse response provides valuable insight.

2.3.1 Responses in the time domain

As discussed in section 2.2, the measured signal consists of the amplitude and phase of the modulated probe reflectivity, which are represented by those of a transfer function, Z . Here we discuss equation (2-6) to build understanding of TDTR signals. From equation (2-6), we see that the measured TDTR signal is given by a sum of the responses of the sample to each incident pump pulse, adjusted by a phase. Crucially, to understand the TDTR signal, we must consider not only the response to the pump pulse which most closely preceded the probe pulse (the $q = 0$ term), but also any residual effect from previous pulses. Let us consider the limiting cases of fast and slow sample responses.

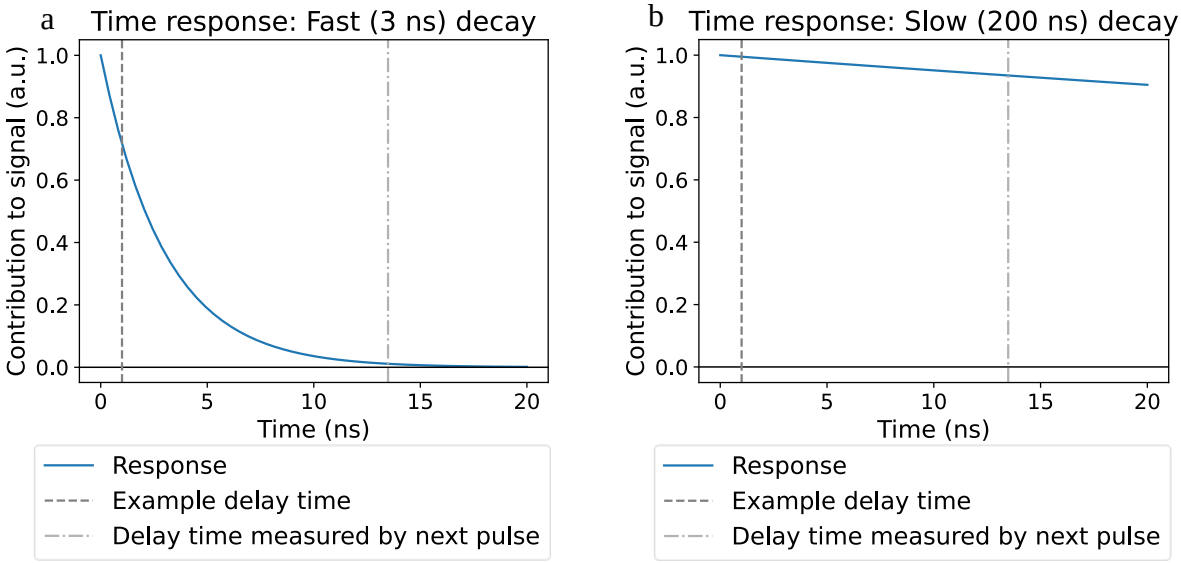

Figure 2-3:Schematic “fast” and “slow” sample responses to a single pump pulse, shown in the time domain. a) The fast response dies out between pulses of the laser and b) the slow response does not.

2.3.1.1 Case 1: Purely fast sample response

We first consider the case of a sample response that decays exponentially with a characteristic time significantly shorter than the time between pulses from the laser, as shown in Figure 2-3a for the case of a 3 ns exponential characteristic time and a 12.5 ns laser repetition rate. In this case, the sample returns to steady state before the next pulse arrives, sometimes described as an absence of accumulation effects between laser pulses. Each laser pulse independently influences the sample, and the measured TDTR signal is equivalent to the single-pulse response of the sample. Because the single-pulse response has no dependence on

modulation frequency, this means that the measured signal will be the same across modulation frequencies and depend only on delay time.

2.3.1.2 Case 2: Purely slow sample response

If the characteristic timescale of the sample response is much longer than the time between laser pulses, as shown in Figure 3b for a 200 ns characteristic time and a 12.5 ns laser repetition rate, the response to a single pump pulse is nearly the same when measured by the probe pulse follows it most closely in laboratory time and when measured by the next probe pulses. Equivalently, each probe pulse measures the effect of not just the pump pulse that most closely preceded it, but also several pump pulses before that—the response from multiple pump pulses accumulates. The small change in the signal over the measurable range of delay times, which is usually a few nanoseconds but cannot be longer than the laser repetition rate, means that the measured TDTR signal depends only weakly on delay time. As discussed further below, there will be a significant dependence on modulation frequency.

2.3.2 Responses in the frequency domain

Thus far, the sample response has been viewed in the time domain, with the temporal response to a single pulse as the starting point. We now turn to considering the relationship between the frequency domain single-pulse response and the measured signal. Applying equation (2-13) we can express the measured signal in terms of the sample frequency response, which is simply the Fourier transform of the time response. As for the time response, we see that the measured signal is determined by the response at the modulation frequency ω_0, but also by that at multiples of a frequency set by the laser repetition rate, $\frac{2\,\pi}{\tau_{rep}}$. We consider how this applies to fast and slow single-pulse responses.

2.3.2.1 Case 1: Purely fast sample response

A fast response in the time domain corresponds to a broad frequency response, as shown in Figure 2-4a. Comparison to the frequencies measured by the laser makes it clear that multiple frequencies contribute, up to large values of frequency. This corresponds to fast (high frequency) responses being important, which is unsurprising given the defined fast nature of the sample response. More instructive is looking at the low frequency behavior, within the range of possible modulation frequencies. As shown in Figure 2-4c, the frequency response is nearly flat through this range, meaning that, as discussed above, changing the modulation frequency has minimal effect on the signal.

2.3.2.2 Case 2: Purely slow sample response

A slow response in the time domain corresponds to a sharp frequency response. (Figure 2-4b) Because the frequency response drops off more rapidly as frequency increases than in the case of a fast sample response, only relatively low frequencies contribute to the signal. This implies that, as expected, very little happens over short time scales. Additionally, the larger magnitude of the response at the modulation frequency compared to that at other measured frequencies means that the response at the modulation frequency more strongly determines the measured signal. Looking at the response within the range of accessible modulation frequencies (Figure 2-4d), the clear contrast from the fast signal response case is obvious. Unlike in the fast response case, in the case of a slow response changing the modulation frequency has a significant impact on the

measured signal. This highlights that varying the modulation frequency is a powerful way to measure slow sample responses.

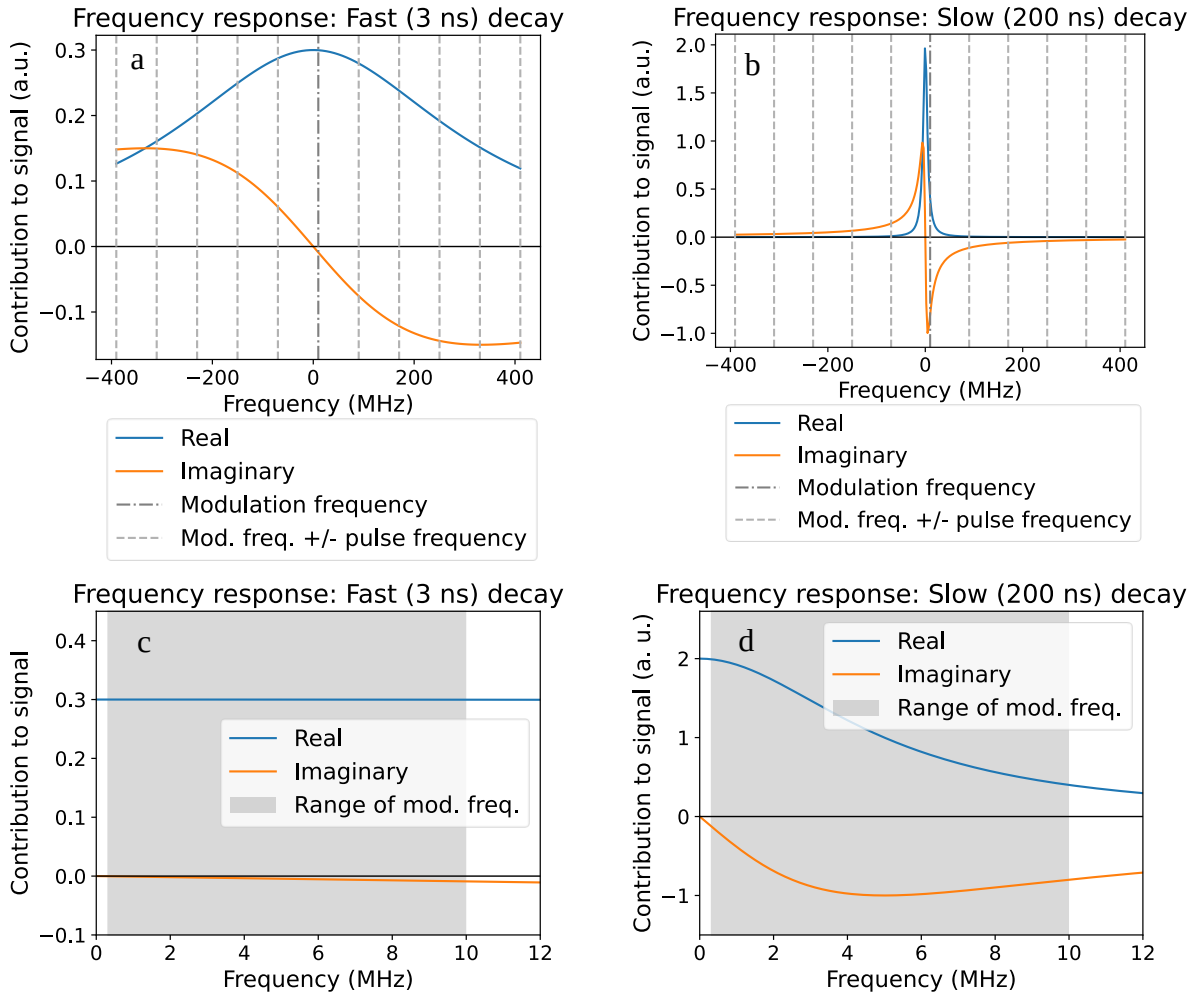

Figure 2-4: Schematic "fast" and "slow" sample responses to a single pump pulse, shown in the frequency domain. a) The fast response has significant magnitude over a wide range of frequencies; b) the slow response does dies off quickly with frequency. c) Zooming in on the low-frequency behavior of a), it is clear that the response has little variation within the range of experimentally accessible modulation frequencies. d) Zooming in on the low-frequency behavior of b) highlights the dependence of measured sample response on modulation frequency.

2.3.3 Simulated TDTR signal for fast and slow responses

For easier comparison to experimental data, the TDTR signal that would be generated from a sample with a purely exponential response is calculated. The discussion above most clearly applies to the magnitude of the TDTR signal. In the case of the magnitude of the signal, the strong dependence on delay time for the sample with a fast response (Figure 2-5a) and minimal dependence on delay time for that with a slow response (Figure 2-5c) is easily visible. Similarly, the magnitude of the TDTR signal for the sample with a fast response does not show a dependence on modulation frequency, whereas that for the sample with a slow response changes dramatically. The phase signal is less easy to directly interpret as its slope varies with modulation frequency for both fast and slow responses, but it should be noted that for small delay times the

phase signal for the sample with a fast response (Figure 2-5b) is nearly independent of modulation frequency, like the magnitude signal, whereas the phase signal for the sample with a slow response (Figure 2-5d) depends on modulation frequency at all delay times. Additionally, the phase for the sample with a fast response is nearer to 90 degrees, corresponding to a small component out-of-phase with the modulation, whereas the sample with a slow response has a much smaller phase, indicating a larger out-of-phase component. Out-of-phase components most easily arise due to accumulation effects, so it is expected that the sample with a slow response would show a larger out-of-phase component.

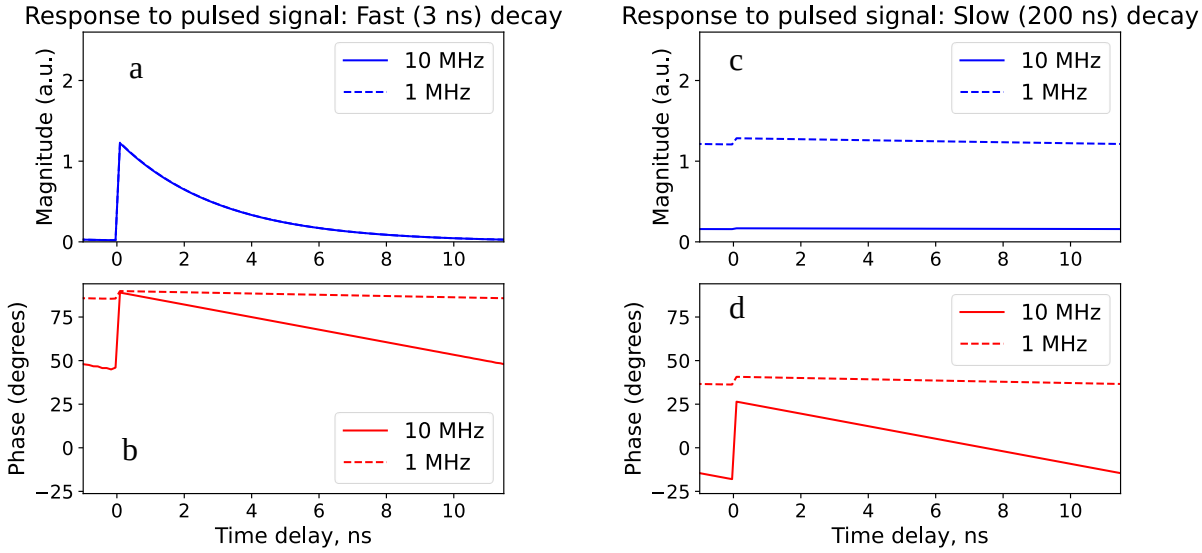

Figure 2-5: Simulated TDTR signal for samples with a,b) the fast response shown in Figures 2-3 and 2-4 and c,d) the slow response shown in Figures 2-3 and 2-4. The dependence on delay time is much stronger in the case of the fast signal, and the dependence on modulation frequency is stronger in the case of the slow signal.

2.4 Model signal from realistic samples

We now seek to apply our understanding of TDTR signals and their origins to modeling of realistic samples. To see the effects of both faster and slower heat transport, we consider two materials: silicon, with a thermal conductivity of 148 W/mK,[12] and fused quartz, with a thermal conductivity of 1.3 W/mK.[13] For standard TDTR measurements, such samples would be coated with a layer of metal, so we model them as coated with 70 nm of aluminum. The calculation of the thermal response of such samples is discussed in Chapter 3, but here we consider the results qualitatively.

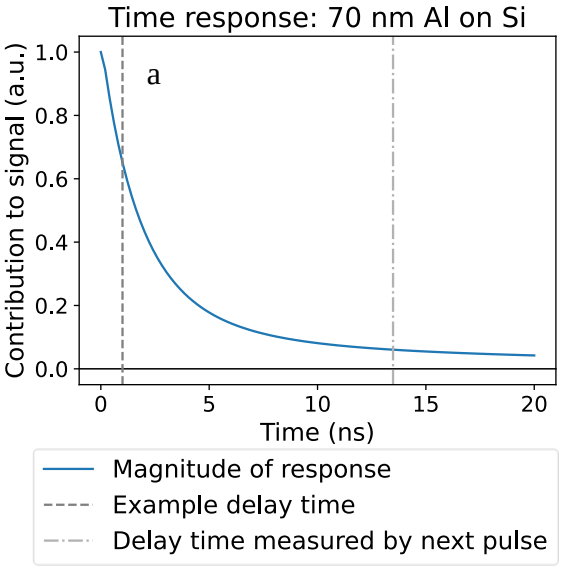
Time response: 70 nm Al on Si
a
Contribution to signal (a.u.)
Time (ns)
Magnitude of response
Example delay time
Delay time measured by next pulse

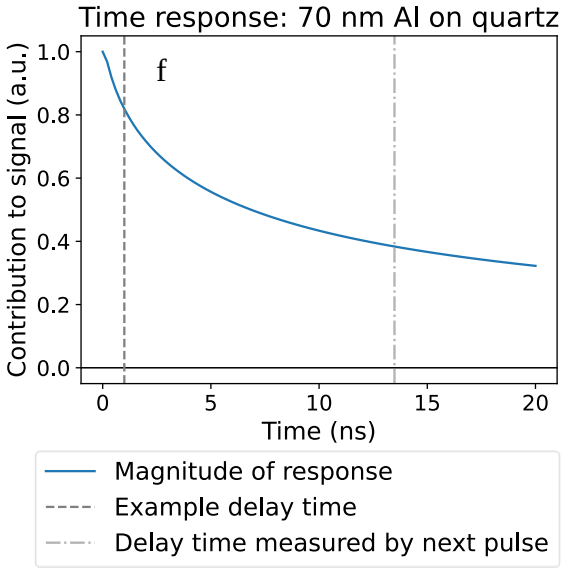
Time response: 70 nm Al on quartz
f
Contribution to signal (a.u.)
Time (ns)
Magnitude of response
Example delay time
Delay time measured by next pulse

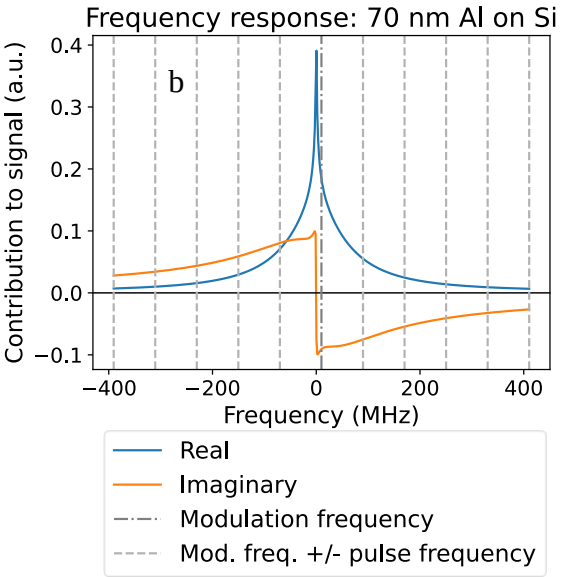
Frequency response: 70 nm Al on Si
b
Contribution to signal (a.u.)
Frequency (MHz)
Real
Imaginary
Modulation frequency
Mod. freq. +/- pulse frequency

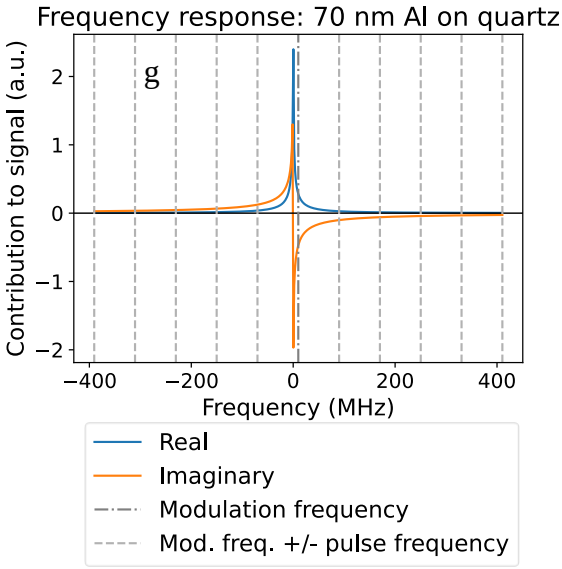
Frequency response: 70 nm Al on quartz
g
Contribution to signal (a.u.)
Frequency (MHz)
Real
Imaginary
Modulation frequency
Mod. freq. +/- pulse frequency

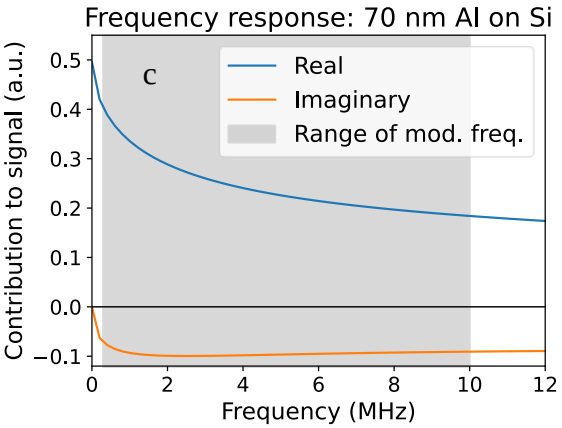
Frequency response: 70 nm Al on Si
c
Real
Imaginary
Range of mod. freq.
Contribution to signal (a.u.)
Frequency (MHz)

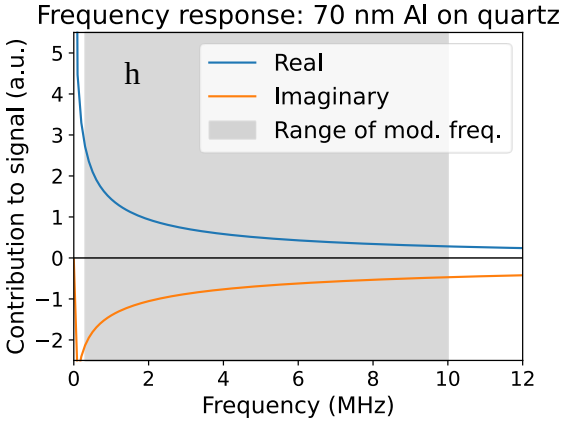
Frequency response: 70 nm Al on quartz
h
Real
Imaginary
Range of mod. freq.
Contribution to signal (a.u.)
Frequency (MHz)

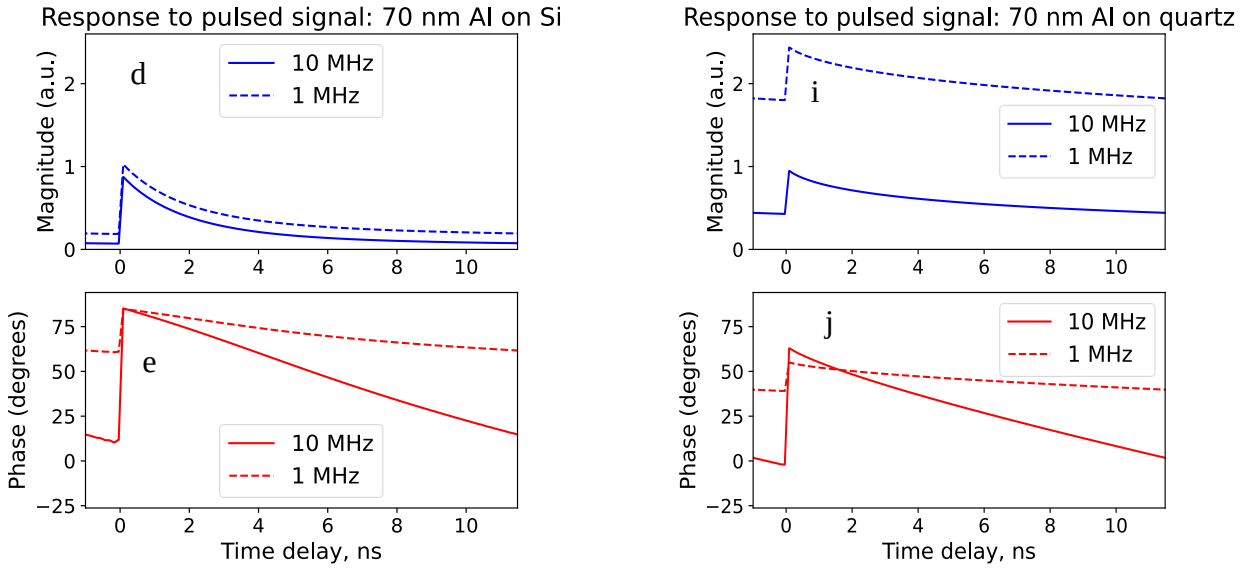

Figure 2-6: Single-pulse and simulated TDTR data for samples of (a-e) 70 nm Al on Si and (f-j) 70 nm Al on quartz. Both show some features of a fast response, but the quartz sample shows some slow response signature as well. See main text for full discussion.

We begin by considering the single pulse responses, as we did for the fast and slow response models. For the time domain responses of both aluminum on silicon (Figure 2-6a) and aluminum on quartz (Figure 2-6f), there is a moderately fast decay over the first few nanoseconds. However, especially in the case of quartz, the decay becomes slower as time increases; ignoring the first few nanoseconds, the sample response could be described as slow. Physically, this corresponds roughly to initial heat flow in the top (thermally conductive) silicon layer, followed by a transition to slower transport across the interface to the substrate and within the quartz. The overall frequency domain responses (Figures 2-6b and 2-6g) also show responses on a number of timescales. Both show a sharp spike at low frequency, indicating a component of a slow response; overall, though, the silicon response is broader than that of the quartz, corresponding to the faster response we expect of a more thermally conductive sample. When we focus specifically on the range of modulation frequencies accessible in a measurement, we still see a behavior with components of both fast and slow responses: for the aluminum on silicon (Figure 6c), the real part of the frequency response remains significant across the range of modulation frequencies, as for the fast sample response shown in Figure 2-4b, though it does decrease with frequency and the imaginary part is non-trivial, as for the slow sample response shown in Figure 4d. The aluminum on quartz sample (Figure 2-6h) shows primarily slow behavior—both real and imaginary components are significant, and the real component decays significantly over the range of accessible modulation frequencies. From this assessment, the aluminum on silicon sample can be expected to react mostly like a sample with a purely fast response but show some slow response behavior as well, especially with variations in modulation frequency. The aluminum on quartz sample can be expected to have more slow response behavior, particularly in modulation frequency dependence, but to also show some fast response behavior, especially at small delay times.

Looking at the simulated TDTR signal in Figures 2-6d-e and 2-6i-j, we see approximately this behavior. In Figure 6d, the magnitude of the TDTR signal for the aluminum on silicon

sample, we see behavior that looks very similar to the modeled fast sample response (Figure 2-5a), with the exception that there is some dependence of the overall signal on modulation frequency. This indicates that there is also a slower component to the sample response, as expected. The phase behavior (Figure 2-6e) is somewhat similar to that for the sample with a fast response (Figure 2-5b) in that the phase at low delay times is similar across modulation frequencies, but the range of phase covered by the signal for the aluminum on silicon sample is much larger, likely due to the non-exponential nature of the response. The magnitude of the calculated TDTR signal for aluminum on quartz (Figure 2-6i) shows both a fast, delay time dependent response, and a distinct dependence on modulation frequency. This indicates, as expected, that both fast and slow responses are present. The phase data (Figure 2-6j) is at 1 MHz similar to that for a slow sample response (Figure 2-5d), but at 10 MHz differs, and is more similar to the response for aluminum on silicon (Figure 2-6e). Higher modulation frequency corresponds to measurement less deep in the sample, so it makes sense that the two aluminum-coated samples would look more similar, and that the slower heat transport in the quartz would be less significant at 10 MHz than at 1 MHz.

2.5 Overview

In this section, we have focused on understanding of the origin of TDTR signal. The basics of the experimental apparatus are discussed, and the significance of the measured signal in terms of the underlying sample response is considered. We now turn to further understanding of that sample response.

3 Heat flow and measurement

3.1 Physics of laser incidence

3.1.1 Metals

In traditional TDTR implementations, samples are coated with a layer of metal, most typically aluminum, which then interacts with both the pump and probe lasers. Here we consider the effects of these laser incidences and how they contribute to the TDTR measurement.

3.1.1.1 Pump laser

The purpose of the incidence of the pump beam of the TDTR setup is to provide a heat source at the sample surface, the diffusion from which can be monitored. However, the energy of the incident laser beam is not instantaneously converted to heat, but rather undergoes a complicated absorption process. Particularly due to the ultrafast pulsed nature of the pump beam, it is important to consider the response of the metal to the incident light.

The initial response of a metal to incident light is driven by electron-photon interactions. In response to a laser pulse, electrons are excited to a highly non-equilibrium state in which those electrons which absorb photons have significantly more energy than those that do not, making the definition of an electron temperature unclear. The absorbed energy causes both diffusive and ballistic transport of the hot electrons through the metal which occurs simultaneously with scattering between hot and cold electrons.[14,15] As electrons scatter with each other, they reach a better-defined energy distribution, allowing the definition of an electron temperature (separate from the lattice temperature due to slower electron-phonon scattering) by a time hundreds of femtoseconds to a few picoseconds after the absorption of the laser pulse. Because of the low heat capacity of electrons, this temperature can be very high, e.g. a few thousand Kelvin.[15] Starting simultaneously with the establishment of the electron temperature, but in general occurring more slowly, scattering occurs between electrons and the lattice, causing their temperatures to equilibrate.[16,17]. The rate of this equilibration is determined by the electron-phonon coupling coefficient, which for aluminum is approximately 20×10^{16} W/m^{3}K,[18] and in typical metals takes hundreds of femtoseconds to a few tens of picoseconds.[19] Because of the higher heat capacity of the lattice, lattice temperature excursions are much smaller, usually less than 10 K in typical TDTR measurements.

Within tens of picoseconds, the initial response to the laser pulse has died out and only heat transport needs to be considered. Because typical TDTR modeling considers only diffusive heat transport and neglects differences in electron and lattice temperatures, only delay times greater than 100 ps are typically considered for data analysis. For these delay times, the temperature at the sample surface is well approximated as resulting from heat transport through the materials and interfaces of the sample, as described below.

Most researchers treat the laser energy as fully absorbed at the surface of the sample. Lubner[20] follows an approach where the top 10 nm of the aluminum layer, as well as the thermal properties of the native oxide layer on top of the aluminum, are condensed to a 1 nm layer with 10 times the heat capacity in order to account for the finite laser penetration depth. Lubner's approach was taken in this work.

3.1.1.2 Probe laser

The reflection of the probe laser is used to monitor changes in the sample surface temperature, which is possible due to a property known as *thermoreflectivity*. The reflectivity of materials has a relatively weak dependence on temperature, typically on the order of dR/dT ~10^{-4}-10^{-5} K^{-1} for common metals such as Al, Au, Cu, and Ni,[21,22] but this is easily detectable in a TDTR experiment. Several mechanisms underlie the thermoreflectance of metals. A non-exhaustive list of such mechanisms includes:[21]

- Decrease in density due to thermal expansion decrease the plasma frequency and can warp or shift electron energy bands. Such shifts in band structure can lead to Fermi level shifts. This can lead to changes in reflectivity.
- The Fermi distribution function becomes less sharp as temperature increases, changing the population of electrons available for transitions that originate or terminate at energies near the Fermi level. For wavelengths of light corresponding to the energies of these transitions, reflectivity will change.
- The phonon population increases with temperature, which leads to increased electron-phonon interactions, decreases electron relaxation times and can lead to changes in electron band structure. Again, this leads to changes in reflectivity.

These effects are in general non-linear with temperature, but for small temperature deviations such as those in a typical TDTR measurement a Taylor expansion approach can be taken and the reflectivity can be treated as varying linearly with temperature.

Aluminum is commonly used in TDTR experiments in large part because of its relatively high thermoreflectivity, especially near the 800 nm wavelengths typical of titanium:sapphire lasers. A combination of two interband transitions is excited by near-800 nm light,[23] and changes in temperature lead to shifts in the electronic structure that underlies them and so in the reflectivity of the probe light.[21] This leads to a thermoreflectivity coefficient on the order of 10^{-4} K^{-1}.[22] Thus, for probing at 800 nm, aluminum-coated samples provide significantly higher signal than those coated with other metals.

We assume that the probe laser penetration depth is shallow enough to model the probe laser as measuring the surface temperature of the sample.

3.1.2 Semiconductors

This work is not limited to samples which are coated in metal, but also considers the case in which the pump and probe laser beams are directly incident on a semiconductor surface. The physics underlying the absorption of the pump beam and reflection of the probe are somewhat different because of the finite bandgap of the material. These are discussed in Chapter 6.

3.2 Physics of heat flow

In solids, conduction is the dominant heat transfer mechanism phenomenon: heat flows in response to temperature gradients. This is described by Fourier's Law, $q = -\bar{\bar{\kappa}}\nabla T$,[24] with the proportionality between flux and temperature gradient given by $\bar{\bar{\kappa}}$, the thermal conductivity of the material, which is a second order tensor which is a function of temperature.[25] This is an effective phenomenological description but provides little insight into the ties between heat transport and other processes.

To identify such links, it is necessary to move to a microscale view of the solid. We view the solid as a network of atoms held together by chemical bonds. At finite temperature, the atoms vibrate about their equilibrium positions, and because of the bonds between them, vibrations are

transmitted from one atom to its neighbors. Looking at the solid as a whole, such transmitted vibrations can be viewed as collective oscillations and called phonons. A reasonable approximation of lattice behavior can be made by treating the phonons as particles moving through the space occupied by the material.[26] They can scatter because of collisions with other phonons, defects in the material, or boundaries; the average distance traveled between scattering events is denoted as the mean free path, λ. The phonon contribution to the thermal conductivity is given by $k_{phonon} = \frac{1}{3} C v \lambda$, where C is the heat capacity of the material and v is the average phonon velocity.[26] Velocity scales with the strength of the atomic bonding, so materials with stronger bonds are generally more thermally conductive; lattice defects and material interfaces tend to scatter phonons, reducing λ and so conductivity. Phononic thermal conductivity varies with temperature. At low temperature, the mean free path is determined mostly by impurity and boundary scattering and does not change with T, so the thermal conductivity scales like the heat capacity of the material, proportional to T^3. As temperature increases, phonon-phonon scattering becomes more significant, and the mean free path starts to fall. The heat capacity plateaus as temperature increases, so the thermal conductivity will also fall.[26]

In insulators, conductive heat transport is determined primarily by the behavior of phonons, but in materials with mobile electrons, the transport of electrons from one part of the system to another carries significant energy. Each electron carries kinetic energy given by its mass and velocity, $KE = \frac{1}{2} m v^2$. The more electrons move, the more energy is transported and the higher the thermal conductivity. The ease of electron motion can be quantified by the electron mobility, μ. The electrical conductivity, σ, is determined by the product of the mobility, the number of mobile electrons, and the amount of charge carried by the electron: $\sigma = qn\mu$. If we assume that each electron is moving approximately as a free particle, its mean speed will scale as $T^{1/2}$,[26]so the kinetic energy will scale with T. Because the charge of the electron is temperature independent, we expect that the ratio of the electronic thermal conductivity (proportional to kinetic energy) and the electrical conductivity (proportion to charge) will be proportional to temperature. This is known as the Wiedemann-Franz Law, $\frac{\kappa_{electron}}{\sigma} = LT$. The constant L is known as the Lorentz number. Its exact value depends on the system under study, but for metals and degenerately doped semiconductors, it is usually $2.44*10^{-8}$ W Ω K^{-2} .[27] In non-degenerately doped semiconductors, the value of L is somewhat lower (called Lorentz number suppression), but the proportionality holds.

Heat transport by phonons and that by electrons coexist, however in insulators and most semiconductors thermal conductivity is dominated by phonon behavior and in most metals it is dominated by electronic transport.

3.3 Mathematical description of heat flow in TTR

To determine the thermal properties of samples, as is the goal of TTR, requires understanding how those properties impact the measured signal. This requires understanding how thermal properties impact heat flow through a sample, and how that heat flow determines the measured response. We begin by discussing the simplest case: a bulk metal.

3.3.1 Heat transport in bulk and layered materials with metal surfaces

3.3.1.1 Bulk metal

For the purposes of this analysis, we consider only diffusive thermal transport. This assumption is valid when the mean free paths of heat carriers are significantly smaller than the other length scales in the experiment, such as the laser spot size and depth of heat penetration into the sample. In samples with long mean free paths and for experimental conditions that give small length scales, ballistic heat transport must also be considered,[28] but that is beyond the scope of this work.

To model diffusive thermal transport, we turn to the well-established Fourier model:[24]

$$-\nabla \cdot (\Lambda \nabla T) + c_p \frac{\partial T}{\partial t} = 0 \tag{3-1}$$

where Λ is the thermal conductivity, which is in general a tensor, and c_p is the volumetric heat capacity. We simplify this by considering a material with radial symmetry, where the thermal conductivity tensor will be the same in both radial directions. Equation (3-1) can then be expanded to

$$-\Lambda_z \frac{\partial^2 T}{\partial z^2} - \Lambda_r \frac{1}{r}\frac{\partial}{\partial r}\left(r \frac{\partial T}{\partial r}\right) + c_p \frac{\partial T}{\partial t} = 0 \tag{3-2}$$

where Λ_z is the thermal conductivity in the *z* direction (into the material) and Λ_r is the thermal conductivity in the radial direction. To solve this equation, we first take the Fourier transform, replacing the time derivative with multiplication by $i\omega$:

$$-\Lambda_z \frac{\partial^2 \tilde{T}}{\partial z^2} - \Lambda_r \frac{1}{r}\frac{\partial}{\partial r}\left(r \frac{\partial \tilde{T}}{\partial r}\right) + c_p i\omega \tilde{T} = 0 \tag{3-3}$$

Then, assuming a medium with infinite radial extent, we take the Hankel transform, which replaces the derivative in r with multiplication by $-k^2$:

$$-\Lambda_z \frac{\partial^2 \tilde{T}}{\partial z^2} + \Lambda_r k^2 \tilde{T} + c_p i\omega \tilde{T} = 0 \tag{3-4}$$

which is now a differential equation in terms of only z,

$$\frac{\partial^2 \tilde{T}}{\partial z^2} = \frac{\Lambda_r k^2 + c_p i\omega}{\Lambda_z} \tilde{T} \tag{3-5}$$

and is solved by

$$\tilde{T}(z, k, \omega) = Ae^{-qz} + Be^{qz} \tag{3-6}$$

and equivalent expressions, where

$$q^2 = \frac{\Lambda_r k^2 + c_p i\omega}{\Lambda_z} \tag{3-7}$$

In the case of an effectively semi-infinite sample (one where the sample thickness is much greater than other length scales), we apply the boundary condition that the temperature deviation must go to zero as z becomes large:

$$\lim_{z \to \infty} \tilde{T} = 0 \tag{3-8}$$

so

$$\tilde{T}(z, k, \omega) = Ae^{-qz} \tag{3-9}$$

For the purposes of analyzing TDTR data, we need to know how the temperature responds to heating. For samples with metal surfaces, we consider only surface heating and surface measurement. For a heat source of magnitude *Q* at the surface, we can write

$$Q = -\Lambda_z \left.\frac{d\tilde{T}}{dz}\right|_{z=0} \tag{3-10}$$

or

$$Q = \Lambda_z q A \tag{3-11}$$

The quantity we seek is the thermal response, $G = \tilde{T}/Q$, which here is

$$G_{bulk}(\omega, k) = \frac{1}{q\Lambda_z}\, e^{-qz} \tag{3-12}$$

or, at the surface ($z = 0$) as measured in traditional TDTR,

$$G_{bulk}(\omega, k) = \frac{1}{q\Lambda_z} \tag{3-13}$$

For the purposes of TDTR measurements, the surface heating is provided by the pump beam, which is assumed to have a Gaussian radial distribution:

$$p_0(r) = A_0 e^{(-2r^2/w_0^2)} \tag{3-14}$$

where w_0 is the $1/e^2$ radius of the pump laser spot.

To apply this to our solution for G, we apply a Hankel transform and find

$$\tilde{p}_0(k) = \frac{A_0}{4\pi} e^{-k^2 w_0^2/8} \tag{3-15}$$

In real space, the temperature deviation caused by the pump heating is given by the convolution of the pump profile and the sample thermal response, but in the spacial frequency domain this becomes multiplication:

$$\tilde{T}_{surf}(k, \omega) = \frac{A_0}{4\pi} e^{-k^2 w_0^2/8}\, G_{bulk}(\omega, k) \tag{3-16}$$

The measured TDTR signal is based on the reflection of the probe beam, which occurs over the area of the probe laser spot. We consider a probe spot with a Gaussian profile of radius w_1:

$$p_1(r) = A_1 e^{(-2r^2/w_1^2)} \tag{3-17}$$

The measured component of the temperature deviation is then given by the real space equation

$$H(\omega) = \int_0^\infty A_1 T_{surf}(r) e^{(-2r^2/w_1^2)}\, r\, dr \tag{3-18}$$

We use the fact that $T_{surf}(r)$ can be found by taking the inverse Hankel transform of $\tilde{T}_{surf}(k)$,

$$\begin{aligned} T_{surf}(r) &= \int_0^\infty \tilde{T}_{surf}(k) J_0(k r)\, k\, dk \\ &= \int_0^\infty \frac{A_0}{4\pi} e^{-k^2 w_0^2/8}\, G_{bulk}(\omega, k)\, J_0(k r)\, k\, dk \end{aligned} \tag{3-19}$$

where J_0 is the 0th order Bessel function of the first kind, and write

$$H(\omega) = \int_0^\infty A_1 \int_0^\infty \frac{A_0}{4\pi} e^{-k^2 w_0^2/8}\, G_{bulk}(\omega, k)\, J_0(k r)\, k\, dk\, e^{(-2r^2/w_1^2)}\, r\, dr \tag{3-20}$$

Switching the order of integration and simplifying, we find

$$\begin{aligned} H(\omega) &= \frac{A_0 A_1}{4\pi} \int_0^\infty G_{bulk}(\omega, k) e^{-k^2 w_0^2/8} \int_0^\infty e^{(-2r^2/w_1^2)}\, J_0(k r)\, r\, dr\, k\, dk \\ &= \frac{A_0 A_1}{16\pi^2} \int_0^\infty G_{bulk}(\omega, k) e^{-k^2 (w_0^2 + w_1^2)/8}\, k\, dk \end{aligned} \tag{3-21}$$

which is generally evaluated numerically.

Equation (3-21) is the frequency domain sample response discussed in section 2.2.2.

3.3.1.2 Layered structures

For layered samples, like many of those involved in TDTR measurement, heat flow through multiple materials and interfaces must be modeled. For example, for a metal-coated sample, heat diffuses first through the metal, then through the interface between the metal and the layer below, and then through the layer below, and so on for as many layers as present in the sample.

The conductivity of interfaces is a rich topic[29–31] but for our purposes we consider only the result that heat flow through an interface can be described as proportional to the temperature difference across the interface and so summarized by an interface conductivity, analogous to the thermal conductivity of bulk materials.

Finding the thermal response of a layered sample involves solving the heat equation in all layers and matching appropriate boundary conditions at the interfaces. This process can be made tractable through a frequency-domain matrix formalism. Two main approaches have been taken in the literature.

Cahill[7] builds on the algorithm developed by Feldman,[32] which treats temperature flow each layer, e.g. layer *j*, as two traveling thermal waves, one moving in $+z$ and the other in $-z$:

$$T_j(z) = T_j^+ e^{qz} + T_j^- e^{-qz} \tag{3-22}$$

Feldman and Cahill describe one-dimensional systems where $q^2 = i\,\omega\frac{c_p}{\Lambda_z}$ for ω the frequency, c_p the volumetric heat capacity, and Λ_z the thermal conductivity in the direction of heat flow. As derived above in section 3.3.1.1 and by Schmidt,[33] this can readily be extended to include radial conduction by redefining q as in equation (3-7).

Alternatively, Schmidt, Chen, and Chen[9] follow the approach developed by Carslaw and Jaegar,[34] in which the temperature and heat flux at each location are modeled. The two approaches involve different arithmetic but yield equivalent results. Here we follow Cahill's approach.

Equation (3-22) can be made easier to manipulate by representing the temperature in each layer with the vector

$$\vec{T_j}(z) = \begin{pmatrix} T_j^+ e^{q_j z} \\ T_j^- e^{-q_j z} \end{pmatrix} \tag{3-23}$$

Several important relationships can then be expressed in matrix form:

i) Heat flow within a layer, e.g. from point z_1 to point z_2, can be expressed by matrix multiplication:

At z_1,

$$T_j(z_1) = T_j^+ \mathrm{e}^{q_j z_1} + T_j^- \mathrm{e}^{-q_j z_1} \tag{3-24}$$

so

$$\vec{T_j}(z_1) = \begin{pmatrix} T_j^+ e^{q_j z_1} \\ T_j^- e^{-q_j z_1} \end{pmatrix} \tag{3-25}$$

At z_2,

$$T_j(z_2) = T_j^+ e^{q_j z_2} + T_j^- e^{-q_j z_2}$$
$$= T_j^+ e^{q_j z_1} e^{q_j (z_2 - z_1)} + T_j^- e^{-q_j z_1} e^{-q_j (z_2 - z_1)} \quad (3\text{-}26)$$

meaning that

$$\overrightarrow{T_j}(z_2) = \begin{pmatrix} T_j^+ e^{q_j z_1} e^{q_j (z_2 - z_1)} \\ T_j^- e^{-q_j z_1} e^{-q_j (z_2 - z_1)} \end{pmatrix}$$
$$= \begin{pmatrix} e^{q_j (z_2 - z_1)} & 0 \\ 0 & e^{-q_j (z_2 - z_1)} \end{pmatrix} \overrightarrow{T_j}(z_1) \quad (3\text{-}27)$$
$$\equiv \boldsymbol{U_j}(z_2 - z_1) \overrightarrow{T_j}(z_1)$$

where we define

$$\boldsymbol{U_j}(z_2 - z_1) \equiv \begin{pmatrix} e^{q_j (z_2 - z_1)} & 0 \\ 0 & e^{-q_j (z_2 - z_1)} \end{pmatrix} \quad (3\text{-}28)$$

as the operator for translation within a layer.

ii) Heat flow across boundaries can be written as matrix multiplication. If we consider a boundary with negligible thermal resistance at location $z = \xi$ between two layers a and b, as shown in Figure (3-1), we can write temperature and heat flux continuity as

$$T_a(\xi^-) = T_b(\xi^+) \quad (3\text{-}29)$$
$$\Lambda_{z,a} \left. \frac{dT_a}{dz} \right|_{z=\xi^-} = \Lambda_{z,b} \left. \frac{dT_b}{dz} \right|_{z=\xi^+} \quad (3\text{-}30)$$

which are satisfied if

$$\overrightarrow{T_b}(\xi^+) = \frac{1}{2\, q_b \Lambda_b} \begin{pmatrix} q_b \Lambda_\mathrm{b} + q_a \Lambda_\mathrm{a} & q_b \Lambda_\mathrm{b} - q_a \Lambda_\mathrm{a} \\ q_b \Lambda_\mathrm{b} - q_a \Lambda_\mathrm{a} & q_b \Lambda_\mathrm{b} + q_a \Lambda_\mathrm{a} \end{pmatrix} \overrightarrow{T_a}(\xi^-)$$
$$\equiv \boldsymbol{\Gamma_{ba}} \overrightarrow{T_a}(\xi^-) \quad (3\text{-}31)$$

where

$$\boldsymbol{\Gamma_{ba}} \equiv \frac{1}{2\, q_b \Lambda_b} \begin{pmatrix} q_b \Lambda_\mathrm{b} + q_a \Lambda_\mathrm{a} & q_b \Lambda_\mathrm{b} - q_a \Lambda_\mathrm{a} \\ q_b \Lambda_\mathrm{b} - q_a \Lambda_\mathrm{a} & q_b \Lambda_\mathrm{b} + q_a \Lambda_\mathrm{a} \end{pmatrix} \quad (3\text{-}32)$$

is defined as the matrix operator for moving from layer *a* to layer *b*,[32] and we have dropped the subscript *z* for simplicity of notation.

Thermal resistance can also be accounted for by adding terms to this matrix expression,[32] but in TDTR modeling it is more practical to treat the interface as its own extremely thin (e.g. 1 nm) layer with negligible heat capacity.

iii) Consideration of the boundary conditions surrounding an infinitesimal region of heat generation located within a material, e.g. at location $z = \zeta$, allows relating the temperature vectors on the two sides of the heat source:

$$\overrightarrow{T_a}(\zeta^+) - \overrightarrow{T_a}(\zeta^-) = -\frac{Q}{2\,q_a\Lambda_a}\begin{pmatrix}1\\-1\end{pmatrix} \tag{3-33}$$

where Q represents the heating power.[32]

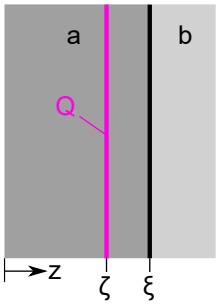

Figure 3-1: A 1D sketch of a simple layered structure with localized heating to which Feldman's algorithm can be applied.

These tools are used to find the surface temperature of a TDTR sample in response to heating. In Figures (3-1) and (3-2) we illustrate this with a 1D sketch, but note that consideration of appropriately defined q allows the same approach to be used for 3D radially symmetric samples. A model layered structure is shown in Figure (3-2). The left-most layer is taken to have an insulated surface (for most TDTR measurements, heat loss to the air is negligible), and the right-most layer is taken to be semi-infinite. This assumption is valid when the layer thickness is much greater than the penetration depth of the TDTR measurement, which is typically on the order of microns to hundreds of microns. We assess how the surface temperature is changed by near-surface heating.

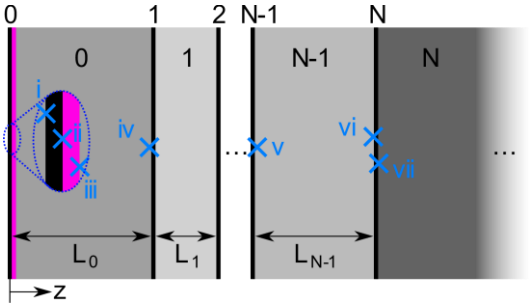

Figure 3-2: A more complicated layered structure with near-surface heating, as in a TDTR measurement

Treating the surface as position $z = 0$, the heat source is considered to be localized at an infinitesimal depth at $z = \epsilon$, where ϵ is an extremely small value. We now consider the modeling of the temperature at each of the marked points, following the procedure laid out by Feldman.[32]

For points i and ii, we begin with the boundary condition at the left side of the structure. Point i is located to the left of the interface between layer 0 and the air, at $z = 0^-$. Applying equation (3-22) to the air layer, we find

$$T_{air}(z) = T_{air}^{+}e^{qz} + T_{air}^{-}e^{-qz} \tag{3-34}$$

and note that any non-zero value for T_{air}^{-} will lead to a temperature which diverges away from the structure, which is unphysical. Therefore, we define

$$\overrightarrow{T_{air}}(z) = \begin{pmatrix}T_{surf}\,e^{qz}\\0\end{pmatrix} \tag{3-35}$$

where we have used the fact that at $z = 0^-$, $T_{air} \equiv T_{surf}$. We then evaluate at $z = 0^-$ to find the value of $\vec{T}$ at point i:

$$\overrightarrow{T_i} = \begin{pmatrix} A \\ 0 \end{pmatrix} \equiv \begin{pmatrix} T_{surf} \\ 0 \end{pmatrix} \tag{3-36}$$

We next seek $\vec{T}$ at point ii, which we find by applying matrix operator $\boldsymbol{\Gamma_{air,0}}$:

$$\overrightarrow{T_{ii}} = \boldsymbol{\Gamma_{air,0}} \overrightarrow{T_i} \tag{3-37}$$

Treating the thermal conductivity of air as zero (perfectly insulating), we simplify:

$$\boldsymbol{\Gamma_{air,0}} = \frac{1}{2\, q_0\Lambda_0} \begin{pmatrix} q_0\Lambda_0 & q_0\Lambda_0 \\ q_0\Lambda_0 & q_0\Lambda_0 \end{pmatrix} = \frac{1}{2} \begin{pmatrix} 1 & 1 \\ 1 & 1 \end{pmatrix} \tag{3-38}$$

$$\overrightarrow{T_{ii}} = \frac{1}{2} \begin{pmatrix} 1 & 1 \\ 1 & 1 \end{pmatrix} \begin{pmatrix} T_{surf} \\ 0 \end{pmatrix} = \frac{1}{2} \begin{pmatrix} T_{surf} \\ T_{surf} \end{pmatrix} \tag{3-39}$$

We now consider the temperature vectors at points iii-vii. For these, we work from the rightmost point (vii) leftward. Point vii is located on the right side of the interface between materials N-1 and N. We begin by writing an expression for the temperature in layer N in terms of the components of the temperature vector, using equation (3-22):

$$T_N(z) = T_N^+ e^{qz} + T_N^- e^{-qz} \tag{3-40}$$

In parallel to the above argument, we note that any non-zero component of T_N^+ will lead to a divergence as $z \to \infty$. Thus, as above,[32]

$$\overrightarrow{T_{vii}} = \begin{pmatrix} 0 \\ T_{bulk} \end{pmatrix} \tag{3-41}$$

Following the same process we used to find the temperature vector at point ii, we apply $\boldsymbol{\Gamma_{N-1,N}}$ to find that at vi, which lies across the interface from vii:

$$\overrightarrow{T_{vi}} = \boldsymbol{\Gamma_{N-1,N}} \begin{pmatrix} 0 \\ T_{bulk} \end{pmatrix} \tag{3-42}$$

where all terms of $\boldsymbol{\Gamma_{N-1,N}}$ are given by the properties of materials N and N-1 and the parameters of the measurement.

We now seek the temperature vector at point v, which lies in material N-1 a distance L_{N-1} to the left of vi, at the interface with material N-2. This is found by applying the operator $\boldsymbol{U_{N-1}}(L_{N-1})$:

$$\overrightarrow{T_v} = \boldsymbol{U_{N-1}}(L_{N-1}) \times \boldsymbol{\Gamma_{N-1,N}} \begin{pmatrix} 0 \\ T_{bulk} \end{pmatrix} \tag{3-43}$$

where again $\boldsymbol{U_{N-1}}$ is fully determined by the properties of material N-1 and the measurement parameters.

A similar process is applied to cross each boundary and move through each layer. For example, point iv lies at the right edge of material 0, and the temperature vector there can be expressed as

$$\overrightarrow{T_{iv}} = \boldsymbol{\Gamma_{0,1}} \times \boldsymbol{U_1}(L_1) \times \boldsymbol{\Gamma_{1,2}} \times \ldots \times \boldsymbol{U_{N-1}}(L_{N-1}) \times \boldsymbol{\Gamma_{N-1,N}} \begin{pmatrix} 0 \\ T_{bulk} \end{pmatrix} \tag{3-44}$$

and point iii lies at $z = \epsilon^+$, infinitesimally close to the left edge of material 0, so the temperature vector there can be written

$$\overrightarrow{T_{iii}} = \boldsymbol{U_0}(L_0) \times \boldsymbol{\Gamma_{0,1}} \times \boldsymbol{U_1}(L_1) \times \boldsymbol{\Gamma_{1,2}} \times \ldots \times \boldsymbol{U_{N-1}}(L_{N-1}) \times \boldsymbol{\Gamma_{N-1,N}} \begin{pmatrix} 0 \\ T_{bulk} \end{pmatrix} \tag{3-45}$$

For convenience, we define

$$\overrightarrow{T_{iii}} \equiv T_{bulk} \begin{pmatrix} B^+ \\ B^- \end{pmatrix} \tag{3-46}$$

We now have expressions for the temperature at $z = 0^+ = \epsilon^-$ and $z = \epsilon^+$ (points ii and iii), which are separated only by the infinitesimal layer of heat deposition. We use equation (3-33) to relate these:

$$\overrightarrow{T_0}(\epsilon^+) - \overrightarrow{T_0}(\epsilon^-) = \overrightarrow{T_{ui}} - \overrightarrow{T_{ui}} = -\frac{Q}{2\,q_0\Lambda_0}\begin{pmatrix}1\\-1\end{pmatrix} \tag{3-47}$$

$$T_{bulk}\begin{pmatrix}B^+\\B^-\end{pmatrix} - \frac{1}{2}\begin{pmatrix}T_{surf}\\T_{surf}\end{pmatrix} = -\frac{Q}{2\,q_0\Lambda_0}\begin{pmatrix}1\\-1\end{pmatrix} \tag{3-48}$$

Separating this into two equations,

$$T_{bulk}B^+ - \frac{1}{2}T_{surf} = -\frac{Q}{2\,q_0\Lambda_0} \tag{3-49}$$

$$T_{bulk}B^- - \frac{1}{2}T_{surf} = \frac{Q}{2\,q_0\Lambda_0} \tag{3-50}$$

we can solve for T_{surf}:

$$T_{surf} = \frac{Q}{q_0\Lambda_0}\left(\frac{B^+ + B^-}{B^- - B^+}\right) \tag{3-51}$$

So, the surface temperature response per unit heating will be

$$G_{layered}(\omega, k) = \frac{1}{q_0\Lambda_{z,0}}\left(\frac{B^+ + B^-}{B^- - B^+}\right) \tag{3-52}$$

with

$$\begin{pmatrix}B^+\\B^-\end{pmatrix} = \boldsymbol{U_0}(L_0) \times \boldsymbol{\Gamma_{0,1}} \times \boldsymbol{U_1}(L_1) \times \boldsymbol{\Gamma_{1,2}} \times \ldots \times \boldsymbol{U_{N-1}}(L_{N-1}) \times \boldsymbol{\Gamma_{N-1,N}}\begin{pmatrix}0\\1\end{pmatrix} \tag{3-53}$$

This result is used by Cahill for a system where all materials are isotropic.[7]

As with the modeling of heat flow in bulk materials, we seek the response, as measured by the probe beam, to the heating caused by the pump. Conveniently, the approach is the same as for a bulk material, so we can use equation (3-21) and simply replace $G_{bulk}(\omega, k)$ with $G_{layered}(\omega, k)$:

$$H(\omega) = \frac{A_0 A_1}{16\pi^2}\int_0^\infty G_{layered}(\omega, k)e^{-k^2(w_0^2+w_1^2)/8}\,k\,dk \tag{3-54}$$

where A_0 and A_1 are the pump and probe intensities and w_0 and w_1 are the pump and probe spot radii. This equation is generally solved numerically, and, plugged into equation (2-13) gives a model of the measured signal.

3.3.2 Heat transport coupled with charge transport

Modeling for samples where the laser is directly incident on a semiconductor surface is more complicated. This case is described in Chapter 6.

3.4 Summary

We have discussed the interactions between lasers and our samples and established a method for accounting for their frequency responses. Combining this with the results from Chapter 2 we have a recipe to move from materials properties and system parameters to measured signal. Fitting this model to experimental data allows the determination of materials parameters.

4 Determination of sample properties

As discussed in Chapters 2 and 3, the measured signal in a time domain reflectivity (TDR) measurement relates to the properties of the materials that make up the sample, but the relationship is complicated. In order to extract materials properties from measured data, a model describing the sample is constructed using the equations in Chapter 3, and a non-linear fitting algorithm is used to fit to unknown properties, such as the thermal conductivity of the material under test.

4.1 Existing approach: Python curve_fit

Numerous algorithms for non-linear fitting are available and could be used with TDR data. One of the most user-friendly is provided by the Python package SciPy,[35] as the function scipy.optimize.curve_fit. By default, this function uses the Levenberg-Marquardt algorithm to minimize the sum of the squares of the residuals between the model and the data.[36–38] Bounds on the parameters can be provided, though in most cases in this work they were not and failure to find physically reasonable values was seen as a reason to question data validity. Multiple parameters can be solved for simultaneously, though solving for too many results in numerical instability. The definition of "too many" is discussed below. The function returns several values, most relevantly the best fit parameters and an estimated covariance matrix. Though the covariance matrix provides one measure of the uncertainty in the fit, curve_fit does not account for uncertainty in input parameters other than those being solved for, so the returned matrix alone often grossly underestimates the uncertainty. For example, for measurements with small laser spot sizes, the uncertainty in measuring the spot size leads to uncertainty in the fitted value. Naïve use of curve_fit does not account for this. To account for such errors, parameters subject to uncertainty were manually perturbed and fits were found at each parameter value. Combining the resulting variance of the output parameters gives an improved estimate of the overall measurement uncertainties:

$$\Delta\Lambda_{tot} = \sqrt{\sum_i (\Delta\Lambda_i)^2} \tag{4-1}$$

where $\Delta\Lambda_{tot}$ represents the total error reported, and $\Delta\Lambda_i$ is the error resulting from the perturbation of each parameter. This, however, does not accurately account for interactions among parameter values—that is, whether the uncertainty in two or more parameters affects the fit similarly or differently. As such, it is a useful estimate but could be improved upon.

Though curve_fit is a powerful tool for determining parameters which allow the modeled TDR data to match the measured data, questions remain about how to use it well. Here, two main questions are addressed: how many parameters can be fit, and how uncertainty in other parameters affects the results.

4.2 Number of fitting parameters

It is not uncommon for several sample properties in a TDR measurement to be unknown or poorly known. For example, typical measurements seek to determine the thermal conductivity of a sample material, but the thermal conductance of the interface between the sample material and other layers is unlikely to be known. Though it is straightforward to write code to that leaves multiple parameters unknown, whether a measurement provides enough information to independently determine those properties must be considered in order to get meaningful results.

The standard approach to assessing what can be solved for relies on a tool known as a sensitivity plot, which summarizes how the modeled data varies with variation in given parameters. Generally, qualitative assessment of the sensitivities to different parameters is used to select measurement conditions and determine what is appropriate to fit. In this work, the use of Fisher information matrices to provide a more quantitative result is proposed.

4.2.1 Sensitivity plots

Intuitively, whether two parameters can be independently solved for is determined by whether they affect the result in sufficiently different ways. For example, if one parameter affects the model only at short delay times and another only at long delay times, both can be determined. In practice, the effects are rarely so simple. A sensitivity plot provides a way of viewing how strongly a parameter affects the model in various regimes. As shown in Figure 4-1 a-c), the simplest way to determine the effect of changing a parameter is simply to perturb it and compare the perturbed and unperturbed models. However, this rapidly becomes unwieldy. To better summarize such information, the sensitivity to a parameter is defined as

$$S = \frac{d\ln(model\ result)}{d\ln(parameter)} \tag{4-2}$$

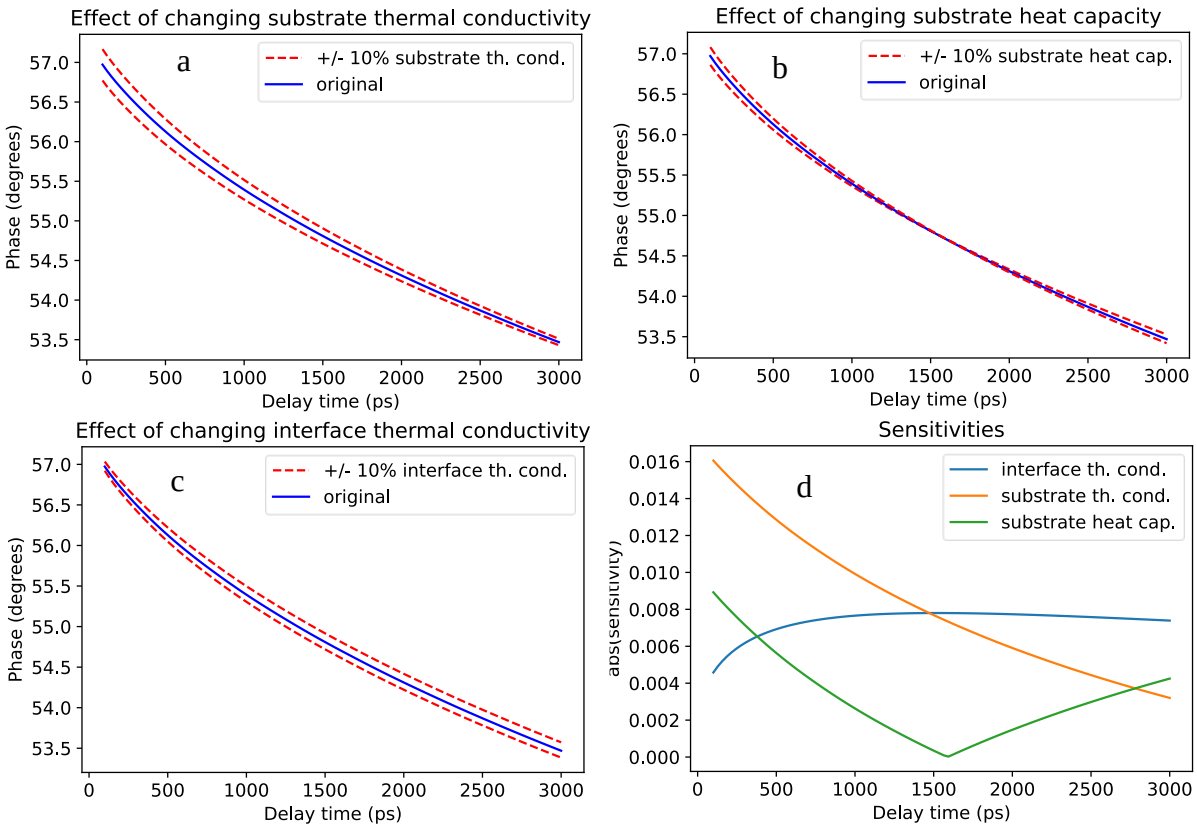

Figure 4-1: For a quartz sample coated with 70 nm of aluminum and measured with a 0.3 MHz modulation frequency, the effects on the calculated caused by perturbations in a) substrate thermal conductivity, b) substrate heat capacity, and c) interface thermal conductivity can be compactly summarized as lines in d) a sensitivity plot.

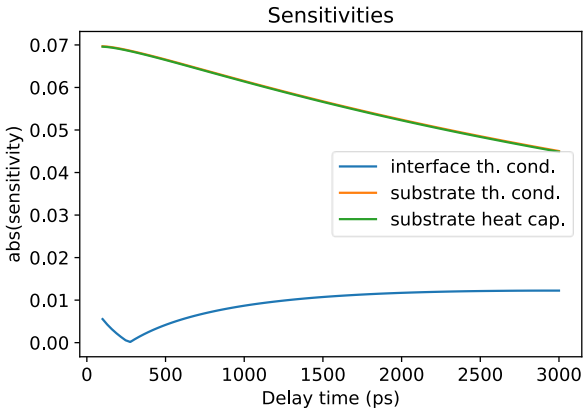

Figure 4-2: For a quartz sample coated with 70 nm of aluminum and measured with a 10 MHz modulation frequency, the sensitivity to substrate heat capacity is nearly identical to that to substrate thermal conductivity, unlike for measurements at 0.3 MHz (as in Figure 4-1).

where, for example, the model result is the magnitude or phase of the measured signal. The use of the natural logarithm inside the derivative provides normalization, since $d\ln(x) = \frac{1}{x}dx$, which allows improved comparisons between parameters that are valid regardless of units. By calculating the sensitivity for various parameters, it is straightforward to view several effects at once, as shown in Figure 4-1d. This provides a powerful tool for comparing the effects of various parameters—for example, it quickly becomes clear that in relatively thermally insulating samples, such as quartz, measurements at high modulation frequencies are nearly identically sensitive to heat capacity and thermal conductivity, (Figure 4-2) but at lower modulation frequencies the effects are different. (Figure 4-1d) Thus, if both are unknown or uncertain, measurement at lower frequency is more helpful. But, as mentioned above, this relies on a qualitative assessment of similarity.

4.2.2 Fisher information matrices

The framework of Fisher information provides a tool to better quantify what can be determined from a measurement. The Fisher information provides a value that expresses how much information an observable variable (say the amplitude or phase at a given delay time and modulation frequency) gives about an unknown parameter (say, the thermal conductivity).[39] Defining the likelihood function for the observable, X, for a given value of the unknown parameter, θ, as $f(X,\theta)$, the Fisher information is given by[39]

$$I(\theta) = E\left[\left(\frac{\partial}{\partial\theta}\ln f(X,\theta)\right)^2 \mid \theta\right] = \int \left(\frac{\partial}{\partial\theta}\ln f(x,\theta)\right)^2 f(x,\theta)\,dx \qquad (4\text{-}3)$$

where $E[g(X|\,\theta)]$ represents the expectation value of $g(X)$ at a given value of θ, and the integration over all possible values x of the observable X means that the resulting information, $I(\theta)$, is not a function of the measured value X. However, the units chosen for θ do matter: if θ is multiplied by a constant, the Fisher information will scale as well: $I(a\theta) = a^2\,I(\theta)$.[39] To avoid complications from unit selection, calculations of information in this work were done based on parameters normalized to their initial estimates.

The above definition is valid for a measurement that depends on a single parameter, but the result easily generalizes to multi-parameter measurements. For a measurement which depends on n parameters, the scalar $I(\theta)$ is replaced with a $n \times n$ matrix with terms given by[39]

$$I_{i,j}(\vec{\theta}) = E\left[\left(\frac{\partial}{\partial\theta_i}\ln f(X,\vec{\theta})\right)\left(\frac{\partial}{\partial\theta_j}\ln f(X,\vec{\theta})\right) \mid \vec{\theta}\,\right] \qquad (4\text{-}4)$$

where $\vec{\theta}$ is a vector of the n parameters. This matrix is referred to as the Fisher information matrix (FIM).

An important application of the Fisher information (in scalar or matrix form) is its use in defining the Cramér-Rao bound,[40,41] which states that the variance of an unbiased estimator cannot be lower the inverse of the Fisher information. In the scalar case, this refers to single numbers; in the matrix case, the inverse of the FIM provides bounds on the variance-covariance matrix for the parameters. Though the topic of selecting unbiased estimators is beyond the scope of this work, the bound provides the insight that a large Fisher information is desirable for accurate parameter estimation. Higher Fisher information corresponds to lower uncertainty in estimated parameters.

Calculation of the FIM is often used in optimal experiment design, where measurement conditions are selected to maximize properties such as the determinant, trace, or value of the smallest eigenvalue of the FIM, in order to minimize the variance of one or, usually, several parameters.[42] In this work, the measurement conditions are taken as given (or rather, chosen for experimental convenience) and the FIM is used to assess the information content of the resultant data, but the same tools apply. Calculation of the likelihood function needed to find the Fisher information matrix requires knowledge of how θ affects X—that is, a model of the system. Though Chapter 3 lays out such a model, its nonlinear nature means that the likelihood and so the Fisher information is a function of the model parameters. This makes use of the Fisher information a somewhat circular process, wherein estimates of the parameters must be used to calculate it before it can be used to determine what parameters can be fit to. Similarly, if the model does not accurately represent the sample, the estimate of the FIM it provides will be inaccurate.

One important implication of the Cramér-Rao bound is that uncertainties can be determined only if the matrix is invertible—that is, not singular. In fact, if the matrix is singular, not all parameters can be observed simultaneously.[43] Definitionally, the matrix is singular if any of the eigenvalues are zero. Practically, when calculating from experimental models, eigenvalues may be finite but very small, making the matrix near-singular and causing inversion to be unstable. For the purposes of this work, a matrix with smallest eigenvalue more than three orders of magnitude smaller than the largest eigenvalue is treated as effectively singular. The number of non-zero eigenvalues of a matrix is its rank, and for a matrix of dimension *n x n* to be non-singular, it must have rank *n*. The dimension of the FIM is determined by the number of parameters involved in the calculation, so for a given FIM the rank, or equivalently the number of non-zero eigenvalues, gives the maximum number of parameters that can be determined. An FIM with rank less than its dimension may imply that it is possible to solve for combinations of the parameters, e.g. the thermal effusivity, just not for each parameter uniquely, e.g. the thermal conductivity and heat capacity.

In the simplest case, the FIM would have no off-diagonal elements, and so neither would its inverse, the optimally measured variance-covariance matrix. With actual physical models, this tidiness is unlikely, and off-diagonal elements of the FIM are likely to be non-zero. It is worthwhile, then, to consider their physical significance. For the FIM of just two parameters, the limiting cases of a toy model are presented:

1) $$FIM = \begin{pmatrix} 1 & \varepsilon \\ \varepsilon & 1 \end{pmatrix}, \varepsilon \ll 1 \rightarrow FIM^{-1} = \begin{pmatrix} 1 & -\varepsilon \\ -\varepsilon & 1 \end{pmatrix} \quad (4\text{-}5)$$

For small values of the off-diagonal elements of the FIM, the Cramér-Rao bound gives a minimum covariance equivalent to minus the value of the off-diagonal element—the

magnitudes of the off-diagonal elements correspond to the magnitude of the covariance, and when they are zero the parameters are not correlated.

2) $$FIM = \begin{pmatrix} 1 & 1-\varepsilon \\ 1-\varepsilon & 1 \end{pmatrix}, \varepsilon \ll 1 \rightarrow FIM^{-1} = \frac{1}{2\,\varepsilon}\begin{pmatrix} 1 & -1 \\ -1 & 1 \end{pmatrix} \quad (4\text{-}6)$$

For large values of the off-diagonal elements, the matrix becomes nearly singular, so its inverse diverges as $1/\varepsilon$. Additionally, though, the magnitude of the off-diagonal elements of the Cramér-Rao bound also approach one—the parameter estimates become very strongly correlated when the off-diagonal elements approach the diagonal elements. This result generalizes to higher dimensions—larger values of off-diagonal elements correspond to more strongly correlated parameter estimates.

It should be noted that for multiple independent measurements, FIMs add.[39] Intuitively, multiple measurements, especially at different conditions, should provide more information, and mathematically this is true. Thus, a near-singular FIM does not mean that parameters cannot be determined at all, simply that the measurement for which the FIM was calculated is insufficient.

4.2.2.1 4.2.2.1 Examples of the FIM: Aluminum on quartz

To make the arguments of the previous section clearer, some FIMs for a model system consisting of 80 nm of aluminum on a quartz substrate are calculated. The eigenvalues, normalized to their largest value for clarity, are presented in Table 4-1, and the FIMs, again normalized to the largest diagonal element, are presented in Figure 4-3. From the list of eigenvalues, it is immediately apparent that that at the lower modulation frequency it is potentially possible to determine at least two of the three parameters considered here, as two of the eigenvalues are within an order of magnitude of each other. At the higher modulation frequency, the second-largest eigenvalue is already orders of magnitude smaller than the first, so it is only possible to determine one of the three values. Looking at the FIMs more directly allows insight into several key differences between the two modulation frequencies. First, at high frequencies the off-diagonal elements between the thermal conductivity and heat capacity for the quartz approach one, implying that those parameters are extremely correlated and trying to solve for both will lead to a near-singular FIM. Second, the on-diagonal element for the interface thermal conductivity is much smaller at high frequency, implying that uncertainty in that parameter will be larger for a low-frequency measurement than for a higher-frequency one (compared to the uncertainty in thermal conductivity of quartz, since these FIMs are normalized). However, the off-diagonal elements between the thermal conductivity of quartz and the interface conductivity are smaller at higher frequency, implying lower correlation between these parameter estimates. This information could be used to inform measurement choices—for example, if the goal is measurement of thermal conductivity and a significant source of uncertainty arises from uncertainty in the heat capacity of quartz, measurement at lower frequency is more suitable. If uncertainty in the result is predominantly from uncertainty in interface conductivity, measurement at higher frequency might be a better choice, though there might not be enough information in the measurement to determine both the interface

Eigenvalues, normalized to largest value:

0.3 MHz modulation	10 MHz modulation	Combined measurement
1	1	1
0.18	6.7×10^{-3}	0.17
7.6×10^{-4}	1.5×10^{-8}	2.8×10^{-3}

Table 4-1: Eigenvalues of the Fisher information matrix, normalized to the largest eigenvalue, for measurement of a quartz sample at two modulation frequencies, treated either as separate measurements or as one combined measurement. Individual measurements, especially at low modulation frequency, have smallest eigenvalues orders of magnitude smaller than the largest.

0.3 MHz modulation

	K_{quartz}	$c_{v,quartz}$	$G_{interface}$
K_{quartz}	1.000	0.328	−0.639
$c_{v,quartz}$	0.328	0.239	−0.062
$G_{interface}$	−0.639	−0.062	0.579

10 MHz modulation

	K_{quartz}	$c_{v,quartz}$	$G_{interface}$
K_{quartz}	1.000	0.998	−0.100
$c_{v,quartz}$	0.998	0.996	−0.100
$G_{interface}$	−0.100	−0.100	0.023

Combined measurement

	K_{quartz}	$c_{v,quartz}$	$G_{interface}$
K_{quartz}	1.000	0.718	−0.325
$c_{v,quartz}$	0.718	0.679	−0.084
$G_{interface}$	−0.325	−0.084	0.256

Figure 4-3: Fisher information matrices, normalized to the largest diagonal element for easier comparison, for measurement of a quartz sample at high and low modulation frequency, treated as separate measurements or as one combined measurement. Measurement at low frequency leads to very large off-diagonal terms between thermal conductivity and heat capacity of quartz, indicating a high covariance in the fitting of those parameters.

conductivity and the quartz thermal conductivity without additional measurement. However, as highlighted by the additive nature of FIMs, measurement at both frequencies would be more powerful still. As shown in Figure 4-3, most values in the normalized FIM for a combined measurement at both frequencies are intermediate between those for measurement at either modulation frequency. The key result arises when examining the eigenvalues of the combined matrix: the third eigenvalue is nearly a factor of four larger than for measurement at either modulation frequency alone. As might be expected, simultaneous fitting of measurement at different measurement conditions makes solving for multiple parameters more feasible. If it were necessary to solve for all three of these parameters, calculation of the FIM could be used to determine what measurements would allow such fitting.

4.2.2.2 FIM: Conclusions

The FIM is a powerful tool for designing experiments and determining what can be solved for within a model. Only a few of its applications are described here—much more can be done, and done with greater mathematical rigor, but such calculations are beyond the scope of this work.

4.3 More sophisticated fitting: emcee

When considering fitting to additional parameters of a TDR model, it becomes desirable to find more sophisticated fitting methods. Each parameter considered is a new dimension of parameter space to explore, and the interactions among parameters become important to consider. To better address these factors, the use of Markov Chain Monte-Carlo (MCMC) methods was explored. MCMC methods are widely used, especially for the fitting of

multiparameter models and noisy data, as they provide an efficient way to determine the probability distributions of possible parameter values even for problems with many dimensions.[44,45] They also make it straightforward to determine how uncertainty in one measurement parameter affects the fitting of another parameter (a technique known as marginalization over nuisance parameters)—in fact, an MCMC-generated sample automatically provides the marginalized distribution.[44]

Though selection of the most effective MCMC method would be a rich topic, for the purposes of this work the Python package emcee[44] was chosen based on accessibility and ease of use. It uses an MCMC method similar to that proposed by Goodman and Weare.[44,46]

The use of emcee starts with defining a set of "walkers," each of which is initialized to a set of possible parameter values (e.g. thermal conductivity, heat capacity, etc.). In this work, initial values were chosen based on random perturbations from an initial guess for each parameter. After initialization, each walker then is moved ("stepped") by a Markov Chain-based method to find combinations of parameter values that provide better values of an objective function. The objective function should drive the parameter values towards a fit that represents the data. If sufficient steps are taken that the walkers can appropriately explore the parameter space, the distribution of their locations will provide a sample of the probability distribution of parameter values—that is, give estimates for the parameters of the model.[44]

When using emcee, the objective function is user-defined, and one appropriate choice is to use the *log likelihood* that the observed data would be measured if the model were correct.[47] This likelihood depends on both the model prediction—values near the prediction are most likely if the prediction is correct—and the noisiness of the system—in a noisy system, values far from the "true" value will be recorded more frequently. For this work, noise was approximated as being Gaussian, meaning that the likelihood of a given deviation between the model prediction and the measured value was given by a normal distribution. The standard deviation of the distribution was determined by the scatter of the experimental data, for example by fitting the experimental data with a low-order polynomial to account for most of the trend and taking the standard deviation of the residuals of that fit. For Gaussian noise with standard deviation σ, the likelihood of measuring a value x_n given a predicted value μ is

$$\mathcal{L} = \frac{1}{\sqrt{2\pi\sigma^2}} \exp\left(-\frac{1}{2}\frac{(x_n-\mu)^2}{\sigma^2}\right) \tag{4-7}$$

so for a set of values $\overrightarrow{x_n}$, the log likelihood can be shown to be

$$\mathcal{LL} = -\frac{N}{2}\log(2\pi\sigma^2) - \frac{1}{2\sigma^2}\sum_{n=1}^{N}(x_n-\mu_n)^2 \tag{4-8}$$

Since the noise level σ was a property of the measurement, not of the model, this meant that the first term was constant throughout the fitting and the second, proportional to the sum of the squared residuals, was optimized by the emcee fitting. It should be noted that σ was different between measurements, so when multiple data sets were fit simultaneously, not all residuals were weighted equally.

The definition of the objective function can also take other information into account. For example, prior knowledge of parameter values can be introduced. Most simply, unphysical parameters can be prevented by defining the objective function to be negative infinity (the worst possible value) outside of the region of acceptability. More nuance, such as expected values with some uncertainty, can also be considered, for example by adding appropriate terms to the

objective function to penalize unlikely values. An example of this is discussed below for the case of the suspended MoS_2 data.

One of the key values of using emcee is that as well as providing the ability to assess the most likely values of parameters, it allows assessment of uncertainty in their values and covariance among parameters. Because the distribution of walker locations samples the possible parameter space, and walkers are driven towards values that give high likelihood, the distribution of walkers gives a good estimate of the distribution of possible parameter values. For parameters which do not strongly affect the likelihood, the walkers will only weakly be driven toward the maximum likelihood value and will probably remain distributed in a wide range around it; for those which do strongly affect the likelihood, the distribution will probably be tighter. The width of this distribution gives an assessment of the uncertainty in the fit—the measured data provides less information about parameters which do not strongly affect the model, so their uncertainties remain higher. More powerfully, since the walkers take on values for all fit parameters simultaneously, looking at the distribution of walkers across two or more parameters allows estimation of the covariance between them. For example, if walkers that sampled higher values of one parameter also sampled higher values of another, it indicates that the estimates of those two parameters are positively correlated. In general, parameters with similar sensitivities will be correlated, but looking at the sampling of the posterior probability distribution as sampled by emcee provides a more direct measurement.

4.3.1 Example: Monolayer MoS_2 with uncertain phase correction

The methods described above were used to fit the data for suspended monolayer MoS_2. Several parameters were uncertain, with the property of interest being the thermal conductivity of the sample. One recognized source of inaccuracy was uncertainty in the phase correction of the measured data: the theory described in Chapters 2 and 3 assumes that the out-of-phase signal from the lock-in amplifier corresponds to the real part of the sample response, and the in-phase component corresponds to the imaginary part. As discussed, the measured data must be corrected such that this is true by adding an appropriate phase offset such that the out-of-phase signal is constant across zero delay time. However, with a noisy signal and small changes at zero delay time, it can be hard to determine the phase offset with certainty, and this uncertainty can impact the fitting result. To account for this, an estimate of the phase offset was made manually as a starting guess, but the phase offset for each measurement was allowed to be a fitting parameter. To drive the system toward appropriate values, a term was added to the objective function for the fit which penalized results with discontinuities in the out-of-phase signal at zero delay time. This term was based on the log-likelihood that a given discontinuity would be measured based on the noisiness of the signal:

$$\mathcal{LL} = -\frac{\Delta Y^2_{across\ t=0}}{2\sigma^2_{mag}} \tag{4-9}$$

where σ_{mag} is the standard deviation of the magnitude of the measured TDR signal, and the $-\frac{1}{2}\log\left(2\pi\sigma^2_{mag}\right)$ term that would make the equation the log-likelihood of a Gaussian was dropped, since it does not vary with the model parameters. Combined with Equation (4-8), this gave an objective function of

$$-\frac{N}{2}\log(2\pi\sigma^2) - \frac{1}{2\sigma^2}\sum_{n=1}^{N}(x_n - \mu_n)^2 - N * \frac{\Delta Y^2_{across\ t=0}}{2\sigma^2_{mag}} \tag{4-10}$$

where the phase correction penalty (Equation (4-9)) was multiplied by N in order to have an equal effect regardless of the number of time points considered.

Walkers were then initialized with values near the starting estimates, allowed to explore the parameter space, and once they converged, their distribution was assessed to measure the most likely parameter values based on the data. The paths of the walkers through parameter space are shown in Figure 4-4, and the summary plot of their positions once they had settled (taken to be beyond 600 steps) are shown in Figure 4-5a. To visualize the multi-dimensional space, the distributions for each pair of parameters are plotted, as well as the univariate distribution for each parameter. The pairwise plots allow visualization of the covariances of the parameters—for example, the values of $(\frac{dn}{dN})/(\frac{dn}{dT})$ (labeled dn_coeff) are not strongly correlated with the values of the thermal conductivity (labeled kr), but the values of the phase corrections are. This indicates that reduction in the uncertainty of the phase correction could further reduce uncertainty in the fitted thermal conductivity, and that systematic errors in phase correction could lead to erroneous values of thermal conductivity. Figure 4-5b shows the raw data with the fitted values of phase correction applied, plotted with the model calculated with the fitted parameters. The fitting routine was able to capture the behavior of the measured data.

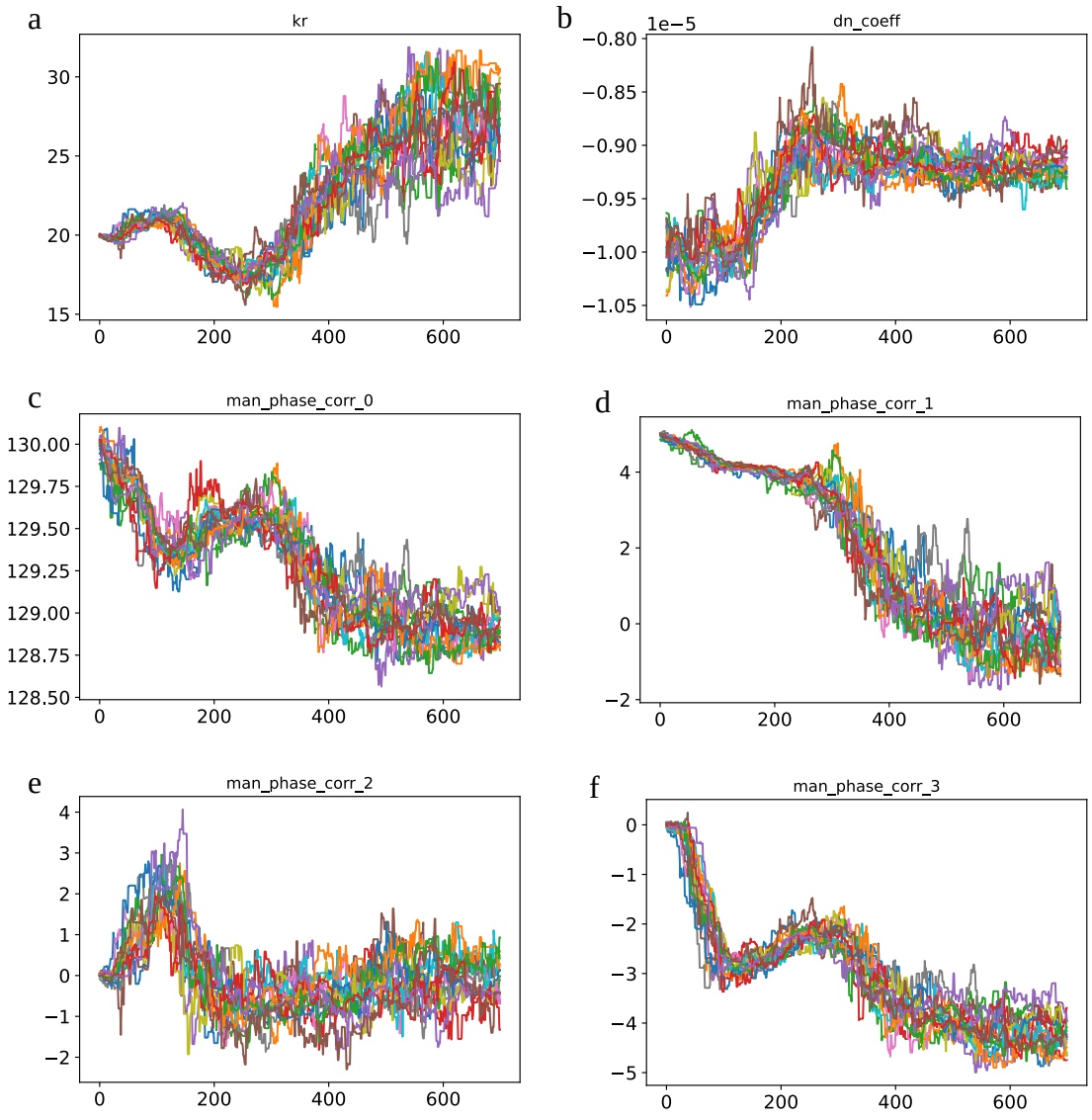

Figure 4-4: Paths of the "walkers" involved in an emcee fit through parameter space. The parameters allowed to vary were: a) sample thermal conductivity, b) $(\frac{dn}{dN})/(\frac{dn}{dT})$, and c-f) the phase corrections for each data set. See text for a description of the objective function. For each walker, there is one line on each plot, showing its value for each parameter at a given step in the calculation. The x axes show the number of MCMC steps taken. This system was treated as having settled to consistent values for steps beyond 600.

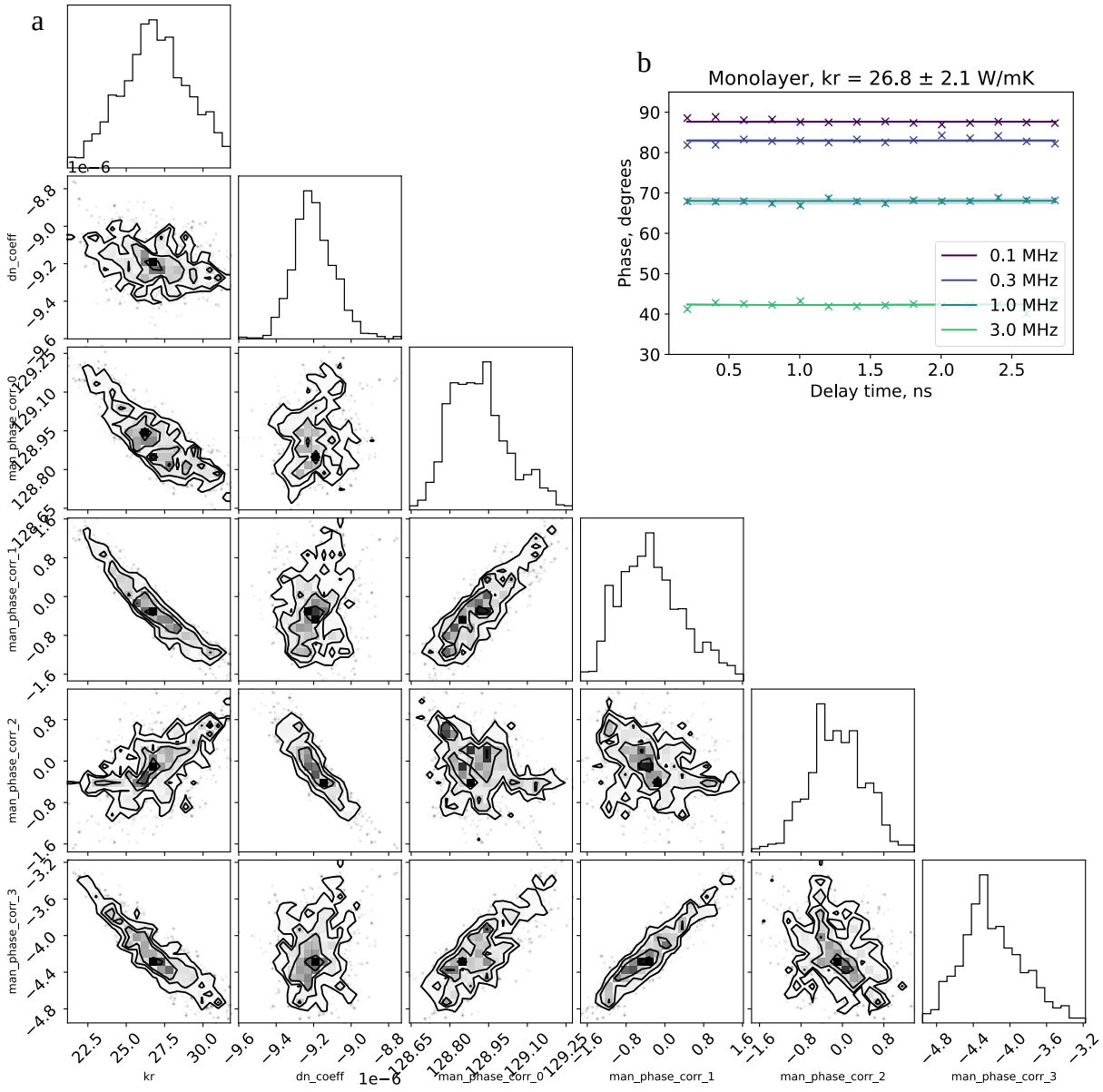

Figure 4-5: a) The corner plot summarizing the distribution of parameters of the walkers shown in Figure 4-4 for steps beyond 600. The individual histograms give the distributions for each parameter separately; the other plots give the contours of the 2D histograms for each pair of parameters. Some pairs, such as the thermal conductivity (kr) and each of the phase corrections (man_phase_corr_i) show stronger correlations than others, such as the thermal conductivity and $(\frac{dn}{dN})/(\frac{dn}{dT})$ (dn_coeff). This is identifiable by the distortion of the 2D histogram along a line. b) The plot showing the calculated fit (lines) with the experimental data (symbols) with the fitted phase corrections applied, showing that the model has found a plausible fit. The shaded regions represent the change in the model when the thermal conductivity is changed within its uncertainty, which is extracted from the standard deviation of the distribution from a). Note that final fits reported in Chapter 7 also allowed for uncertainty in electrical diffusivity and carrier lifetime, giving a slightly different fitted value for thermal conductivity.

4.4 Conclusions

Because time domain reflectance data involves a nonlinear multiparameter model, the question of how to best fit the model is not an easy one to answer. Though straightforward approaches such as the use of the Python curve_fit package do provide results, they hide many of the details of the process, such as the identification of the number of parameters that can be fit. Tools such as the Fisher Information Matrix can be used to assess the information content of a signal based on the predicted model, and more sophisticated fitting tools such as the Python package emcee allow more careful definitions of desired objective functions and can directly account for uncertainty in multiple input parameters. This allows clearer, more rigorously justifiable outcomes.

5 Thermal conductivity near mental-insulator transitions

5.1 Metals, insulators, and metal-insulator transitions

5.1.1 Metals vs insulators

In standard band theory, solids contain some ranges of electron energies which are allowed, and others which are forbidden. The distinction between metals and insulators comes from which of these levels are occupied. In metals, the transition from the occupied energy states to unoccupied states happens within a band of allowed energies, so the energy required to move an electron to an unoccupied state is small. In insulators and semiconductors, the lower energy bands are full, and a gap separates the highest occupied state from the lowest unoccupied state, so an electron must gain sufficient energy to overcome this gap before conduction can occur.[26] For this reason, the electrical conductivity of metals is generally much higher than that of semiconductors and insulators. At temperatures near room temperature, the electrical conductivity of metals generally decreases with further heating, because electron-phonon scattering is increased, whereas in semiconductors and insulators increases in temperature generally lead to the availability of more electrons to carry current, increasing electrical conductivity. Thus, looking at the change in electrical conductivity with temperature can help distinguish metallic from non-metallic behavior.

In the simplest case, a metal results when a material has a partially filled electron band, and a semiconductor or insulator results when some bands are full and others are empty (ignoring temperature effects). However, in some materials multiple bands overlap, so even though a naive accounting might lead to one being full and the next empty, there is no bandgap between them and the material is a metal. In some materials that might be expected to be metals, various effects lead to nonmetallic behavior. For example, the presence of a sufficient number of lattice defects can lead to the localization of some electron states and, if these replace the conductive states, to nonmetallic behavior—an Anderson insulator. Interactions between lattice deformations and electrons can lead to the formation of a static periodic deformation. This increases the effective unit cell of the material and opens a gap in what would otherwise be one electron energy band, leading to a Peierls insulator. Additionally, interactions between electrons can influence their behavior, potentially leading to an energy penalty equivalent to the opening of a band gap. Depending on the type of interaction, materials in which this occurs are called charge density insulators or Mott insulators. In many cases, several of these effects are present and all contribute to the development of insulating behavior.[48,49]

5.1.2 Metal-insulator transitions

The most obvious signature of a metal-insulator transition is a substantial change in the electrical conductivity of a material. Assessment of the temperature dependence of the electrical conductivity, or other confirmation of the band structure, can determine that the material is metallic on one side of the transition and not on the other. In some cases, changes in lattice structure cause or accompany the transition, for example because changes in electron orbital hybridization lead to both structural rearrangement and the overlap of previously separate electron bands. In others, the lattice structure is the same on both sides of the transition.

Frequently, the insulating state is a Peierls, Mott, Anderson, or charge-density insulator, but this is not a requirement.[48]

5.2 The metal-insulator transition in vanadium dioxide (VO_2)

One material that has seen substantial research interest in much of the last 50 years is vanadium dioxide, VO_2. It has a metal-insulator transition at 340 K, which shows some Peierls-like and some Mott-like behavior. There is an accompanying structural change, from monoclinic in the insulating phase to tetragonal in the metal, which is associated with a change in the energy of the vanadium d-band electrons.[50] The bands which are split across the band gap in the insulating state are degenerate and partially filled in the metallic state. Despite the change in structure through the phase transition, the phonon contribution to the thermal conductivity is not expected to change substantially—a reduction of 13% in the metallic state compared to the insulting is expected.[1] The electrical conductivity, however, changes by several orders of magnitude, from $3*10^3$ S/m in the insulator to $9*10^5$ S/m in the metal. If the Wiedemann-Franz Law holds, the electronic contribution to the thermal conductivity would also be expected to change dramatically, leading to a sudden increase in the total thermal conductivity upon entering the metal phase. Fascinatingly, experimental results showing a range of thermal behaviors have been reported: from small decreases in thermal conductivity on entering the metal state in bulk samples[51] as shown in Figure 5-1a, to no detectable change anywhere in the range of 25 to 85 °C, also in the bulk,[52] to small to moderate increases in thin films[2,53] and nanobeams[1] (Figure 5-1 b-c). The fact that in some samples the thermal conductivity does not increase or increases minimally across the transition to the metallic state suggests that there is some mechanism by which the electrical conductivity is not reflected in an electronic contribution to the thermal conductivity—that is, the Wiedemann-Franz Law does not hold, and the electrons are not behaving as quasiparticles, but rather move in a correlated manner. Absent errors in multiple experiments, it also appears that this mechanism is not present in all samples, and electronic conductivity is proportional to thermal conductivity under certain circumstances. Thus far, it is in thin film samples that this appears to be the case, so it is possible that substrate-induced strain or grain size effects are relevant, but more systematic study is needed.

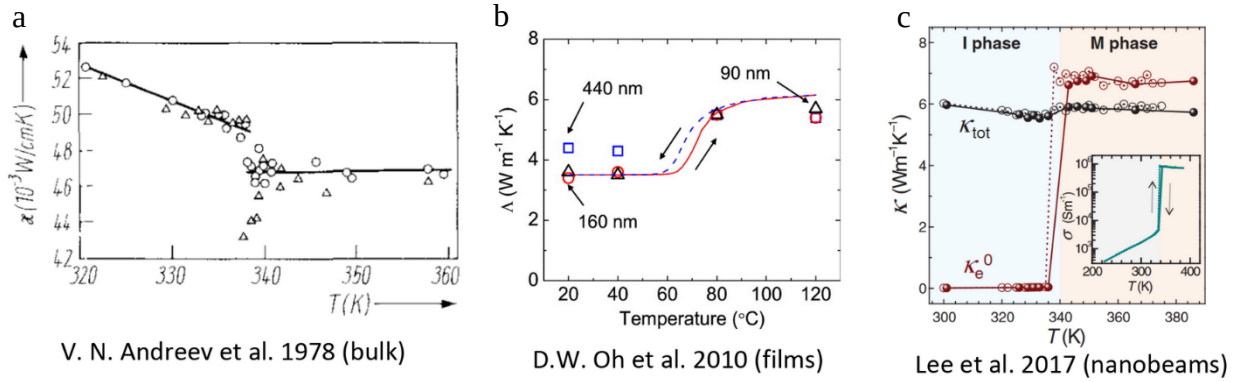

V. N. Andreev et al. 1978 (bulk) D.W. Oh et al. 2010 (films) Lee et al. 2017 (nanobeams)

Figure 5-1: Thermal conductivity of various VO_2 samples. a) The bulk samples measured by Andreev et al[51] showed a slight decrease of approximately 0.3 W $m^{-1}K^{-1}$ in thermal conductivity at the transition into the metallic state. Circles and triangles represent two different samples. b) Thin film samples showed an increase in thermal conductivity of nearly 2 W $m^{-1}K^{-1}$, comparable to the expected change in κ_e.[2] Similar results were reported by Kizuka et al.[53] c) Single crystal nanobeams showed a small increase in total thermal conductivity (black line), but far less of a discontinuity than expected given the electronic behavior (red line).[1]

5.2.1 WVO_2

One way to modify the behavior of VO_2 in a controlled manner is through the addition of dopants. For example, tungsten (W) doping is known to lower the transition temperature of VO_2,[54] and is reported to lead to a larger discontinuity in thermal conductivity across the metal-insulator transition, despite causing a slight decrease in the electrical conductivity of the metallic state.[1] Though this shows a behavior more similar to that predicted by the Wiedemann-Franz Law, Lee et al argue that it does not reflect a restoration of quasiparticle transport.[1]

5.3 Measurement of thermal conductivity

5.3.1 VO2

Experiments focused on VO_2 and WVO_2 films, specifically samples consisting of 300 nm of VO_2 or $W_{0.01}V_{0.99}O_2$, grown by pulsed laser deposition on a silicon nitride coated silicon substrate. The electrical behavior of the films was measured by a four point probe measurement following the van der Pauw method, and the temperatures for the metal-insulator transition were consistent with expectation. For TDTR measurements, 80 nm of aluminum was deposited on the sample layer by e-beam evaporation to serve as the transducer layer. The sample was attached to a thermal stage with silver paste, and TDTR measurements were taken. A spot size of approximately 10 um was used in order to achieve sufficient signal intensity but minimize sensitivity to imperfections in spot shape, and a modulation frequency of 9.5 MHz was used to maximize sensitivity to the properties of the sample layer. The sample temperature was swept across the metal-insulator transition, with TDTR measurements taken at 5 K or 10 K intervals, for VO_2 and WVO_2, respectively.

In order to determine materials properties from TDTR measurements, the collected data were compared to the predictions from a thermal model of the system, and the parameters of the model were adjusted to find the best fit. In general, the measured thermal behavior depends on the thermal conductivity, heat capacity, and thickness of each sample layer, as well as the conductivity of the interfaces between layers.

The properties of the silicon nitride layer were determined by a separate measurement of a control sample with no additional film, and found to be nearly constant with temperature, as shown in Figure 5-2. The measured values were used in the fitting for the VO_2 and WVO_2 samples.

In the 9.5 MHz measurements, sensitivity to layers below the sample layer was minimal, (Figure 5-3a) so fits were performed to the thermal conductivity of the sample and that of the interface between the sample and the aluminum. For temperatures far from the metal-insulator transition, satisfactory fits were achieved by assuming that the sample heat capacity would match

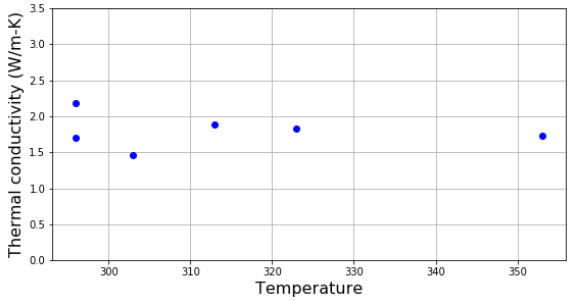

Figure 5-2: Measured thermal conductivity of the silicon nitride layer as a function of temperature. These results were used in fitting for the VO_2 and WVO_2 samples.

the reported literature values for bulk VO_2,[55] but for temperatures across the transition, such an assumption led to non-physical parameter values.

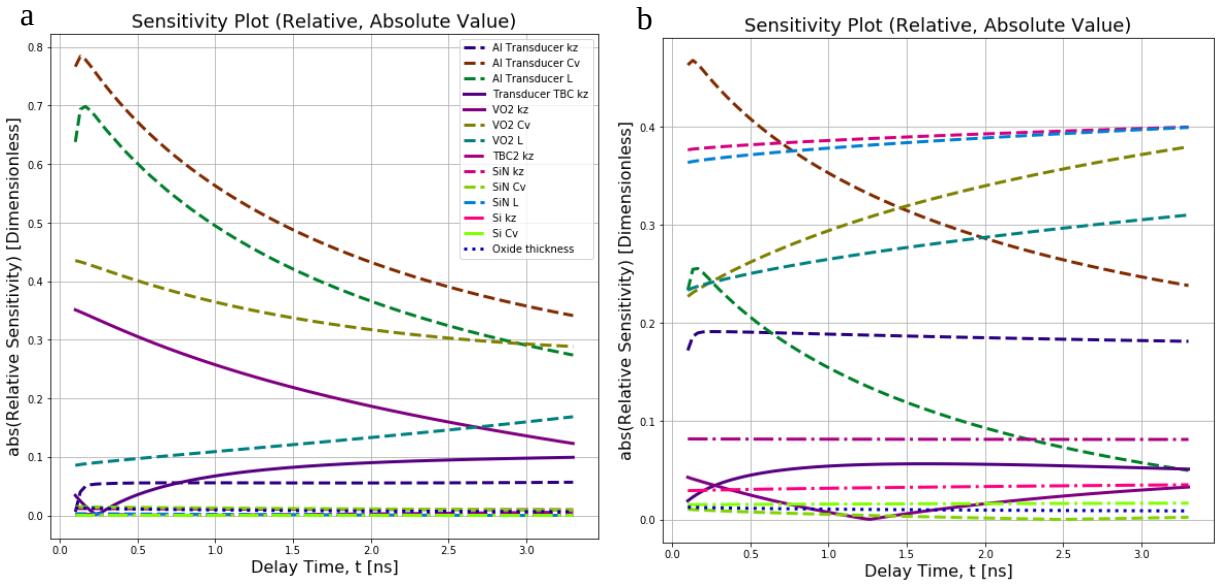

Figure 5-3: Sensitivity plots for the VO_2 sample measured at a) 9.5 MHz and b) 0.94 MHz. Measurements at higher frequencies are more sensitive to layers nearer the surface, so measurement at 9.5 MHz was less sensitive to the SiN properties. However, measuring at 0.94 MHz as well allowed simultaneous fitting to thermal conductivity and heat capacity.

To better understand the thermal conductivity behavior during the transition, better understanding of the heat capacity behavior in these samples was needed. The 9.5 MHz measurements were primarily sensitive to the thermal effusivity of the sample, so the conductivity and heat capacity affect the signal very similarly. To make separate determination of the two parameters possible, measurements were also made at 0.94 MHz, increasing the thermal penetration depth and so by comparison reducing the effective thermal thickness of the sample layer. At this frequency, the measurement is substantially more sensitive to the sample heat capacity than to its thermal conductivity but is also more sensitive to the properties of underlying layers, adding uncertainty to the result. (Figure 5-3b) However, by assuming that sample properties should be the same in both measurements and finding the parameters that best fit measurements at both frequencies, it is possible to determine values for both heat capacity and thermal conductivity of the sample. This was done using the Python package emcee, as discussed in section 4.3.

However, the heat capacities measured by this technique were substantially lower than the literature values, though they showed qualitatively similar behavior. (Figure 5-4) This degree of deviation from literature values is unlikely to be physical, and likely indicates an inaccuracy in the model or fitting method, but approaches such as trying different initial values of parameters did not yield improved results. As these are volumetric heat capacities, some drop in heat capacity compared to the bulk could be expected if the thin film deposition was not of sufficient

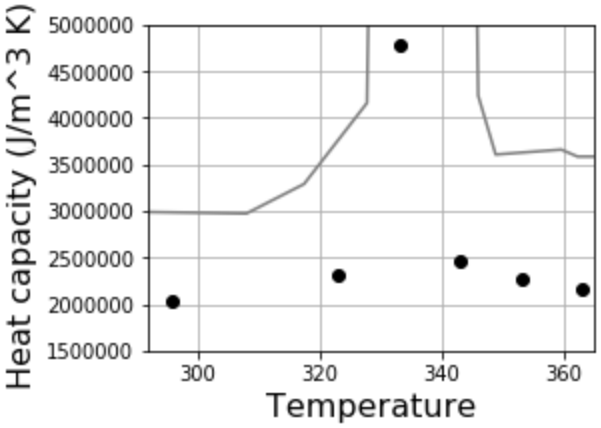

Figure 5-4: fitted heat capacity for the VO2 sample as a function of temperature (points) compared to literature data (grey line). Though the expected increase in heat capacity during the MIT was observed, fitted values were overall ~30% smaller than literature values.

quality to provide a fully dense sample, but this is unlikely to be a large enough effect to explain the discrepancy.

Given the lack of a definitive value for the heat capacity across the MIT, three approaches to were used: 1) the use of literature data from the bulk,[55] including the very high heat capacity across the transition, 2) the use of the same literature data, but the heat capacity across the peak estimated by linear interpolation from the two sides to approximately ignore the increase from the enthalpy of the transition, and 3) the use of the fitted values for heat capacity. Combined, approaches 1) and 2) can be seen to provide bounds on the value of the thermal conductivity, as the more gradual transition expected in the polycrystalline thin film compared to a bulk single crystal likely leads to a shorter, broader peak in heat capacity as a function of temperature. These results are plotted together in Figure 5-5.

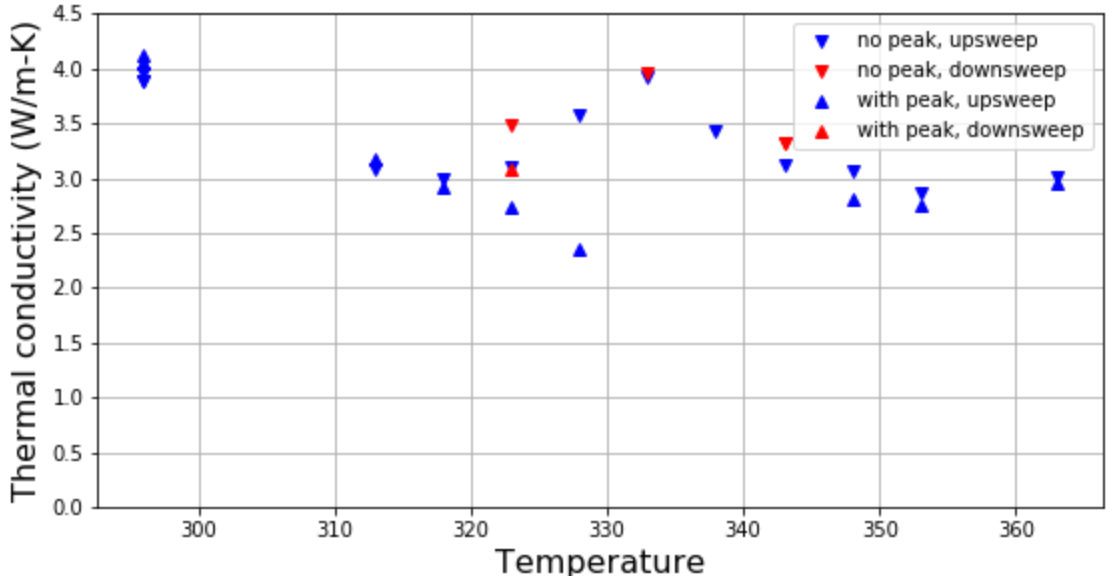

Figure 5-5: Fitted thermal conductivities for VO_2 as a function of temperature, showing results for using literature values for the heat capacity and including (upward pointing triangles) or interpolating to avoid (downward pointing triangles) the peak in the heat capacity data caused by the phase transition. Since the literature data was for a single crystal and the measured film was polycrystalline, it is expected that the film heat capacity was between the two values used, and these data points can be seen as providing bounds on the thermal conductivity.

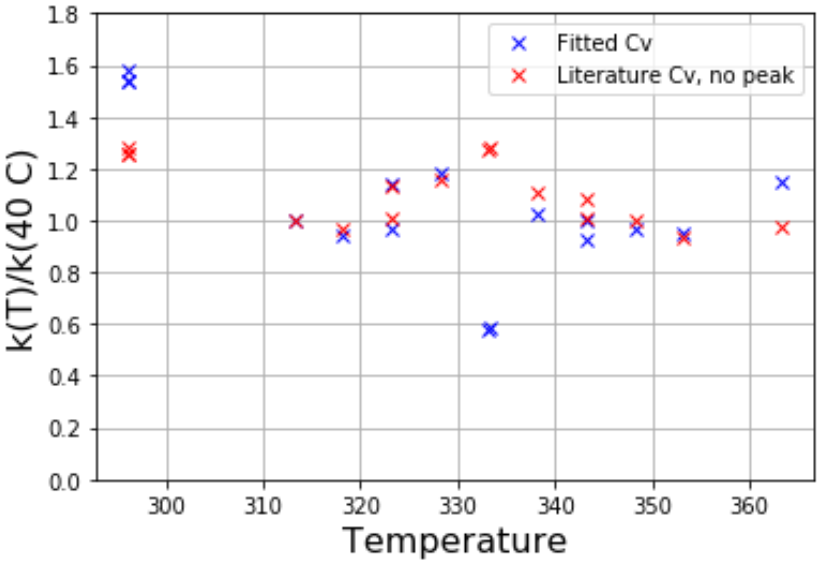

Figure 5-6: Comparison of the behavior of the fitted thermal conductivity when using fitted and literature data for the heat capacity. Though the lower fitted values for heat capacity led to higher resulting values for thermal conductivity, normalization to the value found for 40 °C highlights that the trend in thermal conductivity was similar regardless of the choice of heat capacity.

As mentioned above, the (volumetric) heat capacities found by fitting at multiple measurement frequencies were consistently lower than those reported for a bulk sample. Such a significant difference is unlikely to be physically reasonable, so values found from approach 3) should be used with caution. However, using these values still gave results qualitatively similar to those from approach 2), with the exception of the values for 333 K and the highest and lowest measured temperatures. This is highlighted in Figure 5-6 which shows the fitted values of the thermal conductivity, normalized to the value at 313 K.

To better see the direct effect of the phase transition, a set of measurements was taken with delay time fixed, and temperature increased and then decreased across the transition. This was done at modulation frequencies of both 9.5 MHz and 0.94 MHz. In the first case, the measurement is sensitive to the thermal conductivity and heat capacity of the VO2, as well as the thickness and heat capacity of the aluminum layer. Sensitivity to other properties is significantly smaller. In the second case, there is minimal sensitivity to the thermal conductivity of the VO2, but due to the larger thermal penetration depth, other parameters such as the thermal conductivity of the silicon nitride are also relevant. However, these are expected to vary less with temperature than the VO2 properties. Thus, minimal difference is expected between the 0.94 MHz signal in the insulating and metallic states.

As shown in Figure 5-7, the measured ratio of the in- and out-of-plane TDTR signal components shows a clear peak across the MIT for both modulation frequencies. This peak is attributed to the increased heat capacity across the MIT, which is validated by its being positive at higher modulation frequency, where the sensitivity to heat capacity is positive, and negative at lower modulation frequency, where the sensitivity to heat capacity is negative. Without quantitative accounting for the magnitude of the heat capacity, determination of other properties within the MIT is difficult. For both modulation frequencies, no large change in signal from one side of the phase change to the other was observed. The heat capacity is expected to be about 20% higher in the metallic state than in the insulting state, which would cause an increase of a

few percent in ratio on entering the metallic state in the 9.5 MHz case and a decrease of a few percent in the 0.94 MHz case (corresponding to the sign of the sensitivity to heat capacity). In the 9.5 MHz case any other difference would likely be due to a difference either in VO2 thermal conductivity or the heat capacity of the aluminum transducer. The aluminum heat capacity is expected to increase by approximately 3% between 40 °C and 90 °C,[56] which would be expected to cause a change in ratio of less than the noise level of the measurement. Thus, any change could be attributed to changes in VO2 thermal conductivity, and the observation of similar signal in the insulating and metallic states suggests that the thermal conductivity of the VO_2 was largely constant. Minimal change was observed between the behavior at 40 °C and 80 °C at 0.94 MHz as

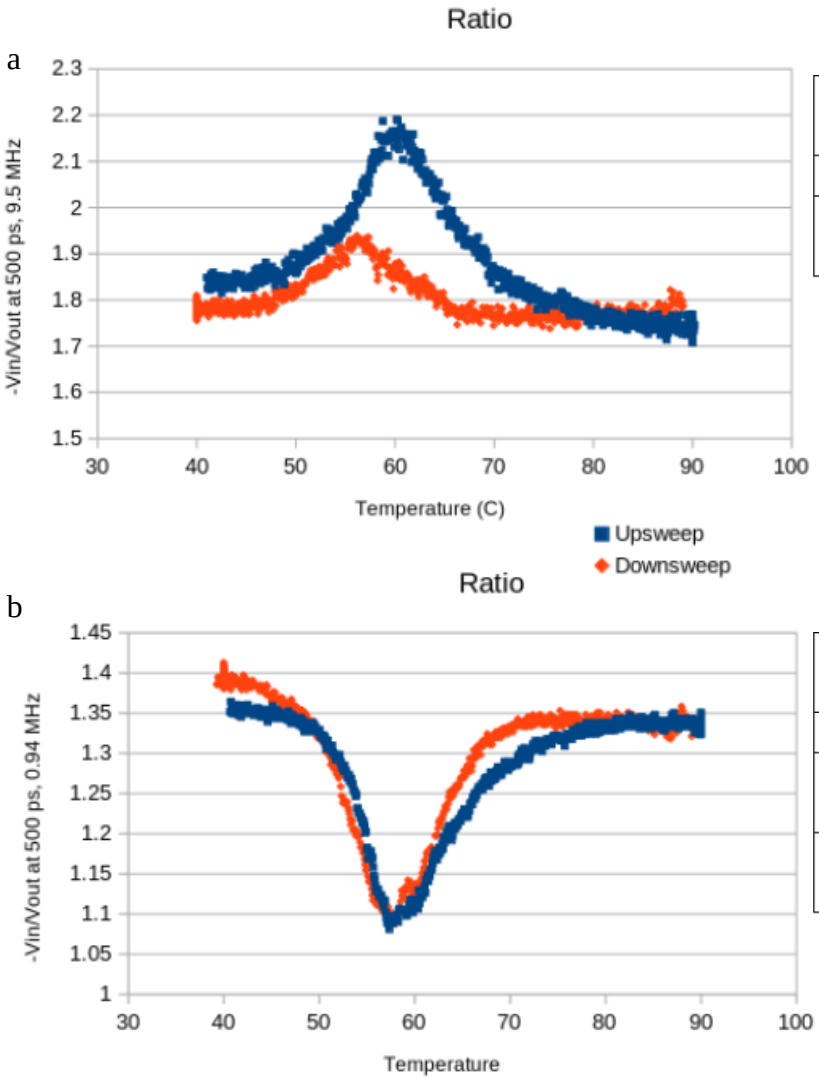

Significant sensitivities:

VO_2 thermal conductivity	0.31
VO_2 heat capacity	0.40
Aluminum heat capacity	-0.60

VO_2 thermal conductivity	0.03
VO_2 heat capacity	-0.26
Aluminum heat capacity	-0.40
Silicon nitride thermal conductivity	0.38

Figure 5-7: The ratio of in- to out-of-phase TDTR signal at a delay time of 500 ps and modulation frequency of a) 9.5 MHz and b) 0.94 MHz, as a function of temperature across the VO_2 MIT, as well as the significant values of the sensitivity to model parameters at those conditions. The sign of the peak seen across the MIT corresponds to the sign of the sensitivity to heat capacity, which is expected to peak during the transition. The small change in signal from one side of the transition to the other implies a small change in properties to which there was significant sensitivity—in particular, the small change in a) implies a small change in thermal conductivity.

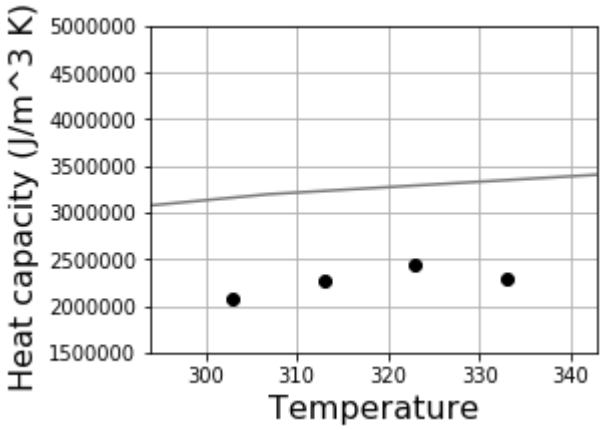

Figure 5-8: Fitted heat capacity for WVO_2 (points) compared to literature data for VO_2 with interpolation replacing the peak caused by the VO_2 phase transition (gray line). As with VO_2, the fitted values were about 30% lower than the literature data.

well—in this case, sensitivity to VO_2 thermal conductivity was minimal, but this supports the assertion that the aluminum properties did not vary much across that temperature range.

In short, similar thermal conductivities were observed in the insulating and metallic states for this VO_2 sample.

5.3.2 WVO_2

For WVO_2, heat capacity was 1) estimated from the same VO_2 literature data[55] with interpolation replacing the peak, and 2) fitted. Again, fitting gave significantly lower heat capacities, (Figure 5-8) though the fitted values were similar to those for VO_2.

Using the approximated literature data for heat capacity suggested a fairly constant thermal conductivity over the measured temperature range, as shown in Figure 5-9; using the fitted values suggested a small decrease in thermal conductivity. In neither case was the difference more than 20%. The comparison of results from the two methods of determining heat capacity are shown in Figure 5-10.

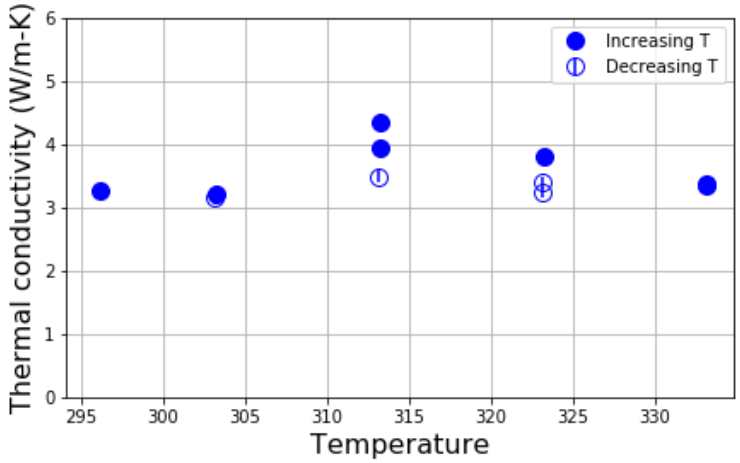

Figure 5-9: Fitted thermal conductivities for WVO2 using the interpolated literature data for VO_2, as a function of temperature. No large change was observed during the MIT.

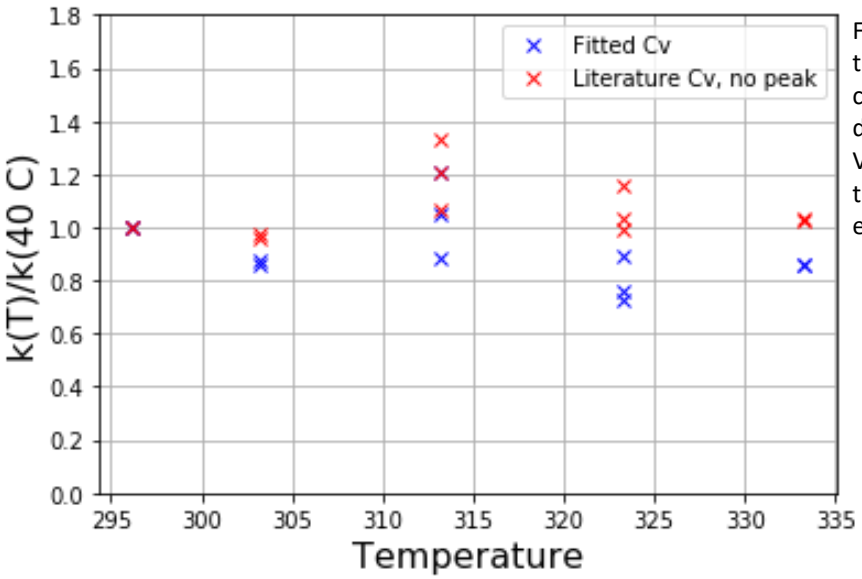

Figure 5-10: Comparison of the trend in the fitted thermal conductivity of WVO_2 with different assumed heat capacities. Values are normalized to the thermal conductivity at 40 °C for easier comparison.

5.4 Assessment of the Wiedemann-Franz Law

In these samples, no substantial change in thermal conductivity was observed across the metal-insulator transition in either VO_2 or WVO_2.

5.4.1 VO_2

In VO_2, the thermal conductivity appeared lessened during the metal-insulator transition, between 325 and 345 K. Given that a mix of metallic and insulating domains are likely present in this temperature range, an increase in phonon boundary scattering is plausible. The transition temperature seen in the thermal results is lower than that determined by the electrical behavior of the samples ($T_{c,electric} \approx 340$ K); this effect was also noted by Oh et al., who attributed it to the higher sensitivity of the thermal measurement to the presence of a small areal fraction of metallic domains.[2] The decrease in the thermal conductivity in the insulating state approaching the transition was larger than expected from literature data, but some decrease is expected due to increased phonon-phonon scattering. However, the magnitude of this drop makes it difficult to estimate the expected lattice conductivity in the metallic state.

More importantly, these samples have a relatively low electrical conductivity in the metallic state. The VO_2 sample has a conductivity of $3.4*10^4$ S/m, which would correspond to κ_e of less than 0.5 $Wm^{-1}K^{-1}$ even if the degenerate Wiedemann-Franz Law held. This is well within the error of measurement, as shown in Figure 5-11, so no conclusive statement about the validity of the Wiedemann-Franz Law in this sample can be made. This low an electrical conductivity is surprising for a VO_2 film in the metallic state, and likely indicates a problem with the sample fabrication. Though these samples were grown according to established recipes, they were grown thicker than usual in order to improve the sensitivity of the TDTR measurement, and this may have led to lower quality.

5.4.2 WVO_2

For the WVO_2 sample, the metal-insulator transition spans a wider temperature range—only the 297 K data point represents behavior in the insulating state, and only the 333 K data point is

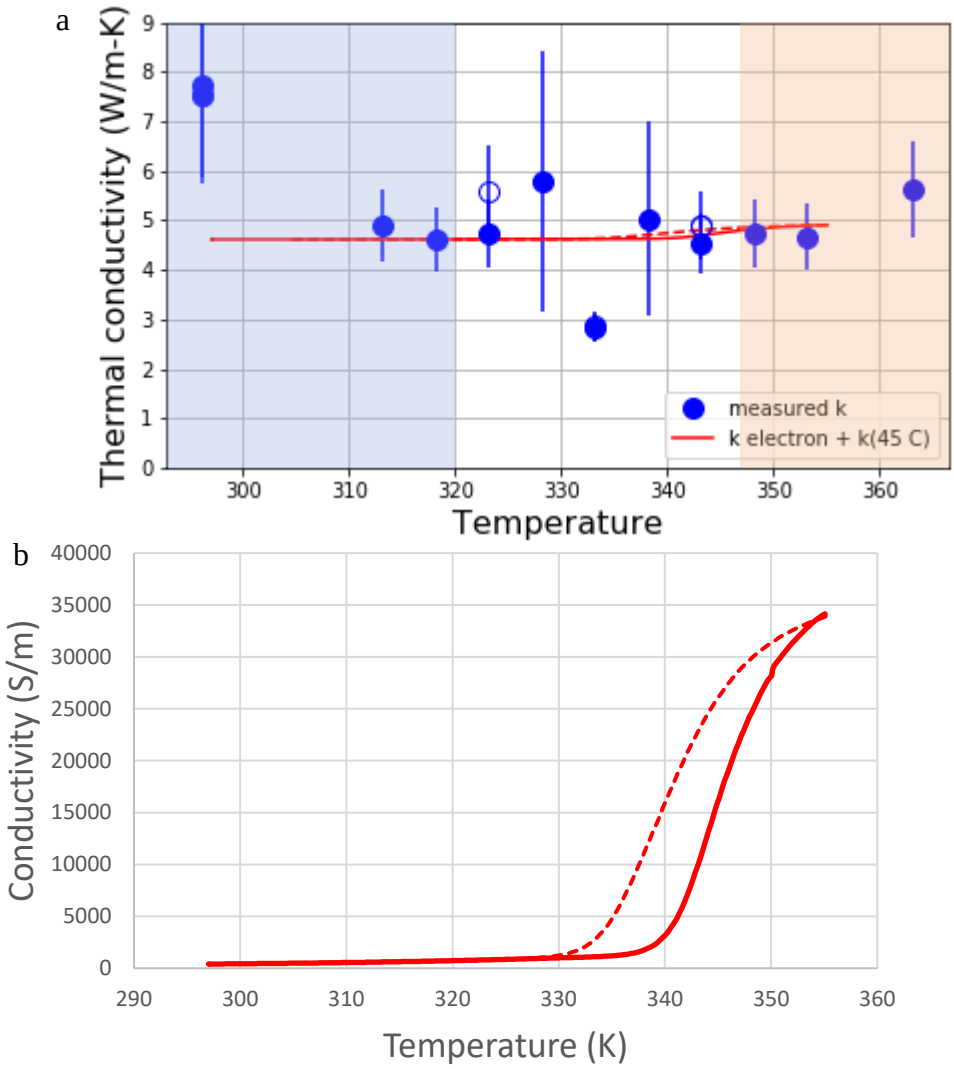

Figure 5-11: a) Measured thermal conductivity for VO_2 across the phase transition (blue), plotted with the expected electronic thermal conductivity if the Wiedemann-Franz Law held, offset by the thermal conductivity at 45 °C for clarity (red). The expected electronic thermal conductivity is very small. b) The measured electrical conductivity of the sample across the phase transition. In both a) and b), the solid red line represents the electrical behavior measured as temperature was increased and the dashed red line that as temperature was decreased.

definitively in the metallic state. This makes it impractical to make statements about the insulating and metallic states in general. The W VO_2 sample does have a higher electrical conductivity in its metallic state at $2.3*10^5$ S/m, corresponding to a possible κ_e of almost 2 $Wm^{-1}K^{-1}$. As shown in Figure 5-12, no corresponding increase in thermal conductivity was seen—the measured thermal conductivity at 333 K was not greater than that at 297 K. Thus, it seems plausible that some degree of Lorentz number suppression is occurring, but without more detailed knowledge of the phonon behavior making a clear statement is impossible.

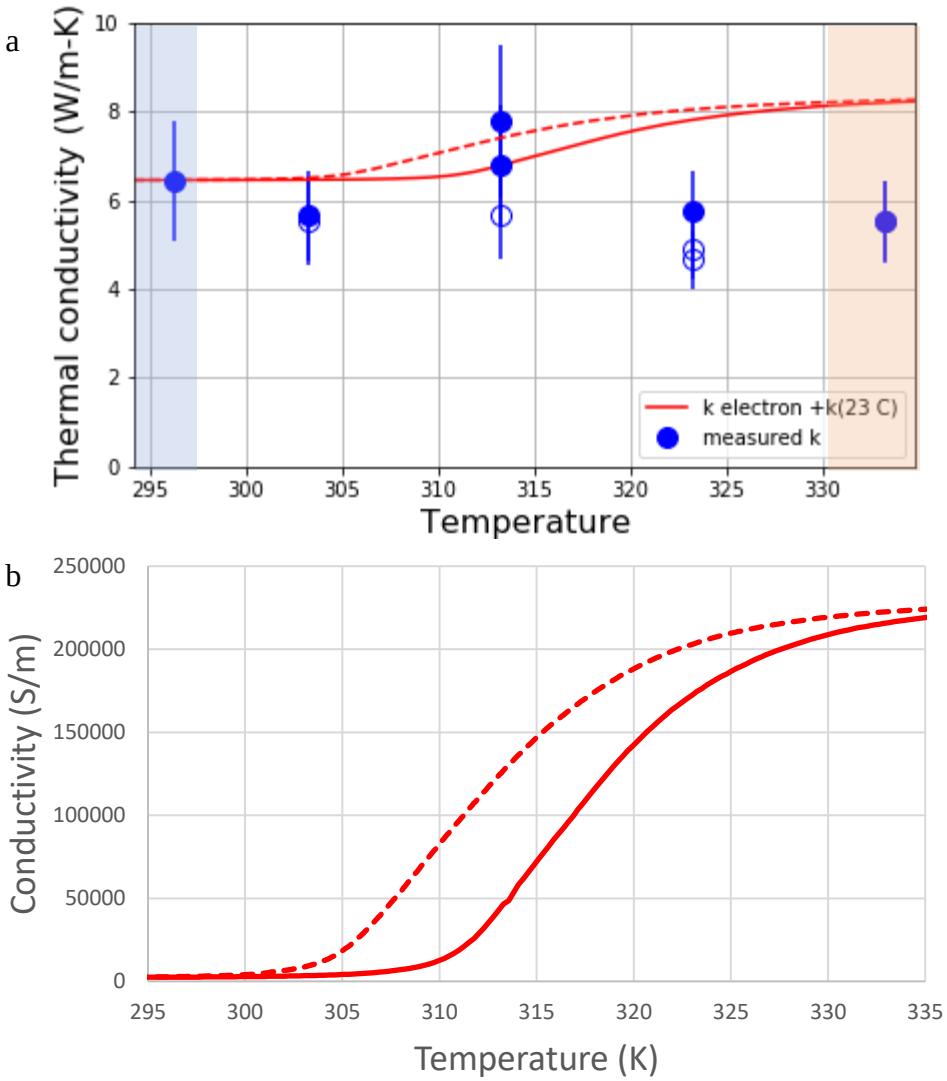

Figure 5-12: a) Measured thermal conductivity for WVO_2 across the phase transition (blue), plotted with the expected electronic thermal conductivity if the Wiedemann-Franz Law held, offset by the thermal conductivity at 23 °C for clarity (red). The measured thermal conductivity does not increase when the electrical conductivity does. b) The measured electrical conductivity of the sample across the phase transition. In both a) and b), the solid red line represents the electrical behavior measured as temperature was increased and the dashed red line that as temperature was decreased.

5.5 Conclusions

In these samples, no obvious change in thermal conductivity was seen when the samples entered the metallic state from the insulating state. In the case of VO_2, however, the electrical conductivity in the metallic state was low enough that minimal change was expected. For the WVO_2 sample, if no Lorentz number suppression was present, a measurable increase in thermal conductivity would be expected if the lattice thermal conductivity were constant. However, insufficient data were collected to make any assertions about the lattice thermal conductivity, so determining whether the near-constant observed thermal conductivity was a result of Lorentz number suppression or a drop in lattice thermal conductivity offset by an increase in electronic

thermal conductivity is not possible. More rigorous conclusions would require measurement of samples with higher electronic thermal conductivity across a wider temperature range, as well as possibly supplemental techniques to study lattice behavior.

6 Transducerless time domain reflectivity measurement of bulk semiconductors

This chapter reproduces the paper "Transducerless time domain reflectance measurement of semiconductor thermal properties," which I published in the *Journal of Applied Physics*. In it, I developed the technique of transducerless time domain thermoreflectance and validated it through measurements of silicon and germanium samples.

6.1 Introduction

The question of how to effectively and accurately measure the thermal properties of materials is a long-standing one. Standard approaches are based on applying heat and monitoring its diffusion, then comparing the measured result to a thermal model.[57] Local measurements require establishing a thermal diffusion length, for example through the use of a modulated heat source. For decades, techniques based on heating via a modulated laser beam have been used, with measurement of the sample response via the photoacoustic effect,[58,59] through photothermal deflection,[60,61] with piezoelectric transducers,[62] or based on reflectivity changes.[63–66] In recent years, time- and frequency-domain thermoreflectance (TDTR[7] and FDTR[67], respectively) have become the dominant approaches. TDTR and FDTR rely on temperature-driven changes in the optical reflectivity of the sample surface,[5] allowing monitoring of temperature changes through the change in reflected intensity of a second laser beam. By detecting the modulation in reflection corresponding to the modulated heating, the thermal response of the sample can be determined.

In their usual applications, both TDTR and FDTR involve the deposition of a thin metal transducer layer on the sample to be measured. This transducer is then the only layer that interacts with either incident laser beam, acting as both heater and thermometer for the rest of the sample. The use of a transducer allows the assumption that the change in reflection is directly related to the sample surface temperature, as the primary component affecting the reflectivity of metals is the distribution of free electrons, which is temperature dependent.[68] With appropriate selection of metal and laser wavelength, the coefficient of thermoreflectivity, dR/dT, can be substantially larger than in an unoptimized system.[21] Additionally, the optical penetration depth of the laser in the metal transducer layer is small, allowing heating to be modeled as occurring at the surface.

However, requiring a metal transducer layer adds complexity and can limit measurement. Deposition of the transducer is a permanent modification of the sample surface, removing the possibility of *in-situ* measurements. In interpreting results, additional parameters such as the thickness and heat capacity of the transducer and the thermal interface conductivity to the sample become important. The conductivity of the transducer-sample interface must be high enough compared to the conductivity of the sample for the measurement to be sensitive to sample properties. For ultra-thin samples or measurements of in-plane conductivities, the transducer acts as a thermal short and suppresses the sensitivity of the measurement to the properties of interest, especially for samples with relatively low thermal conductivities.[69] Thus, a technique that does

not require a transducer layer is desirable. Key differences between measurements with and without a transducer are highlighted in Figure 6-1.

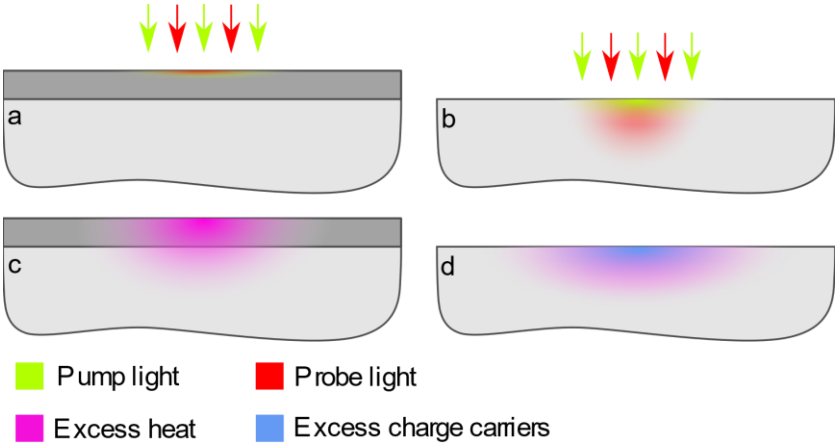

Figure 6-1: a) In a transducer-coated sample, light absorption happens near the surface of the material, whereas b) in an uncoated semiconductor sample, light penetrates into the material. c) In a coated sample, heat must diffuse through the transducer to reach the sample, and no charge carriers are generated. d) In an uncoated sample, heat and charge carriers are both generated and diffuse directly in the sample.

Others have pursued the goal of transducerless thermoreflectivity measurements. Wang et al.[68] and Qian et al.[69] demonstrated the feasibility of FDTR measurements on uncoated samples; however, their thermal model breaks down at short delay times and in materials with long carrier diffusion lengths. Tanaka et al.[70] use a TDTR-like setup, but use a thermal model that is only valid for time scales shorter than those used in many TDTR measurements. By using overlapped pump and probe beams, we avoid the complex optical systems required for the beam-offset techniques of Fournier et al.[57] and Hurley et al.[64]. In this paper, we demonstrate the usage of standard TDTR instrumentation and measurement technique to determine thermal conductivities of semiconductors without the use of a transducer layer. We anticipate that such a technique can extend the range of samples which can practically be measured using existing TDTR equipment.

6.2 Transducerless measurements

The mechanism of TDTR measurements is described in detail elsewhere.[7] TDTR is a pump-probe method in which an ultrafast pulsed laser is divided into two beams, both of which are directed to a sample. Our TDTR setup uses a 565 nm pump beam and an 800 nm probe beam. The pump beam is modulated, typically at a frequency of 0.1-10 MHz, and the probe beam is passed through a mechanical delay stage, temporally separating the incidences of the pump and probe beams by some delay time—in our setup, up to 3 ns. This allows measurement both over the fast (picosecond to nanosecond) timescale of the delay stage and over the slow (microsecond) timescale of the pump modulation.

In transducerless time domain reflectivity measurements, both pump and probe beams are incident directly on the semiconductor sample. We highlight the key processes that occur when a pump pulse strikes our samples in Figure 6-2. In our experiments, the pump beam photon energy, $h\nu$, is greater than the bandgap of our samples, E_g, and the pump has a non-zero penetration depth. When a pump pulse is absorbed, electron-hole pairs with energy $h\nu$ are generated throughout a volume of the sample corresponding to the region of absorption. Within a few

picoseconds, excited carriers thermalize to the lattice temperature and relax to the band edge,[71,72] releasing thermal energy ($h\nu - E_g$). Over the next tens of picoseconds to hundreds of nanoseconds, the photogenerated carriers and the generated heat diffuse into the sample, and the carriers recombine. Assuming primarily non-radiative recombination, this leads to an addition source of thermal energy E_g for each recombination event, serving as an additional distributed heat source. Beyond the photocarrier lifetime, the population of carriers returns to its background level, leaving only the thermal energy which continues to diffuse. At long enough timescales, sufficient spreading of the thermal pulse has occurred that the sample can be treated as having returned to equilibrium. Crucially, for intermediate time scales (nanosecond to microsecond, depending on carrier recombination time), the continued heating arising from carrier recombination means that proper treatment of the sample temperature requires consideration of both generation and diffusion of heat and the behavior of the photoexcited charge carrier population. Accordingly, we coin the term transducerless time domain reflectance (tTDR), highlighting that changes in optical reflectance are modulated both thermally and electronically, as opposed to only thermally as in TDTR. As with traditional TDTR, the sensitivity of the measurement to sample responses across multiple timescales is beneficial—we are able to measure thermal effects both at short delay times, where the sample response is strongest, and at long times when electronic effects are diminished. Additionally, though we do not explore it in this work, we anticipate that the sensitivity of tTDR to both thermal and electronic effects could be used to probe links between variations in thermal and electronic properties of materials.

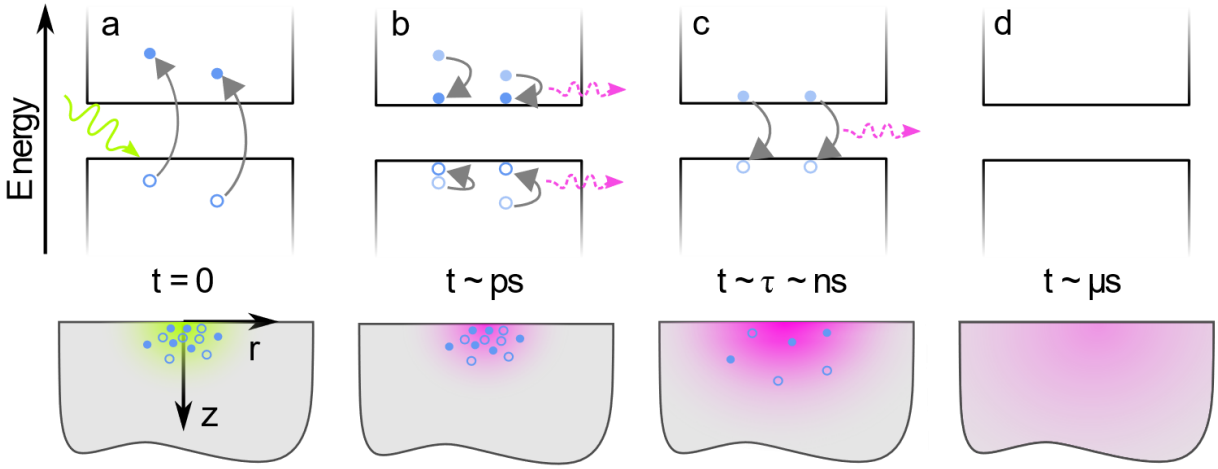

Figure 6-2: Schematic of the processes occurring after a pump pulse strikes a semiconductor sample. a) Electron-hole pairs are generated near-immediately; b) carriers thermalize rapidly, generating heat; c) heat diffuses and carriers diffuse and recombine, generating more heat; d) heat continues to diffuse after carriers have fully recombined.

Various authors have approached the problem of describing coupled thermal and carrier behavior following laser incidence. Stearns and Kino[62] and Fournier et al.[60] solve for the special case with near-surface carrier generation. Sablikov and Sandomirskii[59] solve for the carrier concentration in the sample and the surface temperature caused by a non-zero pump penetration, but do not give an expression for temperature below the surface. Tanaka et al.[73] extend the model of Sablikov and Sanomirskii to temperature as a function of depth, but do not consider heat generation from carrier recombination. All these authors assume that the laser spot is large enough to treat its lateral dimensions as infinite, which eliminates the possibility of measuring

sample anisotropy. Yang, Ziade, and Schmidt[74] and Qian et al.[69] consider spots with finite lateral dimensions and non-zero pump penetration, but model only the thermal diffusion from the initial laser incidence, neglecting carrier effects. Here, we consider the full case where the pump laser has a finite size, penetrates into the sample, and generates free charge carriers which recombine as a further heat source.

6.2.1 Carrier and temperature behavior

The behaviors of both the excited carriers and the temperature field are governed by diffusion equations. As discussed above, the temperature field depends on the carrier concentration; in principle, the carrier population is also a function of temperature. However, we assume that the temperature excursions of our samples are small enough that the population of carriers generated due to increased temperature is small compared to the photoexcited population, making this effect negligible and allowing the carrier equation to be solved separately from the temperature equation. To validate this assumption, we find an upper bound on the per-pulse heating by assuming the full energy of the pump beam is converted to heat in the volume in which it is absorbed. For the experimental parameters used in this work, we expect approximately 2 K of temperature rise for germanium and 0.2 K for silicon, corresponding to an increase in intrinsic carrier concentration of 2×10^{12} cm^{-3} and 1×10^{8} cm^{-3}, respectively.[75,76] Additionally, we assume that the photocarrier population is large enough to dominate over the background doping, so that the total electron and hole populations are similar, that is $N \approx P$. For our measurements, the pump energy per pulse was approximately 10^{-10} J, corresponding to an initial photoexcited carrier concentration of approximately 1.0×10^{19} cm^{-3} in germanium and 1.4×10^{19} cm^{-3} in silicon. Figure 6-3 highlights the degree to which the photoexcited concentration outweighs carrier concentrations from due to both temperature changes and the light doping of the samples measured.

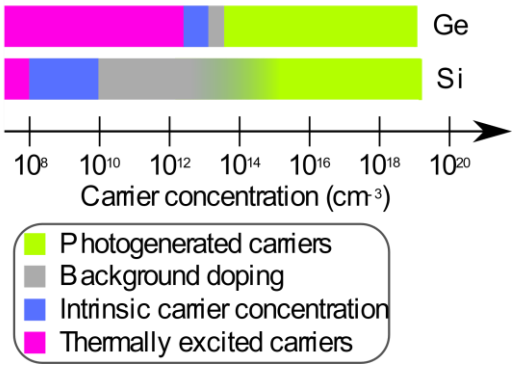

Figure 6-3: Carrier concentrations in germanium and silicon samples. With the experimental parameters used in this study, the density of photoexcited carriers far exceeds the intrinsic carrier concentration, the background doping of the sample, and the population of carriers generated due to the increase in sample temperature, validating the assumptions of our model. The background doping for the silicon sample is shown as a range because the sample was too resistive to directly measure the doping level.

A full treatment of the recombination of excited carriers would require consideration of one, two, and three phonon processes, yielding

$$\frac{\partial N_{recomb}}{\partial t} = -\gamma_1 N - \gamma_2 N^2 - \gamma_3 N^3 \qquad (6\text{-}1)$$

where γ_1, γ_2, and γ_3 are the carrier recombination rates for linear, two-body, and Auger processes, respectively.[70] Considering the full form of this equation is not mathematically feasible, but given the relatively high photoexcited carrier concentrations of our measurements, we expect Auger recombination to dominate at small delay times. Following the approach of Tanaka et al.,[70] we approximate

$$\frac{\partial N_{recomb}}{\partial t} = -\frac{N}{\tau} \tag{6-2}$$

with

$$\tau = 1 \,/\, \gamma_3 N_0^2 \tag{6-3}$$

with N_0 being the initial carrier concentration.

We begin by considering the impulse response of the sample. Each laser pulse is short enough to be modeled as a delta function in the time domain, so, considering a Gaussian pump laser spot with penetration depth $1 \,/\, \alpha$ and radius w_0, we write the intensity in the sample as

$$A_{pump} = A_0 \mathrm{e}^{\left(-2r^2/w_0^2\right)} \mathrm{e}^{-\alpha z} \delta(t) \tag{6-4}$$

where A_0 is a constant coefficient representing the incident intensity of the pump laser.

The excess carrier concentration caused by the laser, N, is described by a diffusion equation with generation due to the laser spot and loss due to recombination. Carrier motion caused by driving forces other than diffusion is assumed to be negligible. To confirm this, we estimate the current density caused by thermoelectric effects as

$$J_S = S\sigma\alpha\Delta T \tag{6-5}$$

with S the Seebeck coefficient, σ the electrical conductivity of the sample, α the absorption rate of the pump laser, and ΔT the temperature deviation caused by the laser incidence. The diffusion current density is estimated from the electrical diffusivity, D, the absorption rate of the pump laser, α, and the concentration of photoexcited carriers, ΔN, as

$$J_D = eD\alpha\Delta N \tag{6-6}$$

with e electron charge. For our germanium and silicon samples, we expect J_S to be 2×10^5 A/m^2 and 1×10^3 A/m^2,[77,78] whereas J_D will be 4×10^8 A/m^2 and 1×10^9 A/m^2, showing that diffusion dominates carrier motion.

For modeling carrier diffusion, we assume in-plane diffusivity, D_r, to be independent of direction, but allow it to be different from the out-of-plane diffusivity, D_z, yielding

$$-D_z \frac{\partial^2 N}{\partial z^2} - D_r \frac{1}{r}\frac{\partial}{\partial r}\left(r\frac{\partial N}{\partial r}\right) + \frac{\partial N}{\partial t} = \frac{-N}{\tau} + \frac{A_0}{\pi w_0^2}\delta(t)e^{-2r^2/w_0^2}e^{-\alpha z} \tag{6-7}$$

where τ is the time constant of carrier recombination.

Assuming a semi-infinite material with surface recombination velocity s at its free surface, we find boundary conditions

$$\lim_{z\to\infty} N = 0 \tag{6-8}$$

$$D_z \left.\frac{\partial N}{\partial z}\right|_{z=0} = sN|_{z=0} \tag{6-9}$$

We convert the partial differential equation to an ordinary differential equation in z by taking the Hankel transform (in r) and Fourier transform (in t), eliminating the derivatives in r and t, respectively, and replacing $\delta(t)$ with a one:

$$-D_z \frac{d^2 N}{dz^2} + D_r k^2 N + \mathrm{i}\omega N = \frac{-N}{\tau} + \frac{A_0}{4\pi}\mathrm{e}^{-k^2 w_0^2/8}\mathrm{e}^{-\alpha z} \tag{6-10}$$

This is solved by

$$N(z,\omega,k) = \frac{A_0}{4\pi D_z}\mathrm{e}^{-k^2 w_0^2/8}\frac{1}{q^2-\alpha^2}\left(\mathrm{e}^{-\alpha z} - \frac{s+D_z\alpha}{s+D_z q}\mathrm{e}^{-qz}\right) \tag{6-11}$$

with

$$q^2 = \left(D_r k^2 + \mathrm{i}\omega + 1/\tau\right) / D_z \tag{6-12}$$

Equations (6-11) and (6-12) represent the frequency response of the excess carrier concentration, in the Hankel transform domain.

The excess temperature, *T*, is described by a diffusion equation with generation due to both the laser spot and carrier recombination. We treat the thermal conductivity as constant with time, neglecting variation caused by the pump incidence. For the germanium and silicon samples studied here, the increase in thermal conductivity due to increased carrier concentration was estimated from the Wiedemann-Franz Law to be less than 0.5%.

As we did for the electrical diffusivity, we assume that in-plane thermal conductivity Λ_r is independent of direction but not necessarily identical to out-of-plane conductivity Λ_z, and write:

$$\begin{aligned} -\Lambda_z\frac{\partial^2 T}{\partial z^2} - \Lambda_r\frac{1}{r}\frac{\partial}{\partial r}\left(r\frac{\partial T}{\partial r}\right) + c_p\frac{\partial T}{\partial t} \\ = \frac{E_g}{\tau}N + \frac{A_0}{\pi\omega_0^2}\left(h\nu - E_g\right)\delta(t)\mathrm{e}^{-2r^2/w_0^2}\mathrm{e}^{-\alpha z} \end{aligned} \tag{6-13}$$

where c_p is the heat capacity of the sample, E_g is the bandgap, and $h\nu$ is the energy of a pump photon.

With the same assumptions as above, the boundary conditions are

$$\lim_{z\to\infty} T = 0 \tag{6-14}$$

$$-\Lambda_z\left.\frac{\partial T}{\partial z}\right|_{z=0} = E_g s N|_{z=0} \tag{6-15}$$

and following the same approach of taking Hankel and Fourier transforms and then solving the ODE, find

$$T(z,\omega,k) = \frac{A_0}{4\pi\,\Lambda_z}\mathrm{e}^{-k^2 w_0^2/8}\left(\mathrm{e}^{-z\alpha}C_1 + e^{-qz}C_2 + \mathrm{e}^{-q_{th}z}C_3\right) \tag{6-16}$$

where

$${q_{th}}^2 = \left(\Lambda_r\, k^2 + c_p\mathrm{i}\omega\right)/\Lambda_z \tag{6-17}$$

$$C_1 = \frac{-\left(E_g - h\nu\right)}{q_{\mathrm{th}}^2 - \alpha^2} + \frac{E_g}{D_z\tau\left(q_{\mathrm{th}}^2 - \alpha^2\right)(q^2-\alpha^2)} \tag{6-18}$$

$$C_2 = \frac{E_g}{D_z\tau\left(q^2 - q_{\mathrm{th}}^2\right)(q^2-\alpha^2)}\frac{s+D_z\alpha}{s+D_z q} \tag{6-19}$$

$$\begin{aligned} C_3 = \frac{-1}{q_{th}}\Bigg[&\frac{-\alpha\left(E_g - h\nu\right)}{q_{th}^2 - \alpha^2} \\ &+ \frac{1}{(q^2-\alpha^2)D_z\tau}\left(-E_g s\tau + \frac{s+D_z\alpha}{s+D_z q}\left(E_g s\tau + \frac{E_g q}{q^2 - q_{\mathrm{th}}^2}\right)\right. \\ &\left.+ \frac{E_g\alpha}{q_{\mathrm{th}}^2 - \alpha^2}\right)\Bigg] \end{aligned} \tag{6-20}$$

Equations (6-16) - (6-20) give the frequency response of the excess sample temperature, in the Hankel transform domain.

To highlight the types of solutions generated by equations (6-11) and (6-16), we calculate the delay time dependencies for the response to a single pump pulse and plot the resulting solutions in Figure 6-4. At zero delay time, the depth profiles of both the temperature and the carrier distributions match that of the pump spot, and as time increases carriers and heat diffuse into the sample, but at different rates. Additionally, carrier recombination both in the bulk and at the surface decreases the total carrier concentration and increases the total temperature deviation. At long enough delay times, the carrier concentration will decay to zero and the total temperature deviation will plateau.

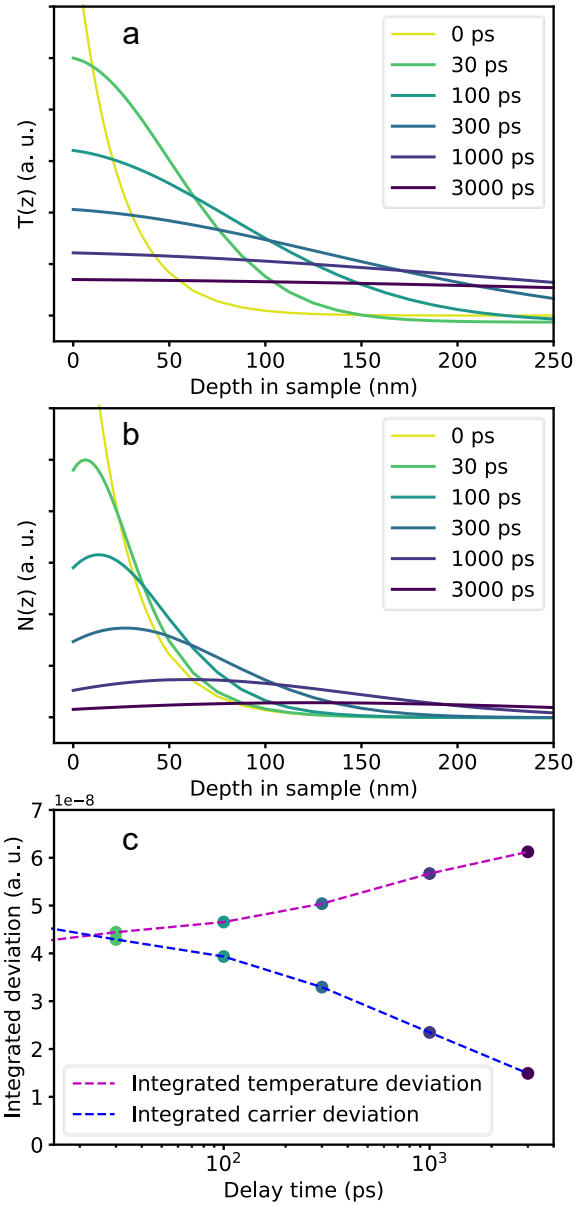

Figure 6-4: Plots of the results of a) equation (6-16) and b) equation (6-11) for a germanium sample, transformed to the time domain for a single laser pump pulse. At zero delay time, curves match the exponential behavior of the pump distribution, but diffuse into the sample as time passes. Additionally, the carrier concentration dies away and more heat is generated by recombination, as shown by c) the changing area under the curve.

6.2.2 Reflectivity

We now consider the effect of the probe beam. We assume it to be Gaussian in the transverse direction with radius w_1 and have penetration depth δ_1 into the sample, allowing its intensity to be described by

$$A_{probe} = A_1 \mathrm{e}^{(-2r^2/w_1^2)} \mathrm{e}^{-z/\delta_1} \tag{6-21}$$

where A_1 is a constant coefficient representing the incident intensity of the probe laser.

The total reflectivity is a function of the complex refractive index, $\tilde{n} = n + i\kappa$, in the entire volume addressed by the probe. We first consider the z dimension.

To properly address the reflectivity of the sample to the penetrating probe beam, it is necessary to solve Maxwell's equations in the material. We seek to consider the effects of both carrier concentration and temperature, so we begin by assessing the response to an arbitrary parameter affecting $\tilde{n}$, which we denote $\phi(z, \omega)$. For such a parameter, we expect a change in reflection [79]

$$\Delta R(\omega) = \int_0^\infty f(z)\phi(z,\omega)\,\mathrm{d}z \tag{6-22}$$

where $f(z)$ is a sensitivity function consisting of an exponentially damped oscillation caused by the interference of reflections from the surface and within the sampled depth:[79]

$$f(z) = f_0 \left(\frac{\partial n}{\partial \phi} sin\left(\frac{4\pi n z}{\lambda} - \theta \right) + \frac{\partial \kappa}{\partial \phi} cos\left(\frac{4\pi n z}{\lambda} - \theta \right) \right) \mathrm{e}^{-z/\delta_1} \tag{6-23}$$

$$f_0 = 8 \frac{2\pi(n^2(n^2+\kappa^2-1)^2 + \kappa^2(n^2+\kappa^2+1)^2)^{1/2}}{\lambda((n+1)^2+\kappa^2)^2} \tag{6-24}$$

$$tan\,\theta = \frac{\kappa(n^2+\kappa^2+1)}{n(n^2+\kappa^2-1)} \tag{6-25}$$

where λ is the probe wavelength and $\theta \in \left[0, \frac{\pi}{2}\right]$. For the semiconductors under study here, $\frac{\partial \kappa}{\partial \phi} \ll \frac{\partial n}{\partial \phi}$, so, to a good approximation,

$$f(z) = f_0 \left(\frac{\partial n}{\partial \phi} \sin\left(\frac{4\pi n z}{\lambda} - \theta \right) \right) \mathrm{e}^{-z/\delta_1} \tag{6-26}$$

which is plotted in Figure 6-5.

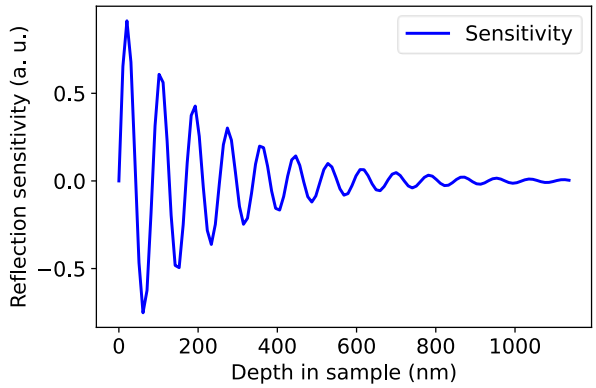

Figure 6-5: The result of equation (6-26), sensitivity of the reflectivity of the sample to deviations in carrier concentration and temperature, as a function of depth. θ is taken to be zero, corresponding to the case of negligible κ and $\frac{\partial \kappa}{\partial \phi}$, and all other parameters are those of germanium probed at 800 nm.

We now consider how to define $\phi(z,\omega)$. In semiconductors, the refractive index is affected by both the carrier and thermal distributions,[70]

$$\Delta n = \frac{\partial n}{\partial T}\Delta T + \frac{\partial n}{\partial N}\Delta N \tag{6-27}$$

so instead of the single parameter ϕ we must consider both *N* and *T*, yielding

$$\begin{aligned}\Delta R(\omega,k) = \int_0^\infty f_0 \sin\left(\frac{4\pi n z}{\lambda} - \theta\right)\left(\frac{\partial n}{\partial N}\Delta N(\omega,z,k)\right. \\ \left. + \frac{\partial n}{\partial T}\Delta T(\omega,z,k)\right)\mathrm{e}^{-z/\delta_1}\,\mathrm{d}z\end{aligned} \tag{6-28}$$

This adds two additional unknown parameters to the system: $\frac{\partial n}{\partial N}$ and $\frac{\partial n}{\partial T}$. The first, $\frac{\partial n}{\partial N}$, can be estimated from the semiconductor Drude equation,[80]

$$\frac{\mathrm{d}n}{\mathrm{d}N} = \frac{-\lambda^2 \mathrm{e}^2}{2\pi n m^* c^2} \tag{6-29}$$

where λ is the probe wavelength, *e* the charge of an electron, m^* the ambipolar effective mass of the charge carriers, and *c* the speed of light.

The second term, $\frac{\partial n}{\partial T}$ is a result of several effects, including Fermi smearing, electron-phonon collisions, and bandgap shift, and is best estimated from empirical data.[70] However, due to the number of difficult-to-estimate initial coefficients of our equation, we fit a normalized version of the signal such that only the ratio $\frac{\partial n}{\partial N} / \frac{\partial n}{\partial T}$ is relevant to the final result, and can be determined in the data fitting process. In most semiconductors, $\frac{\partial n}{\partial T}$ is positive, unlike $\frac{\partial n}{\partial N}$, so $\frac{\partial n}{\partial N} / \frac{\partial n}{\partial T}$ is expected to be negative.[70]

We now consider the lateral extent of the probe. The probe measures a weighted average of the area it strikes.[7] Taking the Hankel transform of equation (6-21) and combining with the Hankel domain solution $\Delta R(\omega,k)$, we find

$$\Delta R_{probe}(\omega) = \int_0^\infty \Delta R(\omega,k)\mathrm{e}^{-k^2 w_1^2/8} k\,\mathrm{d}k \tag{6-30}$$

Combined with equations (6-11) - (6-12), (6-16) - (6-20), and (6-28), equation (6-30) gives an expression for the frequency dependence of the measured reflectivity.

6.2.3 Voltage signal

As described above, the measured tTDR signal is given by the reflection of a modulated pulsed laser. The reflection is directed to a photodetector, which provides a voltage signal which is sent to a lock-in amplifier set to the modulation frequency, *f*. This means that the signal samples the frequency response of the sample at ±*f* as well as at frequencies shifted by multiples of the frequency of the laser repetition rate, $1/\tau_{rep}$:[7]

$$\begin{aligned}\Delta V(t_{delay}) = \frac{\mathrm{d}V}{\mathrm{d}R}\sum_{m=-\infty}^{\infty}\left(\Delta R\left(\frac{m}{\tau_{rep}} + f\right)\right. \\ \left. + \Delta R\left(\frac{m}{\tau_{rep}} - f\right)\right) exp\left(2\pi i m t_{delay} / \tau_{rep}\right)\end{aligned} \tag{6-31}$$

where ΔV is the measured voltage signal, and $\frac{dV}{dR}$ is the responsivity of the the photodetector-amplifier system. By combining equations (6-30) and (6-31) we find the predicted tTDR signal. An example of the depth profiles of T and N and their combination into the final signal is shown in Figure 6-6.

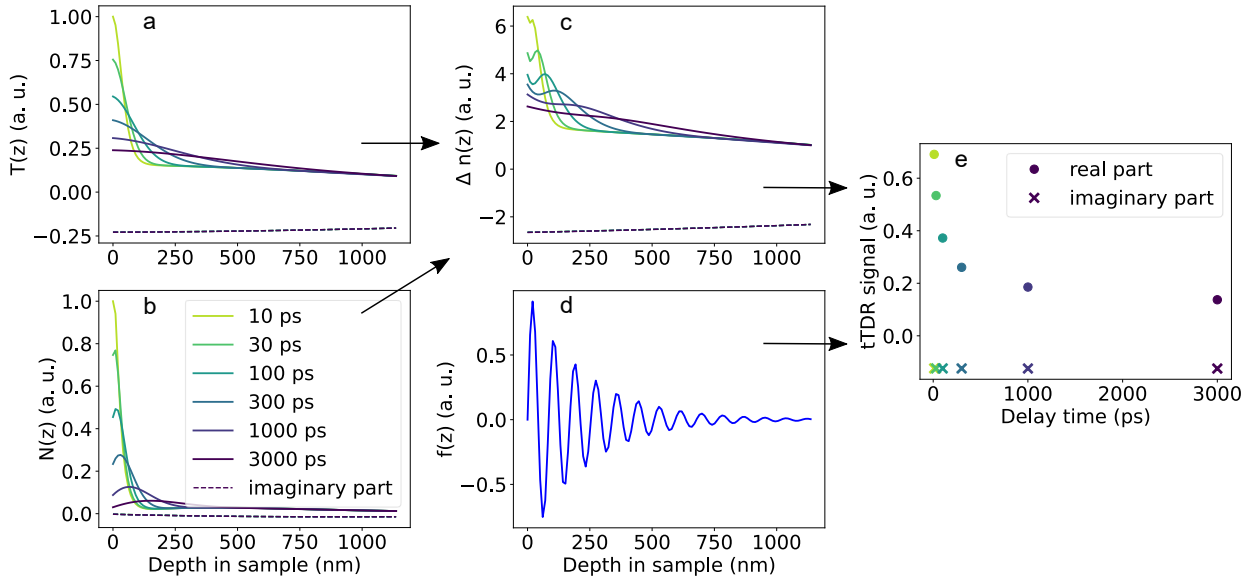

Figure 6-6: Schematic of temperature profile and carrier concentration effects on the recorded tTDR signal, based on a germanium sample measured with a modulation frequency of 1 MHz. Both a) the temperature and b) the carrier concentration affect c) the refractive index, and multiplying the refractive index deviation by d) the sensitivity and integrating gives e) the measured signal. The real part of the signal is influenced by both the single-pulse response and the modulation-frequency response, and the imaginary part primarily by the modulation-frequency response.

Table I: Parameters affecting $\Delta V(t_{delay})$ after normalization

Symbol	Property	Function of
Λ_z, Λ_r	Thermal conductivities	Sample
c_p	Heat capacity	Sample
D_z, D_r	Electrical diffusivities	Sample
s	Surface recombination velocity	Sample
E_g	Bandgap	Sample
τ	Carrier lifetime	Sample and measurement
α	Pump absorption rate	Sample and measurement wavelength
δ_1	Probe absorption depth	Sample and measurement wavelength
n	Index of refraction at probe wavelength	Sample and measurement wavelength
$\frac{\partial n}{\partial N}/\frac{\partial n}{\partial T}$	Ratio of carrier signal to temperature signal	Sample and measurement wavelength
w_0, w_1	Pump and probe spot radii	Measurement
ω	Modulation frequency	Measurement
$h\nu$	Pump photon energy	Measurement
λ	Probe wavelength	Measurement

6.3 Results

We validate our time-domain approach to tTDR measurements by confirming our ability to measure known samples. Here we focus on germanium and silicon, both indirect-bandgap semiconductors with bandgaps below the energy of our 565 nm pump and 800 nm probe beams. We assume that carrier recombination happens primarily through non-radiative mechanisms, validating our assumption that each recombination event releases thermal energy E_g. We measure [100] wafers of both materials.

As is typical for TDTR, we perform measurements at a range of modulation frequencies and fit our results for each frequency independently. Optical penetration depths and refractive indexes were determined by ellipsometry, and comparison to literature values shows good agreement. Electronic diffusivity was determined through Hall effect measurements for germanium and as a fitting parameter for silicon. In both cases, diffusivities were found to be lower in our samples than in the literature, more notably for germanium, which we attribute to lower purity of our samples than those studied elsewhere. The range of diffusivity considered for germanium spans the standard deviation of the values found through repeated Hall measurement, and for silicon the range covers the values found from fitting at different modulation frequencies. Data fitting for silicon is described in more detail below. Literature values are used for heat capacities[81] with an assumed 10% uncertainty, and spot sizes are measured by analysis of photos of the laser spot. For the germanium sample, a lower magnification objective was used than for silicon, leading to a larger spot size, and the spot size was determined from a photo of the reflected laser, leading to uncertainty from setting the camera focus; for the silicon, the camera was placed in the sample location, minimizing this uncertainty. Multiple images were taken of each laser spot and the range of spot sizes found was used in calculating error bars on thermal conductivity.

Assessment of these parameters leaves the carrier recombination time, the surface recombination velocity, the ratio $\frac{\partial n}{\partial N} / \frac{\partial n}{\partial T}$, and the thermal conductivity to be determined. Though

we are unable to fit to all of these parameters simultaneously, only a narrow range of values was found that gave consistent results at all modulation frequencies, and these were used in the final fitting to thermal conductivity. We analyze the total magnitude of our tTDR signal, normalized to that just before the pump arrival.

Table II: Values of parameters used for fits. Ranges listed were used in the calculation of error bars and are the smaller of the assumed uncertainty of the measurement in which the value was found or the maximum range in which it was possible to find a good fit to the experimental data. See text for further description of ranges used and commentary on comparison to literature values.

Parameter	Value for Ge	Range for Ge	Literature values for Ge	Value for Si	Range for Si	Literature values for Si
c_p (J/m^3K)[81]	1.70×10^6	1.53×10^6 to 1.87×10^6	1.70×10^6	1.66×10^6	1.49×10^6 to 1.83×10^6	1.66×10^6
D (m^2/s)	5.3×10^{-6}	5.25×10^{-6} to 5.35×10^{-6}	7.7×10^{-3} [82]	7.3×10^{-4}	6.6×10^{-4} to 7.9×10^{-4}	3.5×10^{-3} [83]
s (m/s)	80	72 to 104	0.8[84]	125	124 to 133	87 to 500[85]
τ (s)	1×10^{-5}	5×10^{-7} to 1×10^{-2}	7×10^{-7} [86]	9×10^{-8}	8.6×10^{-8} to 9.6×10^{-8}	3×10^{-9} [87]
α (1/m)	4.4×10^7	-	4.5×10^7 [88]	7.1×10^5	-	7.1×10^5 [88]
δ_1 (m)	2.3×10^{-7}	-	2.0×10^{-7} [88]	9.7×10^{-6}	-	9.7×10^{-6} [88]
n	4.72	-	4.71 [88]	3.69	-	3.69 [88]
$\frac{\partial n}{\partial N}/\frac{\partial n}{\partial T}$ (m^3K)	-5.72×10^{-26}	-6.18×10^{-26} to -5.26×10^{-26}	-6×10^{-25} [89,90]	-7.54×10^{-24}	-12.3×10^{-24} to -8.69×10^{-24}	-9×10^{-25} [90,91]
Effective spot size (m)	2.1×10^{-5}	1.68×10^{-5} to 2.52×10^{-5}	-	7.6×10^{-6}	7.37×10^{-6} to 7.83×10^{-6}	-

6.3.1 Germanium

Best-fit values for germanium properties were found through an iterative fitting procedure, starting with expected literature values. The carrier recombination time and surface recombination velocity were perturbed in turn until high quality fits with consistent values across modulation frequency were found. The signal at small delay time is more sensitive to the ratio $\frac{\partial n}{\partial N}/\frac{\partial n}{\partial T}$ than that at longer delay time, so fits to the first nanosecond of data were used to determine $\frac{\partial n}{\partial N}/\frac{\partial n}{\partial T}$, and fits to the full dataset were used to determine the thermal conductivity.

The significantly larger best-fit surface recombination velocity compared to the literature value for germanium is not surprising, as surface recombination is very sensitive to surface quality and our sample received no special surface treatment. The carrier recombination time estimated from the literature assumes a carrier concentration equal to that immediately following

the pump incidence; the lower carrier concentration at longer delay times would lead to a longer recombination time, explaining the difference to our measured value. We repeated our measurements at laser powers lower than those reported here and did not see a significant difference in normalized signal, despite the expected dependence of carrier recombination time on pulse energy, due to the weak dependence of the final signal on the recombination time. The calculated literature value of $\frac{\partial n}{\partial N}/\frac{\partial n}{\partial T}$ relies on both estimation of $\frac{\partial n}{\partial T}$ based on data measured at longer wavelengths and on the validity of the Drude model for $\frac{\partial n}{\partial N}$, meaning that the difference from it to the best-fit value is not significant.

Once best-fit values for all parameters (as listed in Table II) were determined, uncertainties were assessed. Because of the numerical complexity of the model, our ability to consider the simultaneous effects of multiple parameters, for example through the Monte Carlo method, was limited, and error bars were estimated based on the effects of each parameter individually. The uncertainties for the carrier recombination time and the surface recombination velocity were found by changing the value of each parameter individually until the model failed to find a good fit to the data, defined as a doubling of the residuals of the fit or a difference of more than 40% in values found for different modulation frequencies. The range of $\frac{\partial n}{\partial N}/\frac{\partial n}{\partial T}$ considered was that given by the fits for different modulation frequencies. The effect of the uncertainty in each input parameter was determined by repeating the fitting to thermal conductivity with that parameter modified to the limits of its uncertainty, and recording the resultant change in fitted value, $\Delta\Lambda_i$ for parameter i. The magnitudes of the error bars are found as

$$\Delta\Lambda_{tot} = \sqrt{\sum_i (\Delta\Lambda_i)^2} \tag{6-32}$$

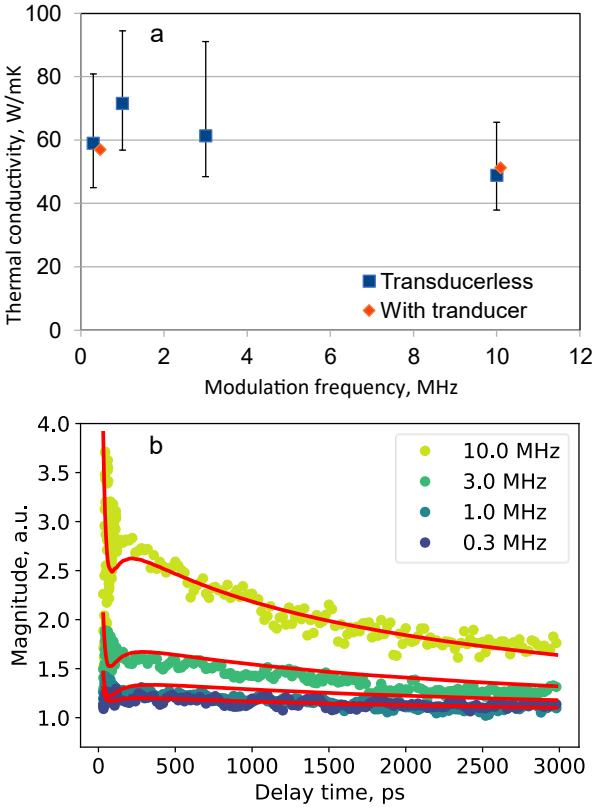

Figure 6-7: Fitting results for germanium. a) Fitted values of thermal conductivity. Error bars are found by perturbing input parameters within their uncertainties. b) Overall fit of model to total magnitude of recorded tTDR data for each modulation frequency. The large signal at small delay times is caused by the dominance of the carrier response at those times.

Fitting results for the germanium sample are shown in Figure 6-7. Our average fitted thermal conductivity of 60 W/mK matches the value found by Maycock,[92] and aligns well with the result we measured by standard TDTR of 51-57 W/mK. Over the tens of picoseconds to nanoseconds of delay time typical of a TDTR measurement, the model is a good fit.

As discussed above, the measured tTDR signal is a combination of thermal and carrier effects. In Figure 6-8 we examine the relative components of the thermal and electrical signal for germanium. The measured signal is explained primarily by the thermal behavior at long delay times, but at short delay times the carrier behavior is also relevant.

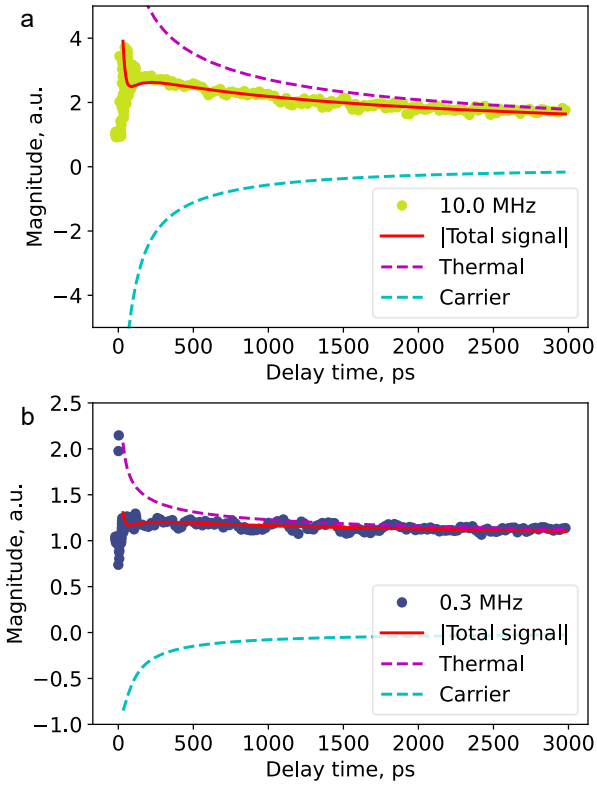

Figure 6-8: Calculated thermal and carrier contributions to the magnitude of total tTDR signal recorded for the Ge sample at a) 10 and b) 0.3 MHz. The total signal is the absolute value of the sum of the (positive) thermal contribution and the (negative) carrier contribution. The carrier effect is more significant at higher modulation frequency, but the thermal signal is larger except at very small delay times.

6.3.2 Silicon

Fits for the silicon sample, shown in in Figure 6-9, were found through a similar procedure to those for the germanium sample. However, in contrast to the case for germanium, for silicon the signal is dominated by the carrier response (Figure 6-10), due to the much higher value of $\frac{\partial n}{\partial N}/\frac{\partial n}{\partial T}$ for the silicon sample. We attribute this to silicon having a weaker dependence of refractive index on temperature than germanium for measurements at 800 nm. Because of the dominance of the carrier response, we were only able to find fitting values for the thermal conductivity for the measurements at the lowest modulation frequencies, where the sensitivity to the thermal properties is strongest. We used the data collected at higher modulation frequency to determine the electrical diffusivity, carrier recombination rate, and surface recombination velocity by a similar iterative procedure to that used for the germanium fitting, and then fit $\frac{\partial n}{\partial N}/\frac{\partial n}{\partial T}$ and the thermal conductivity based on the low frequency data. Error bar calculations for the silicon sample were performed as for the germanium sample.

The best-fit value of the surface recombination velocity was within the range expected from the literature. As in germanium, the fitted carrier recombination rate was lower than expected from Auger recombination based on the initial carrier concentration, which we attribute to the lower carrier concentration at longer delay times. We did not observe a significant dependence of our signal on laser pulse energy, but this does not rule out a dependence of carrier recombination

time on pulse energy as the final signal is not very sensitive to recombination time, especially when that time is larger, as occurs at lower pulse energies. Our estimate of $\frac{\partial n}{\partial N}/\frac{\partial n}{\partial T}$ for silicon is similar to that for germanium, whereas our observed values are quite different, which highlights the limitations of our method for estimating $\frac{\partial n}{\partial N}/\frac{\partial n}{\partial T}$.

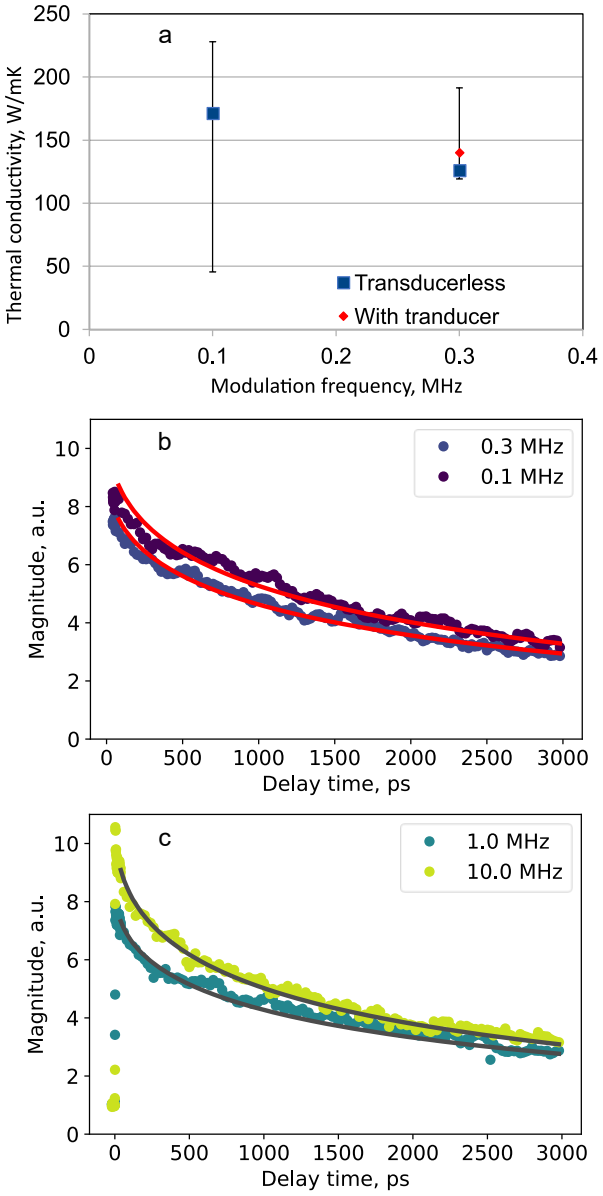

Figure 6-9: Fitting results for silicon. a) Fitted values of thermal conductivity. Error bars are found by perturbing input parameters within their uncertainties. We attribute the larger error bars at 0.1 MHz to the larger instrument noise at low frequency. b) Overall fit of model to total magnitude of tTDR data for low modulation frequencies, where thermal conductivity was the fitting parameter. c) Overall fit of model to total magnitude of tTDR data for higher modulation frequencies, where carrier properties were fit.

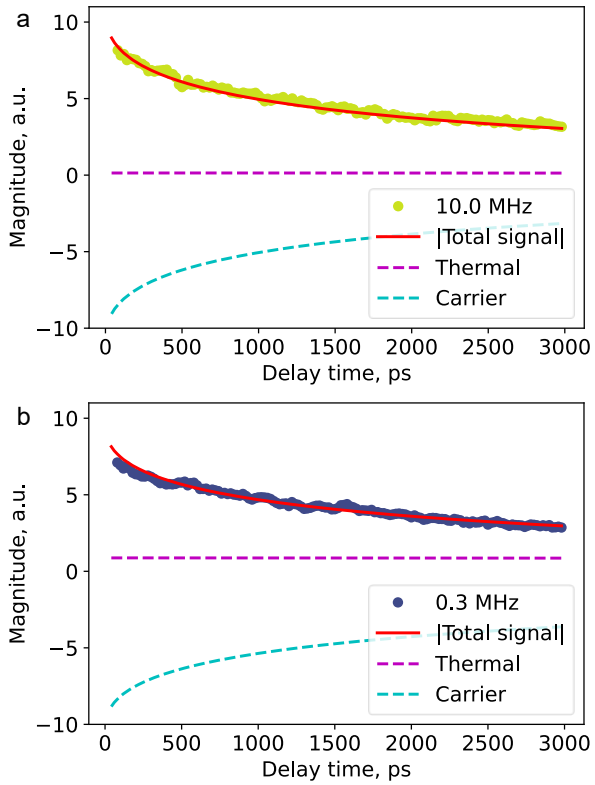

Figure 6-10: Calculated thermal and carrier contributions to the total tTDR signal recorded for the Ge sample at a) 10 and b) 0.3 MHz. The total signal is the absolute value of the sum of the (positive) thermal contribution and the (negative) carrier contribution. The carrier effect dominates in both cases, but the thermal effect is non-negligible at low modulation frequency.

Despite the larger uncertainty caused by the lower sensitivity to thermal conductivity and higher noise in our system at low frequency, our average fitted result for the thermal conductivity of silicon of 148 W/mK compares well to the literature value of 149 W/mK[67] and to our result from standard TDTR of 140 W/mK. We highlight that our consideration of photoexcited carriers allows our model to describe the behavior of this sample, unlike the model presented by Qian et al, which fails to fit their experimental data for silicon.[69] We anticipate that laser wavelengths other than those used here may allow measurement with lower uncertainty: a shorter pump wavelength would provide more thermal energy per incident photon, without increasing the initial carrier density, and a different probe wavelength might provide a higher $\frac{\partial n}{\partial T}$ and so more sensitivity to thermal changes.

6.3.3 Sensitivity analysis

To better understand the properties of our model, we perform a quantitative sensitivity analysis. Defining the sensitivity to a parameter x as $S_x = \frac{\partial \ln R}{\partial \ln x}$ and comparing the relative sensitivities of various parameters, we can establish how strongly each parameter influences our result. Results for Ge and Si at high and low modulation frequency are shown in Figure 6-11.

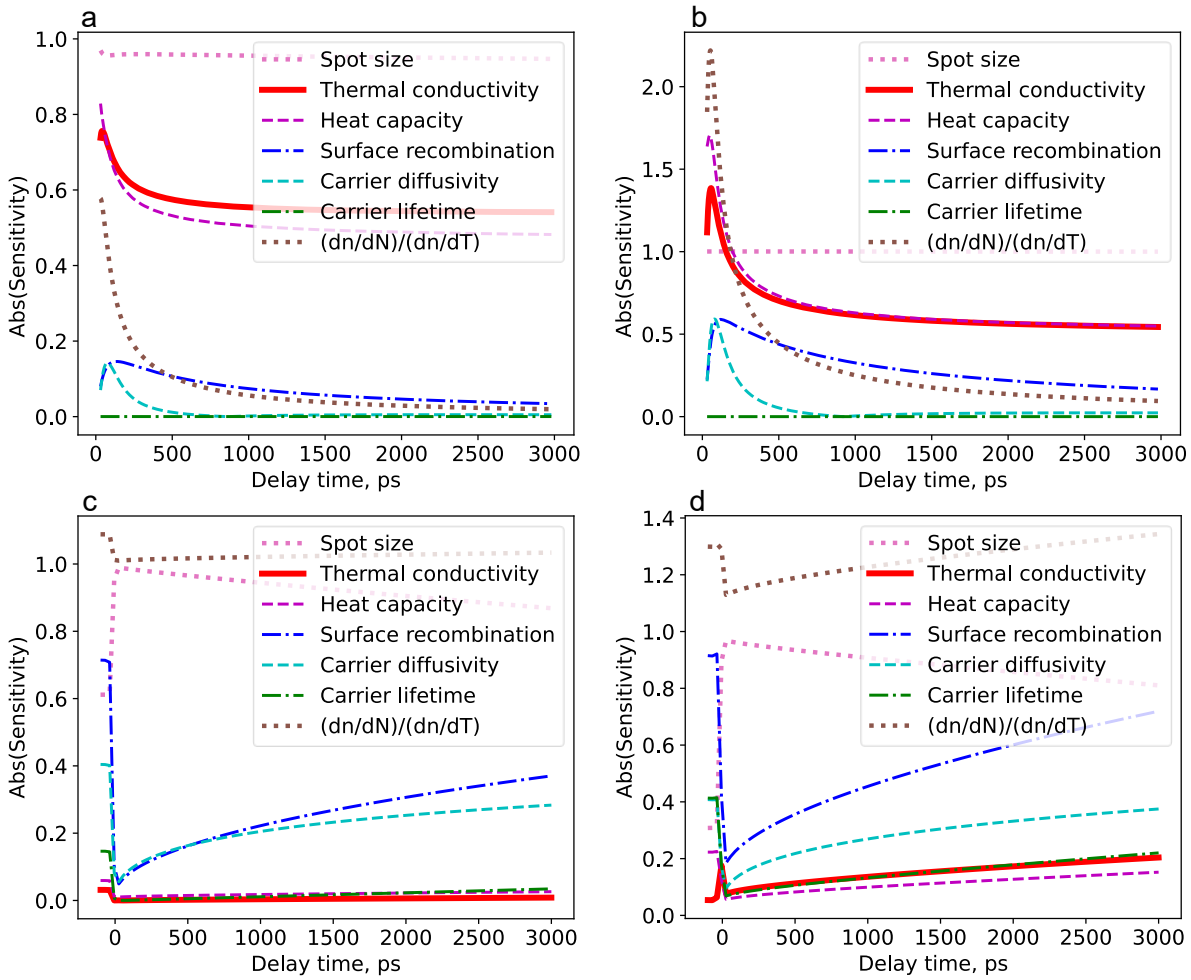

Figure 6-11: Sensitivity plots for a) Ge at 10 MHz modulation frequency, b) Ge at 0.3 MHz, c) Si at 10 MHz, and d) Si at 0.1 MHz.

For the germanium sample, the sensitivity to thermal conductivity is higher than that to other parameters except for the spot size and heat capacity. At low delay times and high frequencies, $\frac{\partial n}{\partial N} / \frac{\partial n}{\partial T}$ has a significant impact on the signal, but this sensitivity is decreased at larger delay times. Sensitivity to carrier lifetime is negligible, implying that surface recombination occurs significantly faster than bulk recombination in this sample. Though the sensitivity to spot size is larger than that to thermal conductivity, the fact that it is nearly constant with delay time and we fit to normalized data means that uncertainty in spot size has minimal effect on the fitting result. As long as the heat capacity of the sample is well known, fitting to the thermal conductivity will be reliable.

By contrast, the sensitivity to thermal conductivity in the silicon sample is very small—indeed, negligible at high frequency. As shown in Figure 6-10 and indicated by the high sensitivity to $\frac{\partial n}{\partial N} / \frac{\partial n}{\partial T}$, the sample response is determined primarily by the carrier response, not the thermal one. To have any confidence in a value measured for the thermal conductivity, we took advantage of the minimal sensitivity to thermal properties at high frequency and fit to the carrier diffusivity, carrier recombination rate, and surface recombination velocity, increasing our confidence in our input for fits at low frequencies. Thus, even though the fits at 0.1 MHz and 0.3 MHz are still dominated by the carrier properties, we have sufficient confidence in the values of those properties to determine a thermal conductivity.

6.4 Conclusions

The dominant noncontact methods of measuring thermal conductivity, TDTR and FDTR, generally require the use of a metal film transducer. However, the use of a transducer complicates the measurement and can restrict access to or reduce sensitivity to certain material properties of interest. In this paper, we demonstrate that time domain transient reflectivity measurements of the thermal properties of semiconductors can be made without the use of a transducer. We present a model for both the carrier and thermal responses to heating with, and measurement by, laser spots of finite dimension and non-zero penetration depth. We show that the model accurately describes the signal from direct measurements of germanium and silicon samples. Though we do not explore fully the possibility in this work, we anticipate that this result will be easily extended to the measurement of samples which cannot easily be measured with a transducer, for example, ultra-thin films or suspended membranes.

7 Transducerless measurements of two-dimensional materials

7.1 Motivation

Measurement of in-plane properties of ultra-thin materials, such as suspended two-dimensional (2D) materials, is very challenging. Measurements are limited by the practicalities of sample fabrication, which require working with small areas of fragile membranes. Additionally, the small thermal conductance of ultrathin membranes means that the presence of any additional material for heat application or temperature sensing is likely to provide a thermal short, necessitating non-contact measurements. Though traditional TDTR is generally considered a non-contact method, it does require the presence of a metal transducer. Deposition of such a layer would be likely to damage a suspended 2D sample and, more importantly, the typical tens of nanometers of metal thickness would conduct far more heat than the material under study, making measurements insensitive to sample properties. Most existing work has instead used Raman thermography.

Raman thermography measures thermal conductivity by using a laser to heat the sample directly, and either the same or a second laser to record the Raman spectrum of the heated sample. Shifts in Raman peaks with temperature are used to detect temperature variation. In the case of one-laser Raman measurements (the same laser acts as heater and thermometer), the relationship between input laser power and measured temperature is recorded and compared to a thermal model. Knowing the heat input into the system requires precise knowledge of the optical absorption of the sample under study, and assumptions must be made about the degree to which thermal resistance comes from intrinsic properties compared to interfaces, etc. This problem is somewhat overcome by two-laser Raman thermography, which uses separate pump and probe lasers to heat the sample and measure the temperature, respectively.[93] This allows the probe laser to be swept in position with respect to the pump laser, allowing mapping of the temperature profile and the use of more detailed modeling. However, both techniques are limited to materials with Raman active modes with appropriately temperature-sensitive properties. Additionally, the non-modulated nature of the measurement means that the pump laser power must significantly exceed that of the probe laser to avoid artifacts from probe heating. Coupled with the fact that Raman peaks do not shift strongly with temperature (for example, Reparez et al[93] relied on a peak shift of 0.022 cm^{-1}/K to monitor temperature in silicon membranes), this requires pump powers large enough to heat the sample by typically 10s and sometimes 100s of Kelvin.

Transducerless time domain reflectance measurements provide another avenue for measurement of in-plane properties of ultra-thin samples. They avoid the problems caused by the introduction of a transducer layer and do not require capturing or fitting to Raman spectra. By using a modulated pump beam, the effects of probe heating do not directly appear in the measurement—so long as the steady-state heating of the sample is low enough not to alter the result, the probe power is irrelevant. Though some information about the electronic properties of the sample is required, they offer an additional tool for characterization of 2D materials and can be done with existing TDTR setups.

7.2 Physics

Much of the physics underlying tTDR measurements of two-dimensional (2D) materials is similar to that underlying measurements of bulk materials, so the model of 2D materials was built from that for bulk materials. Key differences are highlighted here.

In a suspended 2D material, there is no relevant depth dimension. For the materials under study, much of both the pump and the probe intensity was transmitted through the material, so the laser intensity was taken to be constant through the material, and heat and charge transport were taken to be entirely in the lateral direction. This makes properties such as the out-of-plane electrical diffusivity and thermal conductivity irrelevant. Additionally, the material is thin enough that the self-interference of the probe beam described for bulk materials does not occur, and the probe beam can be taken to measure the temperature throughout the depth of the material. (Because the material is thin and the pump also heats throughout its depth, there is no z-dependence of temperature, so the average temperature is the same as the temperature at any depth.) Additionally, surface recombination becomes indistinguishable from bulk recombination as the surfaces and the bulk become close together. For 2D materials, only the total recombination rate was considered, and it should be understood to include recombination from multiple sources, including surface effects.

Many 2D materials, including the MoS_2 studied here, have energetically favorable exciton states even at room temperature. As such, the lowest energy states that carriers relax to following laser excitation are likely to be excitons rather than free electrons and holes at the band edge as in bulk Si and Ge. This has minimal implications for modeling the system, as exciton diffusion and recombination are, from the perspective of the resulting heat, not very different from free carrier diffusion and recombination. The main difference is that the exciton binding energy reduces the energy released during recombination, so instead of the bandgap, the expected energy released by the lowest-energy exciton (in MoS_2, the A exciton)[94] was used in the thermal model.

Complicating matters is the fact that the suspended area of the sample is not much larger than the other length scales in the problem (e.g. spot size, thermal penetration depth), so treating the sample as a semi-infinite suspended membrane led to modeling results that failed to match the measured data for any physically plausible parameter values, as shown in Figures 7-1 and 7-2. However, the small thickness of 2D materials leads to two convenient effects: 1) the in-plane thermal conductance in the membrane is relatively small compared to the conductance between the supported area and the substrate; and 2) the heat capacity of the membrane is small compared to that of the volume of substrate thermally near its supported regions. Together, these effects mean that treating the substrate as maintaining a constant temperature and enforcing a constant temperature boundary condition at the edge of the suspended region is a reasonable approximation. To confirm this, the thermal resistance from the edge of the laser spot, taken to be the $1/e^2$ radius, to the edge of the suspended region was compared to that from the edge of the suspended region to the bulk silicon. (Figure 7-3) Even for a ring as narrow as 100 nm

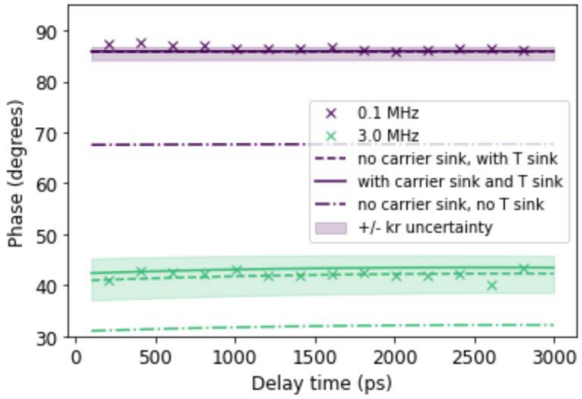

Figure 7-1: Comparison of fit assumptions at 0.1 and 3 MHz. Shown are calculations assuming an infinitely large thermally insulated region (dash-dot line), a finite thermally insulated region and infinite electrically insulated region (dashed line), and finite thermally insulated and electrically insulated regions (solid line), as well as experimental data (symbols). Changing the boundary conditions for carriers led to only small changes in the fit; changing them for temperature led to very different results, especially at low frequency.

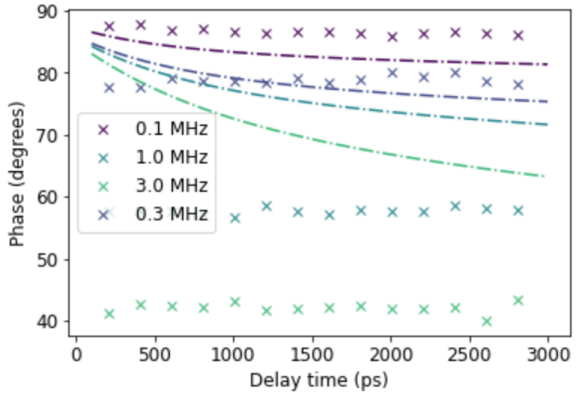

Figure 7-2: attempting to fit low frequency data without accounting for heat sinking required very high thermal conductivity values (here, 500 W/mK) and led to poor fitting of higher frequency data

transmitting heat to the bulk, the thermal resistance from the edge to the bulk (steps 2 and 3 in Figure 7-3, treated as in series to provide a worst-case estimate) was an order of magnitude less than that within the suspended region (step 1 in Figure 7-3), indicating that once heat entered the supported region of the sample it was quickly transported to the bulk silicon—that is, the silicon was an effective heat sink.

The finite spacial domain of the suspended region slightly modifies the mathematical analysis used in Chapter 6. The Hankel transform approach for solving the diffusion equations must be replaced with a Bessel series approach, where the variable k takes on discrete values in order to meet the constant temperature boundary condition at $r = r_{suspended}$, which is met when $J_0(k_n\, r_{suspended}) = 0$ for J_0 the Bessel function of order 0. For example, the heat diffusion equation in the radial direction,

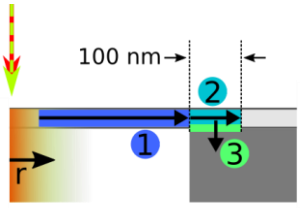

Figure 7-3: Steps used in the assessment of the heat sinking of the sample edges: thermal resistance from the laser spot to the edge of the suspended region (1) was found to be an order of magnitude less than thermal conductance from the edge of the suspended region to 100 nm from the edge, plus the thermal resistance across the interface into the silicon substrate, so the edges of the suspended region were treated as being at a constant temperature.

$$-\Lambda_r \frac{1}{r}\frac{\partial}{\partial r}\left(r\frac{\partial N}{\partial r}\right) + c_p\frac{\partial T}{\partial t} = \frac{E_{exciton}}{\tau}N + \frac{A}{\pi w_0^2}(h\nu - E_{exciton})\delta(t)e^{-2r^2/w_0^2} \tag{7-1}$$

becomes

$$\Lambda_r k_n^2 T + i\omega c_p T = \frac{E_{exciton}}{\tau}N(k_n) + \frac{A}{\pi w_0^2}(h\nu - E_{exciton})\int_0^{r_{suspended}} e^{-2r^2/w_0^2} J_0(k_n\, r)\, r\, dr \tag{7-2}$$

for k_n such that $J_0\left(k_n\, r_{suspended}\right) = 0$

Note that equation (7-2) depends on the behavior of N at the corresponding value of k_n. However, the above discussion focused on the boundary conditions for the heat diffusion equation, not the carrier diffusion equation. In the simplest mathematical case, the same type of boundary condition would apply for both—here, a fixed carrier concentration condition to match the fixed temperature condition. Though the silicon acts as an effective heat sink, it may be less effective as a carrier sink, especially given the presence of the native oxide layer. To account for this, two approaches were taken and compared. First, the spacial domain for the carrier diffusion equation was taken to be infinite, corresponding to an MoS_2 flake much larger than the dimensions of the measurement and well-insulated (electrically) from the silicon, and the carrier diffusion equation solved using a Hankel transform. This solution was converted back to real space, as shown in Figure 7-4, where it could be seen that most of the excess carrier population existed in the suspended region of the sample. In order to solve the heat diffusion equation, the Bessel series of this real space solution was calculated, providing $N(k_n)$ as required. This result was compared to that found by requiring $N\left(r \geq r_{suspended}\right) = 0$, which allowed treatment of the carrier diffusion equation similar to that shown above for the temperature equation and provided $N(k_n)$ directly. As shown in Figure 7-1, these two results were nearly identical at low modulation frequency and deviated slightly at higher frequency, but well within the experimental uncertainty bounds. Because of the reduced computational intensity of the second approach, it was used for finding the final fitted results.

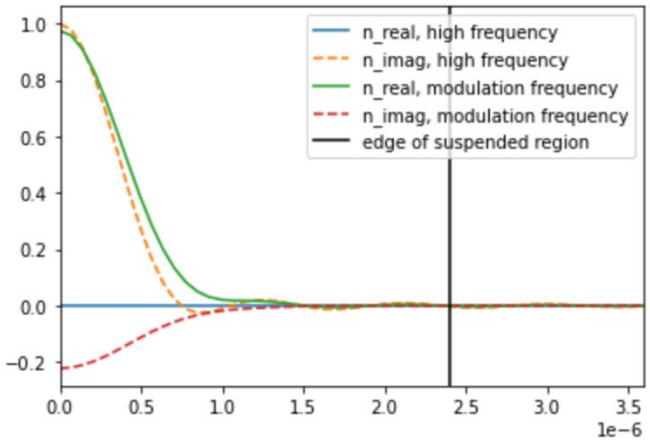

Figure 7-4: Distribution of in- and out-of-phase (real and imaginary) parts of the function describing carrier population, for the high and low frequency components of the measurement, when an infinite spacial domain is assumed. Regardless of frequency, most of the carrier density is found to be within the suspended region.

7.3 Measurement of suspended MoS_2

MoS_2 monolayers were exfoliated from a mineral sample by tape exfoliation onto PDMS. Monolayers were visually identified by light microscopy, and then dry transferred onto a pre-prepared silicon substrate with 4.8 micron diameter holes, which had been cleaned with acetone, isopropanol, and DI water and dried under dry nitrogen. The yield from this process was quite low, as monolayers tended to tear at the edges of the holes, but one sample was successfully prepared and studied via tTDR. To avoid overheating of the sample, low laser powers were used, with long averaging times per data point in order to reduce noise. The tTDR signal is proportional to the product of the absorbed pump power and the thermoreflected probe power, both proportional to the intensity of the beams. The steady state heating of the sample is proportional to the sum of the absorbed pump power and the absorbed probe power. It is desirable, then, to maximize the product of the powers while minimizing the sum. This would be done by using matching pump and probe powers except that the probe interacts with the sample much more weakly than the pump, so a probe power of 120 μW was used with a pump power of 30 μW. It is expected that this led to steady state heating of a few 10s of Kelvin along with a smaller temperature deviation at the modulation frequency. A 100x 0.95 NA objective was used to focus the laser spots onto the sample. The spots were aligned with the suspended membrane first by eye using the system camera, and then the position of the sample was adjusted to maximize the total signal at negative delay time and low modulation frequency, where it arises primarily from heating. Since the center of the membrane was more insulated from the substrate than the edges, it should provide the maximum signal. Measurements were then taken and are shown in Figure 7-5.

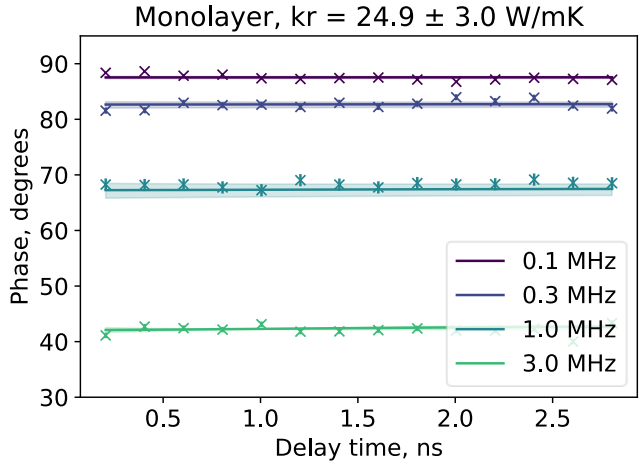

Figure 7-5: Measured data and fitted model for monolayer MoS_2. Error bars on the symbols represent the uncertainty in the calculated phase correction, and shaded regions the effect of perturbing the thermal conductivity within its uncertainty.

Fitting to the raw data was done as described in section 4.3. Laser spot sizes were found by analyzing images of the spots captured by the system camera. Heat capacity was taken from the literature to be 2.0 J/m^3K.[95] Diffusivity and carrier lifetime were taken from literature values as 0.06 cm^2/s and 18 ns, respectively,[96] though in this fitting they were allowed to vary within a factor of two of those values, and fit as 0.058±0.016 cm^2/s and 18.5±1.6 ns. The ratio of the strength of the measured carrier effect to the thermal effect was also treated as a fitting parameter and was found to be $-9.1 \times 10^{-26} \pm 2.7 \times 10^{-27}$ m^{-3}/K^{-1}.

The fitted value of 25 W/m K is lower than previous literature reports of 35-84 W/mK[97–100] from Raman thermography and transient grating spectroscopy. However, given the large scatter in existing work, this value is not unreasonable. Further work, such as the study of additional samples or a temperature-dependent measurement, would strengthen this result.

7.4 Moiré structures

When two or more lattices are stacked and are not matched, whether in lattice constant or in angle, a moiré structures is formed. This provides a superlattice with longer-range periodicity and can lead to the development of new properties. Because of the large moiré lattice constant, a many-atom unit cell is created, corresponding to a very small Brillouin zone. This leads to the formation of new electronic, exitonic, and phononic states.[101,102] Moiré structures in 2D materials have seen significant interest since the demonstration of a magic angle in twisted bilayer graphene, where the flattening of the electronic bands leads to exotic behavior including superconductivity.[103] Most of the investigations of the properties of moiré structures have focused on electronic and optical properties, with little focus on thermal properties. Those works which have studied thermal properties have largely explored out-of-plane conductivity, which has been shown to be dramatically suppressed by twist,[4] but systematic study of in-plane properties is lacking, despite the clear introduction of in-plane periodicity. In this work, steps were taken toward characterization of the in-plane thermal properties of MoS_2 homobilayers.

Phonon thermal conductivity is determined by the frequency and velocity of the phonon modes, i.e. $\Lambda = \frac{1}{3}\int \tau\, v^2 C_\omega\, d\omega$ for τ the relaxation time of the phonon mode, v its velocity, and C_ω the specific heat per unit frequency. Note that τ, v, and C_ω are generally all functions of ω.[26]

Many of the phonon properties are expected to be affected by twist. The reduction in size of the Brillouin zone leads to band folding, leading to the presence of many optical phonon bands. Because of the low group velocity of optical phonons, they carry little heat, so the presence of many optical phonon bands typically leads to reduction in thermal conductivity. Additionally, the presence of many bands increases the number of available channels for phonon-phonon scattering. Smaller twist angles lead to larger moiré lattices and so more band folding, so may lead to lower thermal conductivity than large twist angles.

Additionally, some of the phonon modes of MoS_2 are directly affected by the twist angle. For example, low-frequency Raman measurements have shown that the shear and layer-breathing modes which exist in an untwisted bilayer are not present for twists above about 3°, though a different layer-breathing mode appears in twisted samples.[104] Even lower energy shear modes, with dispersion relationships comparable to those of the intrinsic acoustic phonon modes, have been computationally predicted.[105] The dispersions of these modes, including their velocities, are functions of twist angle, with lower velocity at smaller twist angle.[105] Such low-energy modes may well contribute to heat transport and would also be expected to have lower thermal conductivity at lower twist angle.

Molecular dynamics has been applied to predicting the in-plane conductivity of graphene and MoS_2.[106,107] In both cases, suppression of thermal conductivity with twist is expected, but in graphene a critical angle with minimal thermal conductivity is predicted, and such a result is not seen in MoS_2. (Figure 7-6 a-b) In graphene, MD simulation suggests this is related to increased wrinkling at the critical twist angle,[106] but it is not clear why MoS_2 would not be subject to similar behavior.

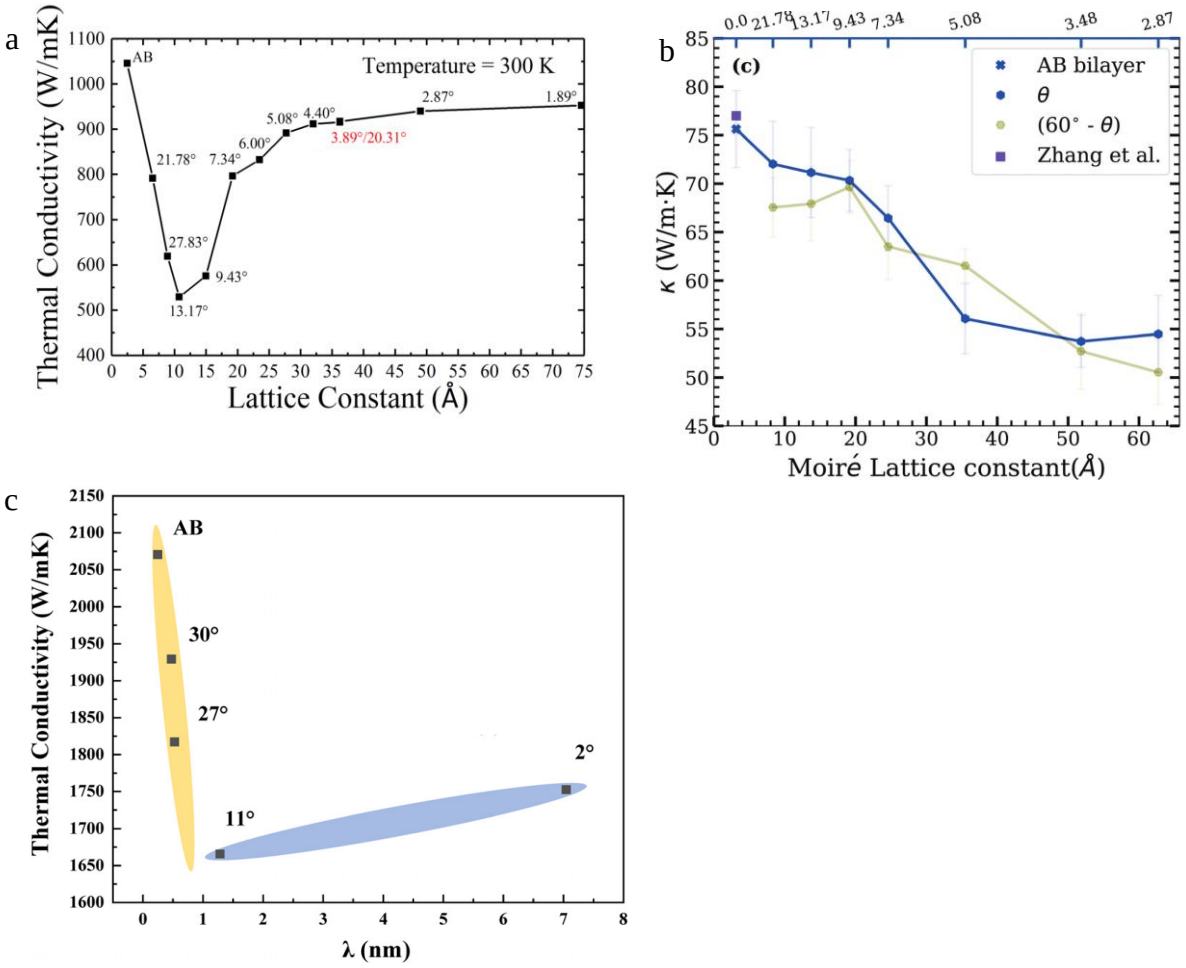

Figure 7-6: a) MD calculated thermal conductivity of twisted bilayer graphene vs commensurate lattice constant, showing a minimum near 13 degrees of twist. Figure taken from Li and Lake.[106] b) MD calculated thermal conductivity for twisted bilayer MoS2 vs moiré lattice constant, showing a monotonic decrease. Figure taken from Mandal et al.[107] c) Raman thermography measurement of thermal conductivity of twisted bilayer graphene vs moiré lattice constant, showing a minimum near 11 degrees of twist. Figure taken from Han et al.[108]

Two studies have reported experimental values for the in-plane thermal conductivity of twisted bilayer graphene, both using Raman thermography. Li et al.[109] measured a single twisted sample (34° twist) across a range of temperatures. At room temperature, they saw a roughly 25% suppression in thermal conductivity compared to an untwisted bilayer. Han et al.[108] measured five samples at twist angles of 0°, 2°, 11°, 27°, and 30° and saw a minimum thermal conductivity in the 11° sample, with an approximately 20% reduction compared to the 0° sample. (Figure 7-6c) This minimum angle corresponds well to the MD prediction of a minimum near 13°, though the predicted thermal conductivities varied between the MD calculation and the measurement. Similar studies of MoS_2 are lacking.

7.4.1 tTDR for moiré structures

Moire structures were assembled by exfoliation and stamping. Tape exfoliation from a bulk crystal was used to generate monolayers on a PDMS stamp, which were identified by optical

microscopy. These were then stamped over a hole in the substrate, with the desired twist applied between the first and second transfer. This was an extremely low-yield process, particularly due to tearing of the monolayers at the edges of the holes. This severely limited the number of available samples for tTDR measurement.

Visually promising samples included those at 5, 10, and 30 degree twists as well as a native bilayer. Unfortunately, high-quality data was only recorded from the sample with a 10 degree twist, but all are briefly discussed here. Fitting properties other than thermal conductivity were taken to be the same as those of the monolayer. Some uncertainty in the carrier diffusivity and lifetime and in $(\frac{dn}{dN})/(\frac{dn}{dT})$ were accounted for by allowing them to be fit parameters, but terms in the emcee objective function were added to drive them toward Gaussian distributions matching those from the monolayer fit. (See Section 4.3 for discussion of the objective function.)

7.4.1.1 Native bilayer

The native bilayer sample was one of the first suspended samples measured, before calculations of the heating of the suspended area were done. As such, it was subjected to higher laser power than other samples and was damaged. Some data was collected before the damage was obvious, (Figure 7-7) but the high laser fluence led to qualitatively different results—e.g. the carrier effect appeared to affect the reflectivity similarly to the thermal effect, rather than opposite it as in all other measured semiconductor samples. This could be mathematically modeled, and the effect could originate due to shifts in exciton absorption peaks caused by intense light, but certainly this behavior indicates results that are hard to compare to other measured data. Additionally, the steady state laser heating was significant enough that it is hard to determine what the effective sample temperature was during the measurement. As such, these results are not very meaningful.

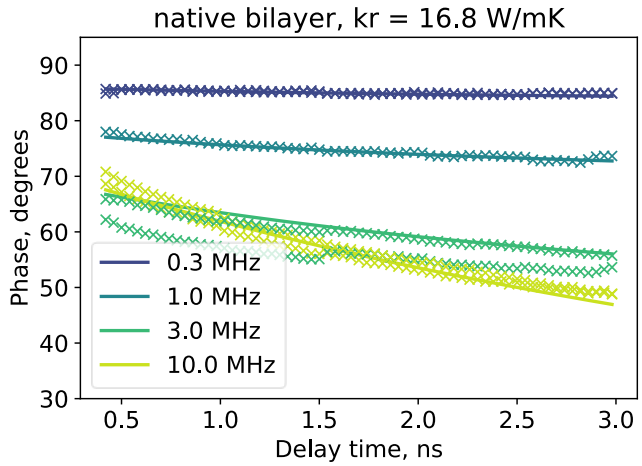

Figure 7-7: Measured data and fitted model for native bilayer MoS_2. These data were collected at much higher laser power, leading to qualitatively different results than found in lower-power measurements.

7.4.1.2 5 degree twist

The sample prepared with a 5° twist was measured at a similar laser power to that used for the monolayer. It provided sufficient signal at modulation frequencies of 1 MHz and below; signal was very weak at higher frequency. However, the measured data, shown in Figure 7-8, consistently had significantly lower phases than the other samples at all measured modulation frequencies. This would most easily be explained by a very low thermal conductivity (<1 W/mK). It is possible that this indicates a partially damaged sample, in which case assuming that the electronic properties are the same as in the other samples is also unreasonable. Regardless, without additional samples to validate the response, it seems likely that this result is due to problems in the fabrication rather than due to the moiré structure.

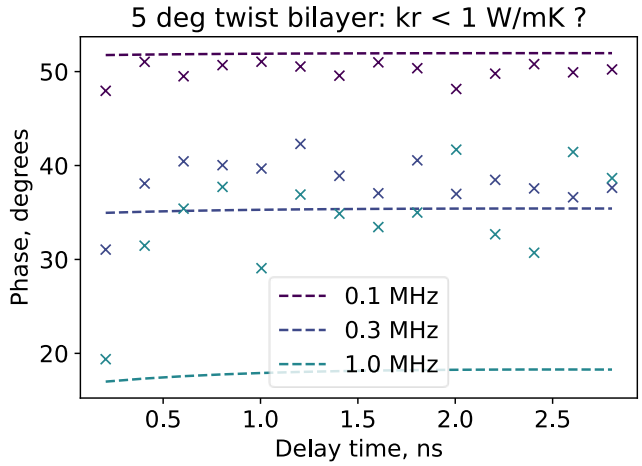

Figure 7-8: Measured data and fitted model for bilayer MoS_2 with a 5° twist. The much lower measured phase than in other measurements could only be fit by assuming extremely low thermal conductivity, and even then the fit was not very good.

7.4.1.3 10 degree twist

Raw data for the 10° sample was qualitatively similar to that for the monolayer sample, showing little trend with decay time but a stronger trend with modulation frequency. Signal at 10 MHz modulation was too weak to be meaningful, but that for 3 MHz and below was usable and is shown in Figure 7-9. The fitted thermal conductivity of 27.5 W/mK was slightly higher than the 24.9 W/mK measured for the monolayer. Reported thermal conductivities of untwisted bilayer MoS_2 are generally larger than those of the monolayer, an effect attributed to decreased boundary scattering in the thicker samples,[100,110] though some reports show the opposite trend.[97]

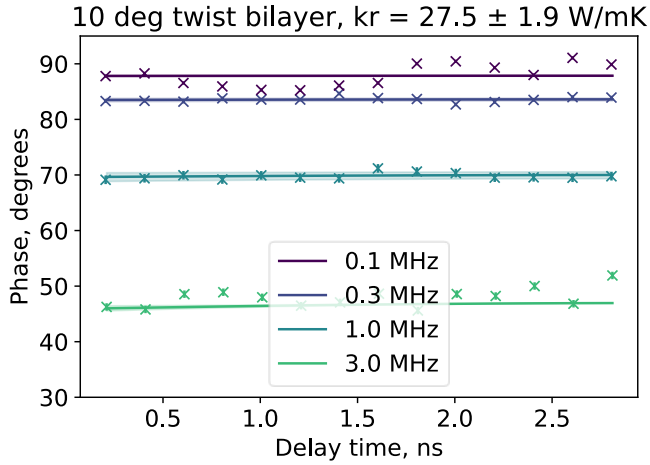

Figure 7-9: Measured data and fitted model for bilayer MoS_2 with 10° twist. Error bars on the symbols represent the uncertainty in the calculated phase correction, and shaded regions the effect of perturbing the thermal conductivity within its uncertainty.

Seeing a slight increase from the monolayer to a twisted bilayer is believable but does not provide any direct information on the effect of the twist.

7.4.1.4 30 degree

Measurements from the 30° sample yielded weaker signal than those from the 10° sample. Possibly the optimum focus and laser position for measurements were not found—small adjustments to sample positioning were seen to make a large difference in signal intensity. Regardless, an attempt was made to fit the measured data, as shown in Figure 7-10, and the model captured some of the behavior of the data. However, the fitted result of 4.7 W/mK was dramatically different from the other measured values, and without more certainty in the data this seems an unlikely result.

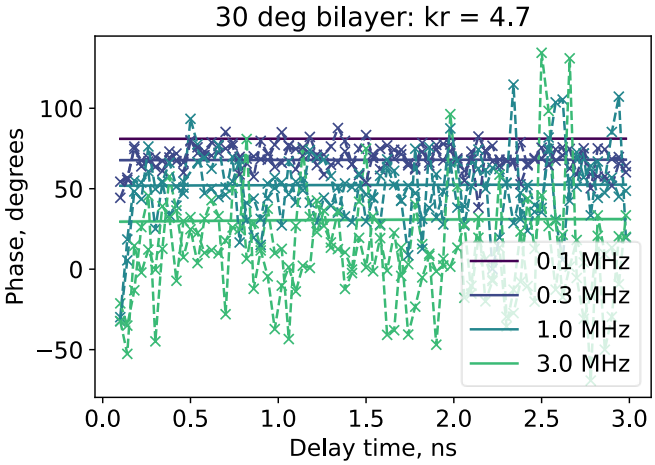

Figure 7-10: Measured data and fitted model for bilayer MoS_2 with 30° twist. As is evident, data were much noisier for this sample than for the monolayer and 10° samples, so this fit result does not seem reliable.

7.4.2 Moiré structures: Conclusion

Attempts were made to measure several twisted bilayer structures, and the measurements of the sample with 10° twist worked well. This demonstrates the possibility of using tTDR to study moiré structures but is insufficient data to make comments on their effects. Future work should also include measurements of the temperature dependence of the thermal conductivity of both untwisted and twisted samples to better elucidate the phonon behaviors. Additional characterization through other techniques suitable for measuring the lowest energy phonon branches, such as Brillouin-Mandelstam spectroscopy[111] has been suggested for similar systems.[105] Comparison between such measurements of low-energy phonon branches and thermal conductivity measurements would provide valuable insight into the underlying mechanisms governing the dependence of thermal conductivity on twist angle.

7.5 Conclusion

The tTDR method provides a new tool for measuring the thermal conductivity of ultrathin materials such as monolayer and bilayer MoS_2. The model for a bulk material can be readily adapted to the 2D case and is shown to fit measured data. Though further validation would be beneficial, this is a promising result. Additionally, twisted bilayer structures were measured, though sample fabrication limitations prevented systematic study as a function of twist angle.

8 Summary and outlook

This work strives to further the applicability of TDR techniques, both through better understanding of what can be measured and through new technique development. The key contribution of this work is the development of tranducerless time domain reflectivity measurements. These are a novel tool for measuring semiconductor thermal properties and make existing TDTR equipment usable for systems which for which it would otherwise not be useful, such as measuring suspended two dimensional semiconductor samples. The demonstration that the technique can be used for such samples, including moiré structures, motivates further attempts to leverage it to better understand such materials systems.

There are certainly many open questions. Chapter 4 describes the use of more sophisticated fitting methods for TDR data, but more rigorous mathematical frameworks to guide such efforts would be a significant contribution.

Chapters 5 describes attempts to study materials near their metal-insulator transitions, but clear results about Lorentz number suppression were not available because the samples studied showed relatively small changes in electrical conductivity, so negligible changes in thermal conductivity were expected. Study of samples with higher electrical conductivity in the metallic state would allow a clearer assessment of Lorentz number suppression and allow investigation of factors such as grain size and orientation on the degree of suppression measured. Additionally, a systematic study of the effects of doping with tungsten or other materials known to affect the metal-insulator transition, such as titanium, could provide additional information about the origins of such suppression. Direct measurement of lattice properties across the transition, for example by inelastic x-ray scattering, would allow more rigorous decoupling of the electronic and lattice contributions to the total thermal conductivity and allow for more accurate determination of the Lorentz number.

Chapters 6 and 7 discuss the development and application of tTDR, but most of its potential applications have not been explored. It is a powerful tool for measurement of any semiconductor sample with electronic properties that can be separately measured, for example through Hall effect measurements, or fit simultaneously with thermal properties as was done for MoS_2. It is particularly applicable to ultra-thin samples or others where coating with a metal transducer layer is infeasible. Though this work has discussed measurements as a function of delay time, the same analysis applies to measurements as a function of modulation frequency, whether with pulsed or continuous-wave lasers. Transducerless frequency domain reflectivity measurements would be a straightforward extension of this work.

As discussed in Chapter 7, moiré structures are a rich field, and their in-plane thermal properties are poorly understood. This work made only small inroads towards changing that. With higher-yield sample preparation, measurements as a function of twist angle for MoS_2 and other 2D semiconductors could be performed, and the effect of the moiré lattice structure assessed. The analysis presented for tTDR on suspended 2D materials assumed a circular suspended region with effective heat sinking at the edges, but otherwise the details of the substrate have minimal effect, and other measurements could be performed on the same or adjacent regions to that used for tTDR. Very similar sample geometries are used for Raman thermography, allowing the possibility of direct comparison between the techniques. Additionally, appropriate substrates could be suitable for both tTDR and transmission electron microscopy, allowing direct measurement of twist angle and observation of the structure of measured samples. Other optical measurements, for example of photoluminescence lifetime,

could provide an estimate of the exciton lifetime in the samples. Such coupled measurements by different techniques could provide exciting insight into the relationships between multiple properties of samples under study.

The field of thermal measurements is a rich one, and the thermal properties of electronic materials will remain technologically relevant. This work offers improvements to the existing techniques and paves the way for more advances.

9 Bibliography

1. Lee, S. *et al.* Anomalously low electronic thermal conductivity in metallic vanadium dioxide. *Science (80-.).* **355**, 371–374 (2017).
2. Oh, D. W., Ko, C., Ramanathan, S. & Cahill, D. G. Thermal conductivity and dynamic heat capacity across the metal-insulator transition in thin film VO2. *Appl. Phys. Lett.* **96**, (2010).
3. Balandin, A. A. *et al.* Superior thermal conductivity of single-layer graphene. *Nano Lett.* **8**, 902–907 (2008).
4. Kim, S. E. *et al.* Extremely anisotropic van der Waals thermal conductors. *Nature* **597**, 660–665 (2021).
5. Paddock, C. A. & Eesley, G. L. Transient thermoreflectance from thin metal films. *J. Appl. Phys.* **60**, 285–290 (1986).
6. Capinski, W. S. & Maris, H. J. Improved apparatus for picosecond pump-and-probe optical measurements. *Rev. Sci. Instrum.* **67**, 2720–2726 (1996).
7. Cahill, D. G. Analysis of heat flow in layered structures for time-domain thermoreflectance. *Rev. Sci. Instrum.* **75**, 5119–5122 (2004).
8. Schmidt, A. J., Cheaito, R. & Chiesa, M. A frequency-domain thermoreflectance method for the characterization of thermal properties. *Rev. Sci. Instrum.* **80**, 3–8 (2009).
9. Schmidt, A. J., Chen, X. & Chen, G. Pulse accumulation, radial heat conduction, and anisotropic thermal conductivity in pump-probe transient thermoreflectance. *Rev. Sci. Instrum.* **79**, (2008).
10. Schmidt, A. J. Optical Characterization of Thermal Transport from the Nanoscale to the Macroscale. (2008).
11. Oppenheim, A., Willsky, A. & Hamid, S. *Signals and Systems*. (Pearson, 1996).
12. Thermal Conductivity in W cm-1 K-1 of Metals and Seminconductors as a Function of Temperature (100 K to 2000 K). in *CRC Handbook of Chemistry and Physics* (ed. Rumble, J.) (CRC Press/Taylor & Francis).
13. Powell, R. W., Ho, C. Y. & Liley, P. E. *Thermal conductivity of selected materials*. (U.S. Department of Commerce, National Bureau of Standards, 1966).
14. Brorson, S. D., Fujimoto, J. G. & Ippen, E. P. Femtosecond electronic heat-transport dynamics in thin gold films. *Phys. Rev. Lett.* **59**, 1962–1965 (1987).
15. Hohlfeld, J. *et al.* Electron and lattice dynamics following optical excitation of metals. *Chem. Phys.* **251**, 237–258 (2000).
16. Schoenlein, R. W., Lin, W. Z., Fujimoto, J. G. & Eesley, G. L. Femtosecond studies of nonequilibrium electronic processes in metals. *Phys. Rev. Lett.* **58**, 1680–1683 (1987).
17. Fann, W. S., Storz, R., Tom, H. W. K. & Bokor, J. Electron thermalization in gold. *Phys. Rev. B* **46**, 13592–13595 (1992).
18. Hostetler, J. L., Smith, A. N., Czajkowsky, D. M. & Norris, P. M. Measurement of the electron-phonon coupling factor dependence on film thickness and grain size in Au, Cr, and Al. *Appl. Opt.* **38**, 3614 (1999).
19. Elsayed-Ali, H. E., Norris, T. B., Pessot, M. A. & Mourou, G. A. Time-resolved observation of electron-phonon relaxation in copper. *Phys. Rev. Lett.* **58**, 1212–1215 (1987).
20. Lubner, S. D. Thermal conductivity measurements in challenging regimes. (2016).
21. Rosei, R. & Lynch, D. W. Thermomodulation Spectra of Al, Au, and Cu. *Phys. Rev. B* **5**,

3883–3893 (1972).
22. Burzo, M. G., Komarov, P. L. & Raad, P. E. Minimizing the uncertainties associated with the measurement of thermal properties by the transient thermo-reflectance method. *IEEE Trans. Components Packag. Technol.* **28**, 39–44 (2005).
23. Ehrenreich, H., Philipp, H. R. & Segall, B. Optical properties of aluminum. *Phys. Rev.* **132**, 1918–1928 (1963).
24. Fourier, J. B. J. *The Analytical Theory of Heat*. (The University Press, 1878).
25. Hahn, D. & Ozisik, M. N. *Heat Conduction*. (Wiley, 2012).
26. Chen, G. *Nanoscale Energy Transport and Conversion*. (Oxford University Press, 2005). doi:10.2221/jcsj.50.53.
27. Kittel, C. *Introduction to Solid State Physics*. (Wiley, 1996).
28. Koh, Y. K. & Cahill, D. G. Frequency dependence of the thermal conductivity of semiconductor alloys. *Phys. Rev. B - Condens. Matter Mater. Phys.* **76**, 1–5 (2007).
29. Swartz, E. T. & Pohl, R. O. Thermal boundary resistance. *Rev. Mod. Phys.* **61**, 605–668 (1989).
30. Swartz, E. T. & Pohl, R. O. Thermal resistance at interfaces. *Appl. Phys. Lett.* **51**, (1987).
31. Monachon, C., Weber, L. & Dames, C. Thermal Boundary Conductance: A Materials Science Perspective. *Annu. Rev. Mater. Res.* **46**, 433–463 (2016).
32. Feldman, A. Algorithm for solutions of the thermal diffusion equation in a stratified medium with a modulated heating source. *High Temp. - High Press.* **31**, 293–298 (1999).
33. Schmidt, A. J., Cheaito, R. & Chiesa, M. A frequency-domain thermoreflectance method for the characterization of thermal properties. *Rev. Sci. Instrum.* **80**, (2009).
34. Carslaw, H. S. & Jaeger, J. C. *Conduction of Heat in Solids*. (Oxford University Press, 1959).
35. Virtanen, P. *et al.* SciPy 1.0: fundamental algorithms for scientific computing in Python. *Nat. Methods* **17**, 261–272 (2020).
36. scipy.optimize.curve_fit. https://docs.scipy.org/doc/scipy/reference/generated/scipy.optimize.curve_fit.html (2022).
37. Marquardt, D. W. An algorithm for least-squares estimation of nonlinear parameters. *J. Soc. Insust. Appl. Math.* **11**, (1963).
38. Levenberg, K. A method for the solution of certain non-linear problems in least squares. *Q. Appl. Math.* **2**, 164–168 (1944).
39. Lehmann, E. L. & Casella, G. *Theory of Point Estimation (Springer Texts in Statistics)*. (Springer, 1998).
40. Cramér, H. *Methods of Mathematical Statistics*. (Princeton University Press, 1946).
41. Rao, C. R. Information and the Accuracy Attainable in the Estimation of Statistical Parameters. in *Breakthroughs in Statistics. Springer Series in Statistics* (eds. Kotz, S. & Johnson, N. L.) (Springer, 1992). doi:https://doi.org/10.1007/978-1-4612-0919-5_16.
42. Asprey, S. P. & Macchietto, S. Designing robust optimal dynamic experiments. *J. Process Control* **12**, 545–556 (2002).
43. Jauffret, C. Observability and Fisher information matrix in nonlinear regression. *IEEE Trans. Aerosp. Electron. Syst.* **43**, 756–759 (2007).
44. Foreman-Mackey, D., Hogg, D. W., Lang, D. & Goodman, J. emcee: The MCMC Hammer. *arXiv* (2013) doi:10.1086/670067.
45. MacKay, D. J. C. *Information Theory, Inference, and Learning Algorithms*. (Cambridge University Press, 2005).

46. Goodman, J. & Weare, J. Ensemble Samplers with Affine Invariance. *Commun. Appl. Math. Comput. Sci.* **5**, (2010).
47. Hogg, D. W., Bovy, J. & Lang, D. Data analysis recipes: Fitting a model to data. *arXiv* (2010).
48. Dobrosavljević, V. Introduction to Metal-Insulator Transitions. in *Conductor Insulator Quantum Phase Transitions* (eds. Dobrosavljevic, V., Trivedi, N. & Valles, J. M. J.) (Oxford University Press, 2012). doi:10.1093/acprof:oso/9780199592593.003.0001.
49. Gebhard, F. *The Mott Metal-Insulator Transition: Models and Methods*. *Springer Tracts in Modern Physics: Volume 137* (Springer, 1962).
50. Hiroi, Z. Structural instability of the rutile compounds and its relevance to the metal-insulator transition of VO2. *Prog. Solid State Chem.* **43**, 47–69 (2015).
51. Andreev, V. N., Chudnovskii, F. A., Petrov, A. V & Terukov, E. I. Thermal Conductivity of VO2, V3O5, and V2O3. *phys stat sol a* **48**, K153–K156 (1978).
52. Berglund, C. N. & Guggenheim, H. J. Electronic Properties of VO2 near the Semiconductor-Metal Transition. *Phys. Rev.* **185**, 1022–1033 (1969).
53. Kizuka, H. *et al.* Temperature dependence of thermal conductivity of VO2thin films across metal-insulator transition. *Jpn. J. Appl. Phys.* **54**, 1–5 (2015).
54. Eyert, V. The metal-insulator transitions of VO2: A band theoretical approach. *Ann. der Phys.* **11**, 650–702 (2002).
55. Chandrashekhar, G. V., Barros, H. L. C. & Honig, J. M. Heat capacity of VO2single crystals. *Mater. Res. Bull.* **8**, 369–374 (1973).
56. Buyco, E. H. & Davis, F. E. Specific Heat of Aluminum from Zero to Its Melting Temperature and Beyond Equation for Representation of the Specific Heat of Solids. *J. Chem. Eng. Data* **15**, 518–523 (1970).
57. Fournier, D., Marangolo, M. & Fretigny, C. Measurement of thermal properties of bulk materials and thin films by modulated thermoreflectance (MTR) Measurement of thermal properties of bulk materials and thin films by modulated thermoreflectance (MTR). *J Appl Phys* **128**, 241101 (2020).
58. Dramicanain, M. D., Ristovski, Z. D., Nikolic, P. M., Vasiljevic, D. G. & Todorovic, M. Photoacoustic investigation of transport in semiconductors: Theoretical and experimental study of a Ge single crystal. *Phys. Rev. B* **51**, 226–233 (1995).
59. Sablikov, V. A. & Sandomirskii, V. B. The Photoacoustic Effect in Semiconductors. *phys stat sol b* **120**, 471–480 (1983).
60. Fournier, D., Boccara, C., Skumanich, A. & Amer, N. M. Photothermal investigation of transport in semiconductors: Theory and experiment. *J. Appl. Phys.* **59**, 787–795 (1986).
61. Fournier, D. & Boccara, A. C. Thermal wave probing of the optical electronic and thermal properties of semiconductors. *Mater. Sci. Eng. B* **5**, 83–88 (1990).
62. Stearns & Kino. Photoacoustic techniques for the measurement of electronic properties of semiconductors. in *Thermal Wave Phenomena in Semiconductors* (ed. Mandelis, A.) (North Holland Publishing Company, 1987).
63. Wagner, R. E. & Mandelis, A. Photomodulated Optical-Reflectance Studies of Germanium: Diagnostic Separation of Temperature and Free-Carrier Effects. in *Photoacoustic and Photothermal Phenomena III: Proceedings of the 7th International Topical Meeting on PA and PT Phenomena* (ed. Bicanic, D.) 372–374 (Springer-Verlag, 1992).
64. Hurley, D. H., Wright, O. B., Matsuda, O. & Shinde, S. L. Time resolved imaging of

carrier and thermal transport in silicon. *J. Appl. Phys.* **107**, (2010).
65. Vitkin, I. A., Christofides, C. & Mandelis, A. Photothermal reflectance investigation of processed silicon. II. Signal generation and lattice temperature dependence in ion-implanted and amorphous thin layers. *J. Appl. Phys.* **67**, 2822–2830 (1990).
66. Salnick, A. & Opsal, J. Dynamics of the plasma and thermal waves in surface-modified semiconductors (invited). *Rev. Sci. Instrum.* **74**, 545–549 (2003).
67. Schmidt, A. J., Cheaito, R. & Chiesa, M. A frequency-domain thermoreflectance method for the characterization of thermal properties. *Rev. Sci. Instrum.* **80**, (2009).
68. Wang, L., Cheaito, R., Braun, J. L., Giri, A. & Hopkins, P. E. Thermal conductivity measurements of non-metals via combined time- and frequency-domain thermoreflectance without a metal film transducer. *Rev. Sci. Instrum.* **87**, (2016).
69. Qian, X., Ding, Z., Shin, J., Schmidt, A. J. & Chen, G. Accurate measurement of in-plane thermal conductivity of layered materials without metal film transducer using frequency domain thermoreflectance. *Rev. Sci. Instrum.* **91**, (2020).
70. Tanaka, T., Harata, A. & Sawada, T. Subpicosecond surface-restricted carrier and thermal dynamics by transient reflectivity measurements. *J. Appl. Phys.* **82**, 4033–4038 (1997).
71. Guidotti, D. & Driel, H. M. Van. Spacially resolved defect mapping in semiconductors using laser-modulated thermoreflectance. *Appl. Phys. Lett.* **47**, 1336–1338 (1985).
72. Mak, G. & Rühle, W. W. Femtosecond carrier dynamics in Ge measured by a luminescence up-conversion technique and near-band-edge infrared excitation. *Phys. Rev. B* **52**, 584–587 (1995).
73. Tanaka, T., Harata, A. & Sawada, T. Subpicosecond surface-restricted carrier and thermal dynamics by transient reflectivity measurements. *J. Appl. Phys.* **82**, 4033–4038 (1997).
74. Yang, J., Ziade, E. & Schmidt, A. J. Uncertainty analysis of thermoreflectance measurements. *Rev. Sci. Instrum.* **87**, (2016).
75. Misiakos, K. & Tsamakis, D. Accurate measurements of the silicon intrinsic carrier density from 78 to 340 K. *J. Appl. Phys.* **74**, 3293–3297 (1993).
76. Morin, F. J. & Maita, J. P. Conductivity and hall effect in the intrinsic range of germanium. *Phys. Rev.* **94**, 1525–1529 (1954).
77. Geballe, T. H. & Hull, G. W. Seebeck effect in germanium. *Phys. Rev.* **94**, 1134–1140 (1954).
78. Geballe, T. H. & Hull, G. W. Seebeck effect in silicon. *Phys. Rev.* **98**, 940–947 (1955).
79. Thomsen, C., Grahn, H. T., Maris, H. J. & Tauc, J. Surface generation and detection of phonons by picosecond light pulses. *Phys. Rev. B* **34**, 4129–4138 (1986).
80. Rosencwaig, A. Thermal wave characterization and inspection of semiconductor materials and devices. in *Photoacoustic and Thermal Wave Phenomena in Semiconductors* (ed. Mandelis, A.) (North Holland Publishing Company, 1987).
81. Heat Capacity of the Elements at 25 ^{o}C. in *CRC Handbook of Chemistry and Physics* (ed. Rumble, J. R.) (CRC Press/Taylor & Francis).
82. Debye, P. P. & Conwell, E. M. Electrical properties of N-type germanium. *Phys. Rev.* **93**, 693–706 (1954).
83. Canali, C., Nava, F. & Reggiani, L. Drift velocity and diffusion coefficients from time of flight measurements. in *Hot-electron transport in semiconductors* 87–111 (1985).
84. Stevenson, D. T. & Keyes, R. J. Measurements of the recombination velocity at germanium surfaces. *Phys. XX* **11**, 1041–1046 (1954).
85. Baek, D., Rouvimov, S., Kim, B., Jo, T. C. & Schroder, D. K. Surface recombination

velocity of silicon wafers by photoluminescence. *Appl. Phys. Lett.* **86**, 1–3 (2005).
86. Dominici, S., Wen, H., Bertazzi, F., Goano, M. & Bellotti, E. Numerical evaluation of Auger recombination coefficients in relaxed and strained germanium. *Appl. Phys. Lett.* **108**, 211103 (2016).
87. Sinton, R. A. & Swanson, R. M. Recombination in Highly Injected Silicon. *IEEE Trans. Electron Devices* **34**, 1380–1389 (1987).
88. Aspnes, D. E. & Studna, A. A. Dielectric functions and optical parameters of Si, Ge, GaP, GaAs, GaSb, InP, InAs, and InSb from 1.5 to 6.0 eV. *Phys. Rev. B* **27**, (1983).
89. Frey, B. J., Leviton, D. B. & Madison, T. J. Temperature-dependent refractive index of silicon and germanium. in *Optomechanical Technologies for Astronomy* vol. 6273 62732J (2006).
90. Spitzer, W. G. & Fan, H. Y. Determination of optical constants and carrier effective mass of semiconductors. *Phys. Rev.* **106**, 882–890 (1957).
91. Jellison, G. E. & Burke, H. H. The temperature dependence of the refractive index of silicon at elevated temperatures at several laser wavelengths. *J. Appl. Phys.* **60**, 841–843 (1986).
92. Maycock, P. D. Thermal conductivity of silicon, germanium, III-V compounds and III-V alloys. *Solid State Electron.* **10**, 161–168 (1967).
93. Reparaz, J. S. *et al.* A novel contactless technique for thermal field mapping and thermal conductivity determination: Two-Laser Raman Thermometry. *Rev. Sci. Instrum.* **85**, (2014).
94. Shi, H. *et al.* Exciton dynamics in suspended monolayer and few-layer MoS2 2D crystals. *ACS Nano* **7**, 1072–1080 (2013).
95. Suryavanshi, S. V., Gabourie, A. J., Barati Farimani, A. & Pop, E. Thermal boundary conductance of two-dimensional MoS2 interfaces. *J. Appl. Phys.* **126**, (2019).
96. Goodman, A. J. *et al.* Substrate-Dependent Exciton Diffusion and Annihilation in Chemically Treated MoS2and WS2. *J. Phys. Chem. C* **124**, 12175–12184 (2020).
97. Zhang, X. *et al.* Measurement of Lateral and Interfacial Thermal Conductivity of Single- and Bilayer MoS2 and MoSe2 Using Refined Optothermal Raman Technique. *ACS Appl. Mater. Interfaces* **7**, 25923–25929 (2015).
98. Taube, A., Judek, J., Łapińska, A. & Zdrojek, M. Temperature-dependent thermal properties of supported MoS2 monolayers. *ACS Appl. Mater. Interfaces* **7**, 5061–5065 (2015).
99. Yan, R. *et al.* Thermal conductivity of monolayer molybdenum disulfide obtained from temperature-dependent Raman spectroscopy. *ACS Nano* **8**, 986–993 (2014).
100. Kim, T., Ding, D., Yim, J. H., Jho, Y. D. & Minnich, A. J. Elastic and thermal properties of free-standing molybdenum disulfide membranes measured using ultrafast transient grating spectroscopy. *APL Mater.* **5**, (2017).
101. Lin, M. L. *et al.* Moiré phonons in twisted bilayer MoS2. *ACS Nano* **12**, 8770–8780 (2018).
102. Huang, D., Choi, J., Shih, C. K. & Li, X. Excitons in semiconductor moiré superlattices. *Nat. Nanotechnol.* **17**, 227–238 (2022).
103. Cao, Y. *et al.* Unconventional superconductivity in magic-angle graphene superlattices. *Nature* **556**, 43–50 (2018).
104. Quan, J. *et al.* Phonon renormalization in reconstructed MoS2 moiré superlattices. *Nat. Mater.* **20**, 1100–1105 (2021).

105. Maity, I., Naik, M. H., Maiti, P. K., Krishnamurthy, H. R. & Jain, M. Phonons in twisted transition-metal dichalcogenide bilayers: Ultrasoft phasons and a transition from a superlubric to a pinned phase. *Phys. Rev. Res.* **2**, 13335 (2020).
106. Li, C. & Lake, R. K. Small Angle and Non-Monotonic Behavior of the Thermal Conductivity in Twisted Bilayer Graphene. *arXiv* 22–25 (2019).
107. Mandal, S., Maity, I., Das, A., Jain, M. & Maiti, P. K. Tunable lattice thermal conductivity of twisted bilayer MoS 2 . *Phys. Chem. Chem. Phys.* **2**, (2022).
108. Han, S. *et al.* Twist-angle-dependent thermal conduction in single-crystalline bilayer graphene. *Appl. Phys. Lett.* **118**, (2021).
109. Li, H. *et al.* Thermal conductivity of twisted bilayer graphene. *Nanoscale* **6**, 13402–13408 (2014).
110. Bae, J. J. *et al.* Thickness-dependent in-plane thermal conductivity of suspended MoS2 grown by chemical vapor deposition. *Nanoscale* **9**, 2541–2547 (2017).
111. Speziale, S., Marquardt, H. & Duffy, T. S. Brillouin scattering and its application in geosciences. *Spectrosc. Methods Mineral. Mater. Sci.* **78**, 543–603 (2014).

Appendix 1: TDTR at the Molecular Foundry

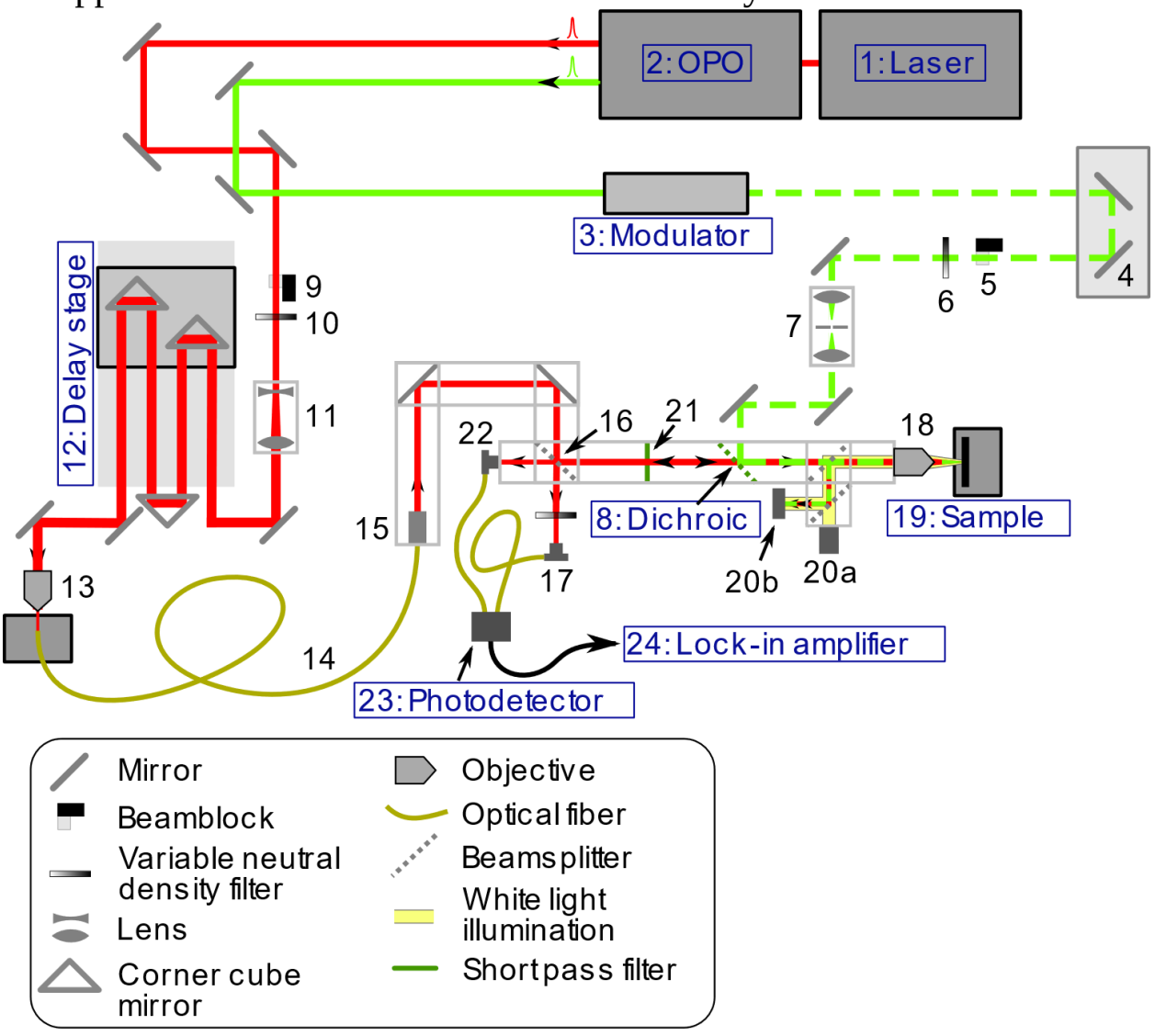

Number	Name	Function
1	Ti:sapphire laser	Generates ~140 fs laser pulses at 800 nm
2	Optical parametric oscillator	Tunes laser output to a variety of wavelengths, here 800 nm and 565 nm
Pump line		
3	Electro-optic modulator	The electro-optic modulator, (Conoptics M350-160, driven by a Conoptics 25D amplifier) provides a modulation envelope on laser pulses, varying the intensity sinusoidally at a tunable frequency from 100s of kilohertz to 10 MHz
4	Micrometer stage	Allows adjustment of the length of the pump path, allowing more precise matching to the probe path
5	Pump beamblock	Allows computer-controlled blocking of the pump beam, for example for measuring signal offsets before measurement
6	Pump neutral density filter	Allows control of the pump beam power
7	Pinhole and associated optics	Two lenses focus light through a pinhole and then recollimate it, improving the roundness of the laser spot
8	Dichroic mirror	Reflects the pump beam to the sample while allowing the probe beam to pass through
Probe line		
9	Probe beamblock	Allows computer-controlled blocking of the probe beam
10	Probe neutral density filter	Allows control of the probe beam power
11	Beam expander	Two lenses expand and recollimate the beam at a larger radius, reducing divergence through the delay stage
12	Delay stage	By physically moving two corner-cube mirrors, the length of the probe path can be precisely set, allowing sweeping delay time during measurement
13	Fiber launch setup	An objective lens focuses the output beam from the delay stage into an optical fiber, which is mounted on a computer-controlled stage to allow optimization of transmission through the fiber
14	Single-mode optical fiber	The single-mode fiber provides the same output beam profile and radius regardless of the input profile, meaning that changes in spot shape and size as the delay stage moves can be ignored
15	Focusing optics	The output from the fiber is collimated for transmission to the sample
16	50/50 beamsplitter	Incoming light from the single-mode fiber is split, half to the sample and half to the reference collimator, allowing monitoring of probe intensity. Reflected signal from the sample is also split, half to the signal collimator for detection, and half discarded
17	Reference collimator and fiber	After the reference beam passes through a neutral density filter, a parabolic mirror couples it into an optical fiber which takes it to the photodetector. The neutral density filter is adjusted before each measurement to match the power of the reference signal to that from the sample

Sample and measurement

18	Objective lens	A microscope objective focuses the pump and probe beams and light from the illumination system onto the sample. Changing the objective allows control of the laser spot size
19	Sample	The sample to be measured is mounted on an xyz stage, allowing positioning to areas of interest
20	Illumination and viewing system	An LED (20a) is mounted on a 50:50 beamsplitter, such that (half of its) light is directed toward the laser beam path. On the beam path, a 92:8 beamsplitter reflects ~8% of the LED light to the sample (while transmitting ~92% of the laser power). Viewing of the sample and the laser spot is possible through a camera (20b) which is also mounted on the 50:50 beamsplitter such that a fraction of the reflected light from the sample is directed to it.
21	Short pass filter	Blocks any pump light that passes through the dichroic mirror, ensuring that the measured signal is based entirely on the probe reflection
22	Signal collimator and fiber	A parabolic mirror couples the probe light reflected off the sample into an optical fiber that takes it to the photodetector
23	Photodetector	A balanced photodetector (Thorlabs PDB435A) subtracts the signal and reference intensities, reducing noise, and passes the result to the lock-in amplifier
24	Lock-in amplifier	The lock-in amplifier (Zurich Instruments HF2LI) selects the component of the measured signal at the frequency at which the pump beam is modulated, allowing measurement of the response of the sample to the pump heating and rejecting noise at other frequencies.